

METHODS FOR AUTONOMOUS MEASUREMENT OF 3D JOINT KINEMATICS FROM 2D
FLUOROSCOPIC IMAGES

By

ANDREW JAMES JENSEN

A DISSERTATION PRESENTED TO THE GRADUATE SCHOOL
OF THE UNIVERSITY OF FLORIDA IN PARTIAL FULFILLMENT
OF THE REQUIREMENTS FOR THE DEGREE OF
DOCTORATE OF PHILOSOPHY

UNIVERSITY OF FLORIDA

2024

© 2024 Andrew James Jensen

I would like to dedicate this to my wife, Lauren, my parents, Robin and Erik, and my Lord and Savior, Jesus Christ †.

ACKNOWLEDGEMENTS

First, I would like to thank my parents for their continued support throughout my undergraduate and graduate studies. They fostered my work ethic and drive to get through something as ambitious as a doctorate.

Secondly, I would like to thank my advisor, Scott Banks. He has truly been something of a second dad to me as I navigate through graduate school and my future career. Though most conversations seem to revolve around either beer, music, or hiking, we seem to have gotten quite a lot done.

Third, I would like to thank my wife, Lauren. Though busy with medical school, she still takes the time to understand my research and offer support outside of academics.

TABLE OF CONTENTS

	<u>page</u>
ACKNOWLEDGEMENTS	4
LIST OF TABLES.....	8
LIST OF FIGURES.....	11
ABSTRACT	12
CHAPTER	
1 INTRODUCTION	14
1.1 Computer Vision Primer	16
1.1.1 Geometric Transformations	16
1.1.2 Image Formation and Camera Properties.....	22
1.1.3 Image Processing.....	25
1.1.4 Image Similarity Metrics	30
1.2 Deep Learning for Image Processing in Orthopaedics	33
1.2.1 The Purpose of Neural Networks for Image Processing.....	33
1.2.2 Neural Network Structure.....	34
1.2.3 Training Neural Networks	40
1.3 Model-Image Registration for Measuring Kinematics from Fluoroscopic Images	41
1.3.1 Pre-Computed Projective Geometries.....	42
1.3.2 Motion Capture	42
1.3.3 Iterative Projections	43
1.3.4 Fully Human Supervised.....	44
1.3.5 Biplane Kinematics Measurements	44
1.3.6 Roentgen Stereophotogrammetric Analysis	45
1.4 Automating Measurements of Kinematics from Fluoroscopic Images	45
1.4.1 Autonomous Implant Detection	45
1.4.2 Initial Pose Estimation.....	47
1.4.3 Objective Function	52
1.4.4 Optimization Routine.....	54
1.4.5 Overcoming Single-Plane Limitations	58
2 THE AIMS OF THIS DISSERTATION	59
2.1 Aim 1: JointTrack Machine Learning: An Autonomous Method of Measuring 6-DOF TKA Kinematics from Single-Plane Fluoroscopic Images	6-59
2.2 Aim 2: Correcting Symmetric Implant Ambiguity in Measuring Total Knee Arthroplasty Kinematics from Single-Plane Fluoroscopy	59
2.3 Aim 3: Musings on Latent Kinematics Space and Synthetic Biomechanics Data.....	60
2.4 Aim 4: This Will Definitely Work on Shoulder Implants, Right?.....	60

3	JOINTTRACK MACHINE LEARNING: AN AUTONOMOUS METHOD OF MEASURING 6-DOF TKA KINEMATICS FROM SINGLE-PLANE FLUOROSCOPIC IMAGES	61
	3.1 Methods.....	63
	3.1.1 Image Segmentation.....	63
	3.1.2 Initial Pose Estimates.....	64
	3.1.3 Pose Refinement	66
	3.1.4 Pose Ambiguities and Registration Blunders.....	66
	3.2 Results	67
	3.3 Discussion.....	70
4	CORRECTING SYMMETRIC IMPLANT AMBIGUITY IN MEASURING TOTAL KNEE ARTHROPLASTY KINEMATICS FROM SINGLE-PLANE FLUOROSCOPY	
	74	
	4.1 Methods.....	75
	4.1.1 Study Design and Sample.....	75
	4.1.2 Determining Symmetric Orientations.....	76
	4.1.3 Constructing Dataset	77
	4.1.4 Classification Algorithms	78
	4.1.5 Fixing Incorrect Symmetry Trap Poses	79
	4.2 Results	80
	4.2.1 Machine Learning Classification Performance	80
	4.2.2 Stratified ψ Test Set Performance	83
	4.2.3 Symmetry Trap Correction Performance.....	83
	4.3 Discussion.....	83
	4.4 Concluding Remarks.....	85
5	MUSINGS ON LATENT KINEMATICS SPACE AND SYNTHETIC BIOMECHANICS DATA	87
	5.1 Introductory Remarks	87
	5.2 Latent Kinematics Space and Reducing the Number of Movements Required for a Full Kinematics Evaluation.....	88
	5.2.1 Brief Mathematical Preliminary and Notation	88
	5.2.2 A Kinematics Translator	89
	5.2.3 Problem 1: Groups calling different movements the same thing	90
	5.2.4 Problem 2: No standardized set of movements to measure	91
	5.2.5 Problem 3: Groups measuring kinematics at different flexion angles	91
	5.3 Toward Generating Synthetic Biomechanics Data.....	92
6	THIS WILL DEFINITELY WORK ON SHOULDER IMPLANTS, RIGHT? ²	93
	6.1 JointTrack Machine Learning on Total Shoulder Arthroplasty Implants	94
	6.1.1 Introduction.....	94
	6.1.2 Methods	94

6.1.3	Results	95
6.1.4	Discussion	95
6.2	Improving Model-Image Registration	96
6.2.1	Introduction.....	96
6.2.2	Improving Error Gradient.....	97
6.2.3	Modified Mean Distance Cost Function.....	99
6.2.4	The Psychology of Shape and Mimicking Human Operators	100
6.2.5	Developing a Cost Function for Aligning High-Curvature Regions	101
6.2.6	Discussion	105
6.3	2D Shape Projection Sensitivity Analysis	106
6.4	Methods.....	108
6.4.1	Data Collection	108
6.4.2	Image Generation	108
6.4.3	Invariant Angular Radial Transform	109
6.4.4	Shape Differences and Sensitivity	110
6.5	Results	112
6.6	Discussion.....	112
6.7	Concluding Remarks.....	116
	LIST OF REFERENCES	117
	BIOGRAPHICAL SKETCH	129

LIST OF TABLES

<u>Tables</u>	<u>page</u>
1-1 A list of activation functions and their corresponding mathematical formula	36
3-1 RMS differences between NFD initial estimates and human supervised kinematics	68
3-2 RMS differences between DIRECT-JTA optimized and human supervised kinematics ...	69
4-1 Machine Learning Classifier Performance.....	81
4-2 Stratified- ψ test set stacked generalization classification performance	82
6-1 Root mean squared differences between JointTrack Machine Learning optimized kine- matics and manually registered kinematics on single-plane fluoroscopy.....	95
6-2 Average projected-shape sensitivity values for each of the implant models.....	113

LIST OF FIGURES

<u>Figures</u>	<u>page</u>
1-1 The geometry of perspective projection can be visualized by using similar triangles. The overall scaling of the image is based on the ratio of the focal length to the depth of the object.	23
1-2 A collection of morphological operations on a binary image: (a) original image; (b) dilation; (c) erosion; (d) majority; (e) opening; (f) closing. Image from [116]	30
1-3 An example of a neural network mimicking the human brain.	34
1-4 A schematic representing a single neuron that receives n inputs and applies ϕ as an activation function.	35
1-5 A basic fully connected network with a single hidden layer. Each of the neurons are exactly the same as the neurons shown in figure 1-4	37
1-6 An example of extracted features from a convolutional neural network. As shown, the deeper into the network one explores, the combination of core features start to create higher level features that might represent the shape of a specific animal [106].	39
1-7 A standard U-Net architecture for a convolutional neural network. This architecture is the most common form of network used for biomedical image analysis and processing. .	39
1-8 A visual representation of Shubert's algorithm, which finds the global minima iteratively through a repeated calculation of the intersection of two lines with slope $\pm K$. If K is known, it will always find the global minimum.	56
1-9 The DIviding RECTangles (DIRECT) algorithm in one dimension. It can find the global minimum of a function without a-priori knowledge of the Lipschitz constant. The value of the line with slope $\pm K$ at each of the end-points represents the theoretical minimum for the value of the function in that region. Thus, the size of the region and the value of the function at the center help the algorithm determine potentially optimal sub-regions. .	57
1-10 The potentially optimal regions of the DIRECT algorithm are those points that lay along the lower convex hull of the scatter plot of sub-domain size vs function value at center. This is due to those regions being the locations where the maximum possible rate of change in the function might be a minimum, without any prior knowledge of the Lipschitz constant.....	58
3-1 An overview of the pipeline for autonomous measurements of total knee arthroplasty kinematics. First, the data is processed through a convolutional neural network to locate the pixels belonging to the femoral and tibial implants [123], then, Normalized Fourier Descriptor shape libraries are used to determine and initial pose estimate [8], and lastly, DIRECT-JTA [39] is run on those segmented images using the NFD estimates as initializations for pose.	62

3-2	Data from seven studies were used to train and test the TKA kinematics measurement pipeline. Color coding in the figure identifies how many images were used for the training, validation, and testing functions. Images from the seventh study were used exclusively for testing the measurement pipeline that was trained using images from the other six studies.	64
3-3	A representative fluoroscopic images is shown (a) with corresponding femoral (b) and tibial (c) ground-truth images created by flat-shaded projections of registered implant models.	65
3-4	Femoral (left) and tibial (right) NFD shape libraries were generated to capture the variation in projection silhouette geometry with out-of-plane rotation [8]. Initial pose estimates were generated by comparing the NFD contour from the x-ray image to the shape library.	65
3-5	The histogram (left) shows the correctly registered frames (Hits, blue) and incorrectly registered frames (Blunders, orange) plotted as a function of the apparent tibial varus/valgus angle relative to the viewing raw. The probability plot (right) shows the distribution of blunders (solid orange) and the cumulative probability of blunders (dotted orange). The Ambiguous Zone is defined as apparent tibial varus/valgus rotations less than the mean + one standard deviation of the blunder probability distribution, capturing approximately 85 % of the blunders.	67
3-6	The figure shows the same radiographic image with two registered tibial implant poses: (a) shows a correctly registered tibial implant, while (b) shows an implant caught in a local cost function minimum corresponding to a nearly symmetric pose.	70
4-1	Two examples of symmetry pose dyads with the correct (left) and symmetry trap (right) kinematics. For some orientations, the symmetry trap is obviously incorrect (top), and for others, it is more ambiguous (bottom).	75
4-2	A visualization of the “symmetry flipper” algorithm that converts 3D orientations into their symmetric counterpart.	77
4-3	A 3D scatter plot of our training data with ‘true’ poses in orange and ‘symmetry trap’ poses in blue. Of note, there are distinct regions of exclusively ‘symmetry trap’ poses, while the region of predominately ‘true’ poses (orange cylinder along Flexion/Extension axis) also has many ‘symmetry trap’ poses.	78
6-1	A graphical representation of the Normalized Surface Distance from [99, 100].	97
6-2	A graphical representation of the Mean Average Surface Distance from [99, 100].	98
6-3	A graphical representation of the Average Symmetric Surface Distance from [99, 100]. .	98
6-4	A graphical representation of the Hausdorff Distance, taken from [99, 100].	99

6-5	Some representative examples of the experiences that Fred Attneave performed to establish the primacy of high curvature as salient in shape recreation and recognition, from [3].....	101
6-6	Some different model views of a manually registered humeral and glenoid implant in an rTSA system. Of note, each view gives the user a different type of feature to focus on. The original view allows the user to determine the relative orientation based on shading, the transparent view allows the user to see the underlying fluoroscopic image, and the solid view allows the user to focus on specific regions of error. Each is crucial to performing manual registration.....	102
6-7	A plot demonstrating the values of the Menger Curvature along the contour of an rTSA humeral implant. The regions of high curvature are the peaks of the plot.	104
6-8	A representative example of poor internal/external rotation of the humeral implant after automated model-image registration using JointTrack Machine Learning [58].	108
6-9	A generic manufacturer-provided humeral implant with label x, y, and z rotation axis. Additionally, each of the δ_x , δ_y , and δ_z are shown, corresponding to the rotational directions of each shape descriptor difference.....	111
6-10	The \mathbb{S} plot for a humeral implant for δ rotations along the x, y, and z axis, respectively..	113
6-11	The \mathbb{S} plot for a glenosphere implant for δ rotations along the x, y, and z axis, respectively.....	113
6-12	The \mathbb{S} plot for a femoral implant for δ rotations along the x, y, and z axis, respectively..	114
6-13	The \mathbb{S} plot for a tibial implant for δ rotations along the x, y, and z axis, respectively. ...	114

Abstract of Dissertation Presented to the Graduate School
of the University of Florida in Partial Fulfillment of the
Requirements for the Degree of Doctorate of Philosophy

**METHODS FOR AUTONOMOUS MEASUREMENT OF 3D JOINT KINEMATICS FROM 2D
FLUOROSCOPIC IMAGES**

By

Andrew James Jensen

March 2024

Chair: Scott Banks

Major: Mechanical Engineering

The fundamental role of human synovial joints is enabling dynamic motion within the musculoskeletal system, which is essential for a wide range of activities. Diseases affecting these joints often lead to pain during movement, imposing significant economic burdens estimated at approximately USD 300 billion annually, encompassing direct healthcare costs and indirect impacts such as lost productivity [1]. Among these conditions, osteoarthritis is particularly prevalent, characterized by the gradual deterioration of cartilage, leading to joint pain and mobility issues [111]. Arthroplasty, specifically total knee arthroplasty (TKA) and reverse total shoulder arthroplasty (rTSA), presents a solution by replacing the damaged joint surfaces with synthetic materials to alleviate pain and restore functionality. Despite the high success rate, a subset of patients reports dissatisfaction due to residual symptoms such as pain, instability, or stiffness post-surgery [7, 18, 107]. Current diagnostic practices for evaluating musculoskeletal disorders primarily rely on static assessments, which fail to capture the complexities of joint mechanics under dynamic conditions—when symptoms are most pronounced. While sophisticated technologies for 3D motion capture exist, their adoption in clinical settings is limited by high costs and operational challenges. Combined with 3D-to-2D model-image registration, fluoroscopic imaging has shown promise for accurate joint assessment. However, the technique's broader application is hampered by the extensive manual effort required, leading to increased time and financial resources [8, 81]. This dissertation introduces a novel framework for

the autonomous measurement of TKA and rTSA kinematics utilizing single-plane imaging techniques. It integrates both modern and historical algorithms, leveraging recent advancements in computational power and machine learning to eliminate the need for manual intervention in the model-image registration process. This approach promises a reliable, cost-effective, and practical method for obtaining accurate dynamic joint kinematics in a clinical setting, potentially transforming the diagnostic landscape for musculoskeletal diseases and enhancing patient outcomes [39, 96].

CHAPTER 1

INTRODUCTION

Total Knee Arthroplasty (TKA) is a standard procedure for alleviating symptoms related to osteoarthritis in the knee. In 2018, orthopaedic surgeons performed more than 715,000 TKA operations in the United States [2]. This number is projected to increase to 3.48 million by 2030 [73] due to an aging population and increased obesity rates. While TKA largely relieves symptomatic osteoarthritis, roughly 20% of TKA patients express postoperative dissatisfaction, citing mechanical limitations, pain, and instability as the leading causes [7, 18, 107]. Standard methods of musculoskeletal diagnosis cannot quantify the dynamic state of the joint, either pre- or post-operatively; clinicians must rely on static imaging (radiography, MRI, CT) or qualitative mechanical tests to determine the condition of the affected joint, and these tests cannot easily be performed during weight-bearing or dynamic movement when most pain symptoms occur. Unfortunately, most of the tools used to quantify 3D dynamic motion are substantially affected by soft-tissue artifacts [44, 78, 113], are prohibitively time-consuming or expensive [34], or cannot be performed with equipment available at most hospitals. It is clear that there is currently a lack of clinically viable methods that can quantify dynamic, weight-bearing kinematics of joints after arthroplasty procedures. This gap limits clinicians' ability to relate patient-reported instability and discomfort during activity to measurable joint mechanics [10].

Model-image registration is a process where a 3D model is aligned to match an object's projection in an image [22]. Researchers have performed model-image registration using single-plane fluoroscopic or flat-panel imaging since the 1990s. Early methods used pre-computed distance maps [75, 137], or shape libraries [8, 121, 122] to match the projection of a 3D implant model to its projection in a radiographic image. With increasing computational capabilities, methods that iteratively compared implant projections to images were possible [39, 79, 81]. Most model-image registration methods provide sufficient accuracy for clinical joint assessment applications, including natural and replaced knees [13, 14, 24, 70], natural and replaced shoulders [66, 80, 84, 114], and extremities [27, 28, 35]. One of the main benefits of this single-plane approach is that suitable images can be acquired with equipment found in most

hospitals. The main impediment to implementing this approach into a standard clinical workflow is the time and expense of human operators to supervise the model-image registration process. These methods require either (1) an initial pose estimate [39, 79], (2) a pre-segmented contour of the implant in the image [22, 75], or (3) a human operator to assist the optimization routine out of local minima [81]. Each of these requirements makes model-image registration methods impractical for clinical use. Even state-of-the-art model-image registration techniques [39] require human initialization or segmentation to perform adequately.

Machine learning algorithms automate the process of analytical model building, utilizing specific algorithms to fit a series of inputs to their respective outputs. Neural networks are a subset of machine learning algorithms that utilize artificial neurons inspired by the human brain's connections [82]. These networks have shown a great deal of success in many computer vision tasks, such as segmentation [29, 103, 123], pose estimation [64, 127], and classification [71, 97, 98]. These capabilities might remove the need for human supervision from TKA model-image registration.

Section 1.1 gives an overview of some of the fundamental building blocks of computer vision and projective geometry. A cursory understanding of these operations is necessary to the underlying mathematics motivating model-image registration, as well as recreating the images generated by fluoroscopic imaging systems. It also outlines a few key classes of image similarity metrics, which are useful when defining objective functions for optimization routines.

Section 1.2 discusses neural networks from a bottom-up perspective, and explains how they can be used to automate different tasks in computer vision, with a strong emphasis on image processing. Understanding the “how” behind neural networks and deep learning drives their usage in automating historically tedious and human-supervised tasks.

Section 1.3 outlines historical methods of utilizing model-image registration for measuring total knee and natural knee kinematics from various imaging modalities. The main emphasis of this chapter is to explain the breadth of research that has been performed in this space, and also explain fundamental limitations with each method that prevent the adoption of this technology

into a clinical setting.

Section 1.4 utilizes the previous chapters to describe a method for autonomously measuring total knee arthroplasty kinematics from single-plane fluoroscopic imaging. Utilizing the framework built by computer vision and machine learning, and driven by the shortcomings of historic methods, a novel pipeline is presented that removes the need for human supervision for this technology, bringing it one step closer to clinical adoption.

Lastly, Chapter 2 discusses the aims of this thesis, beginning with a validation of the pipeline, a novel algorithm addressing a systemic issue in single-plane model-image registration, and a first-principals approach to exploring 2D shape sensitivity.

1.1 Computer Vision Primer

In order to more fully understand the process of extracting total knee arthroplasty kinematics from single-plane digital fluoroscopic images, we must first explore some fundamentals of computer vision, specifically elements of image formation, image processing, and object projection.

1.1.1 Geometric Transformations

Geometric primitives, such as points, are fundamental building blocks for representing shapes and objects in computer graphics. In this section, we will discuss how points can be represented in 2D and 3D space, along with the different mathematical operations that you can perform on those points.

1.1.1.1 2D and 3D Points

In N-dimensional space, a point is represented as a set of N scalars, each representing a magnitude in a particular direction. This can be represented mathematically as a column vector (Eq. 1-1). In two dimensions, a point is represented with two elements, $\mathbf{x} = [x, y]^T$. Similarly, in three dimensions, a point is represented with three elements, $\mathbf{x} = [x, y, z]^T$.

$$\mathbf{x} = \begin{bmatrix} x_1 \\ x_2 \\ \vdots \\ x_{N-1} \\ x_N \end{bmatrix} \in \mathbb{R}^N \quad (1-1)$$

Homogeneous coordinates provide a way to represent points with an additional scale factor, \tilde{w} . This allows us to perform rotations and translations simultaneously and successively using matrix multiplications. The scale factor lets us handle projections and other transformations cleanly through linear algebra operations, even if the final result is not a vector in the original coordinate space. For example, a point $x = [2, 3]^T$ in 2D can be converted to homogeneous coordinates as $\tilde{x} = [2, 3, 1]^T$. The 1 is a placeholder for the scale term that allows matrix transformations like rotations and translations to be applied while preserving the original Cartesian coordinates stored in the first two elements. After the transformations, we can recover the Cartesian coordinates by dividing through by the final scale factor \tilde{w} . Homogeneous coordinates for a point in N-dimensional space are represented as a column vector matrix with $N+1$ elements (Eq. 1-2). When dealing with homogeneous coordinates, $\tilde{\mathbf{x}} = \tilde{w}\bar{\mathbf{x}}$, where $\tilde{\mathbf{x}}$ is the scaled version of $\bar{\mathbf{x}}$, and $\bar{\mathbf{x}}$ is simply the original vector, \mathbf{x} , with a 1 appended.

$$\tilde{\mathbf{x}} = \begin{bmatrix} \tilde{x}_1 \\ \tilde{x}_2 \\ \vdots \\ \tilde{x}_N \\ \tilde{w} \end{bmatrix} = \tilde{w} \begin{bmatrix} \mathbf{x} \\ 1 \end{bmatrix} = \tilde{w}\bar{\mathbf{x}} \quad (1-2)$$

1.1.1.2 2D Transformations

Transformations are operations that change the position, orientation, or shape of an object in 2D space. One of the most basic transformations is a translation, which moves an object by

adding a displacement vector to its position (Eq. 1-3).

$$\mathbf{x}' = \begin{bmatrix} x \\ y \end{bmatrix} + \begin{bmatrix} t_x \\ t_y \end{bmatrix} = \mathbf{x} + \begin{bmatrix} t_x \\ t_y \end{bmatrix} = \mathbf{x} + \mathbf{t}$$

Or, using homogeneous coordinates and matrix multiplication

(1-3)

$$= \begin{bmatrix} 1 & 0 & t_x \\ 0 & 1 & t_y \\ 0 & 0 & 1 \end{bmatrix} \begin{bmatrix} x \\ y \\ 1 \end{bmatrix} = [\mathbf{I} \quad \mathbf{t}] \bar{\mathbf{x}}$$

In this equation, \mathbf{x} is the original position of the object, \mathbf{x}' is the transformed position, and \mathbf{t} is the displacement vector that specifies the amount of translation in the x and y directions. Using homogeneous coordinates and matrix multiplication allows for the convenient representation of multiple transformations as a single matrix multiplication, as well as for the composition of multiple transformations (Eq. 1-4).

$$\begin{aligned} \bar{\mathbf{x}}'' &= \begin{bmatrix} 1 & 0 & t_x \\ 0 & 1 & t_y \\ 0 & 0 & 1 \end{bmatrix} \begin{bmatrix} 1 & 0 & q_x \\ 0 & 1 & q_y \\ 0 & 0 & 1 \end{bmatrix} \begin{bmatrix} x \\ y \\ 1 \end{bmatrix} \\ &= \begin{bmatrix} x + t_x + q_x \\ y + t_y + q_y \\ 1 \end{bmatrix} \end{aligned} \quad (1-4)$$

The next type of 2D transformation is a rotation, which changes the orientation of an object, but not its shape (Eqs. 1-5 and 1-6).

$$\mathbf{x}' = \mathbf{R}\mathbf{x} \quad (1-5)$$

where

$$\mathbf{R} = \begin{bmatrix} \cos\theta & -\sin\theta \\ \sin\theta & \cos\theta \end{bmatrix} \quad (1-6)$$

This will rotate an object by θ in the counter clockwise direction.

It is also possible to perform a rotation and a translation at the same time, by replacing the identity matrix \mathbf{I} in Equation 1-3 with the rotation matrix \mathbf{R} from Equation 1-6. This results in a transformation that preserves lengths and angles while rotating and translating the rigid object (Eq. 1-7).

$$\mathbf{x}' = \begin{bmatrix} \mathbf{R}_{2 \times 2} & \mathbf{t} \end{bmatrix} \bar{\mathbf{x}} \quad (1-7)$$

A scaled rotation will change the size of the object by some scalar factor, s (Eq. 1-8); this transformation preserves angles.

$$\mathbf{x}' = \begin{bmatrix} s\mathbf{R}_{2 \times 2} & \mathbf{t} \end{bmatrix} \bar{\mathbf{x}} \quad (1-8)$$

An affine transformation preserves parallel lines. It applies a general linear transformation defined by an arbitrary 2×3 matrix(Eq. 1-9).

$$\mathbf{x}' = \mathbf{A}\bar{\mathbf{x}}$$

where

$$\mathbf{A} = \begin{bmatrix} a_{11} & a_{12} & a_{13} \\ a_{21} & a_{22} & a_{23} \end{bmatrix} \quad (1-9)$$

A perspective transformation uses homogeneous coordinates to apply projections that handle depth and perspective foreshortening. This simulates a camera projection (Eq. 1-10).

$$\tilde{\mathbf{x}}' = \tilde{\mathbf{H}}\tilde{\mathbf{x}} \quad (1-10)$$

To obtain inhomogeneous results, the resultant $\tilde{\mathbf{x}}'$ must be normalized (Eq. 1-11). A

projective transformation preserves straight lines.

$$\begin{aligned} x' &= \frac{\tilde{x}}{\tilde{w}} & y' &= \frac{\tilde{y}}{\tilde{w}} \\ &= \frac{h_{11}x + h_{12}y + h_{13}}{h_{31}x + h_{32}y + h_{33}} & &= \frac{h_{21}x + h_{22}y + h_{23}}{h_{31}x + h_{32}y + h_{33}} \end{aligned} \quad (1-11)$$

1.1.1.3 3D Transformations

Transformations in three dimensions are extremely similar to their two dimensional counterpart, except the dimensionality of each transformation is increased by one. However, three dimensional rotations introduce added complexity, due to multiple axes of rotation, and the non-commutativity of those rotations. We handle this by utilizing Euler angles [47], which decomposes the final orientation of an object as a combination of rotations about the three coordinate axes. Each rotation about an axis is represented with a matrix (Eq. 1-12), and the final rotation matrix is represented as the order of the rotations that produced it (e.g. Z-X-Y rotation).

$$R_x = \begin{bmatrix} 1 & 0 & 0 \\ 0 & c_x & -s_x \\ 0 & s_x & c_x \end{bmatrix} \quad R_y = \begin{bmatrix} c_y & 0 & s_y \\ 0 & 1 & 0 \\ -s_y & 0 & c_y \end{bmatrix} \quad R_z = \begin{bmatrix} c_z & -s_z & 0 \\ s_z & c_z & 0 \\ 0 & 0 & 1 \end{bmatrix} \quad (1-12)$$

Anatomically, the rotations can be chosen such that they align with the anatomic axes of the joint. This allows for congruence between the mathematical notation used to represent an object in space, and the medical notation used by orthopaedic practitioners (i.e. aligning a Z-X-Y rotation decomposition with the flexion-abduction-external rotation order used by orthopaedic surgeons).

For simplicity, we can also represent 3D rotations as an axis-angle decomposition, which describes the transformation as a single rotation about an arbitrary axis [33] (Eq. 1-13). You can use trigonometric identities to determine the axis and angle given an arbitrary rotation matrix.

$$R_{3 \times 3} = \begin{pmatrix} m_x^2 v + c & m_x m_y v - m_z s & m_x m_z v - m_y s \\ m_x m_y v + m_z s & m_y^2 v + c & m_y m_z v - m_x s \\ m_x m_z v - m_y s & m_y m_z v + m_x s & m_z^2 v + c \end{pmatrix}$$

where

$$\begin{aligned} s &= \sin(\theta) \\ c &= \cos(\theta) \\ v &= (1 - c) \end{aligned} \tag{1-13}$$

and

$$\mathbf{m} = \begin{bmatrix} m_x \\ m_y \\ m_z \end{bmatrix} \text{ is the axis of rotation}$$

3D to 2D Projections Geometric primitives, such as points, lines, and polygons, are the building blocks of computer graphics. These basic shapes can be transformed and combined in various ways to create more complex objects and scenes. In order to represent these 3D primitives and objects in 2D image space, we must apply transformations that manipulate their position, orientation, and other properties. By using these transformations, we can create the illusion of depth and spatial relationships on a flat display. Understanding how to work with primitives and transform them is crucial for creating a wide range of visual effects and graphics in computer graphics.

In computer graphics, one of the most basic methods of projecting three-dimensional objects onto a two-dimensional image plane is an orthographic projection. This projection simply drops the depth component of the object and flattens it onto the image plane (Eq. 1-14). This can be thought of as mimicking a camera with a long focal length, or when the depth of the object is shallow compared to its distance from the camera (also known as a weak perspective projection). In this equation, \mathbf{p} represents a point in 3D space and \mathbf{x} represents the projected point in 2D image

space. The $\tilde{\cdot}$ still represents the point in homogeneous coordinates.

$$\tilde{\mathbf{x}} = \begin{bmatrix} 1 & 0 & 0 & 0 \\ 0 & 1 & 0 & 0 \\ 0 & 0 & 0 & 1 \end{bmatrix} \tilde{\mathbf{p}} \quad (1-14)$$

Perspective Projection The most common 3D-2D projection is *perspective projection*, which accounts for depth perception. This can be done by scaling each point by its z position relative to the camera (Eq. 1-15). This necessitates using homogeneous coordinates (Eq. 1-16).

$$\bar{\mathbf{x}} = \mathcal{P}_z(\mathbf{p}) = \begin{bmatrix} x/z \\ y/z \\ 1 \end{bmatrix} \quad (1-15)$$

$$\tilde{\mathbf{x}} = \begin{bmatrix} 1 & 0 & 0 & 0 \\ 0 & 1 & 0 & 0 \\ 0 & 0 & 1 & 0 \end{bmatrix} \tilde{\mathbf{p}} \quad (1-16)$$

The perspective projection is the cornerstone of model-image registration. If a matrix mimics the fluoroscopic projective geometry in the clinic, then this offers a strong possibility of re-creating a virtual scene with the same geometry as the actual scene.

1.1.2 Image Formation and Camera Properties

Using our knowledge of geometric transformations and projective geometries, we can build up a model of a camera step by step. We standardize our reference frame by having the z direction along the focal direction of the camera, the x direction to the right, and the y direction such that the right-hand rule is maintained. The origin is at the center of the camera.

We will describe the object of interest as a collection of points,

$\mathbf{p}_i = [x_i, y_i, z_i, 1]$ for $i = 1, 2, \dots, N$. For a complete picture, any given operation will be performed on all points. For simplicity, the following equations will demonstrate the process on a single point of the object.

First, we need to describe the location and orientation of the object with respect to the camera. This can be done with a 3D homogeneous transformation matrix (translation and rotation) (Eq. 1-17).

$$\tilde{\mathbf{p}}' = \begin{bmatrix} \mathbf{R}_{3 \times 3} & \mathbf{t}_{3 \times 1} \\ \mathbf{0}_{1 \times 3} & 1 \end{bmatrix} \tilde{\mathbf{p}} \quad (1-17)$$

Then, we use a projective transformation that determines the perspective scaling between the object's location and the image plane at the focal distance. Geometrically, this relationship can be visualized with similar triangles (Fig. 1-1) and quantified using the ratio of lengths (Eq. 1-18). In these equations, f' is the focal distance in units of length.

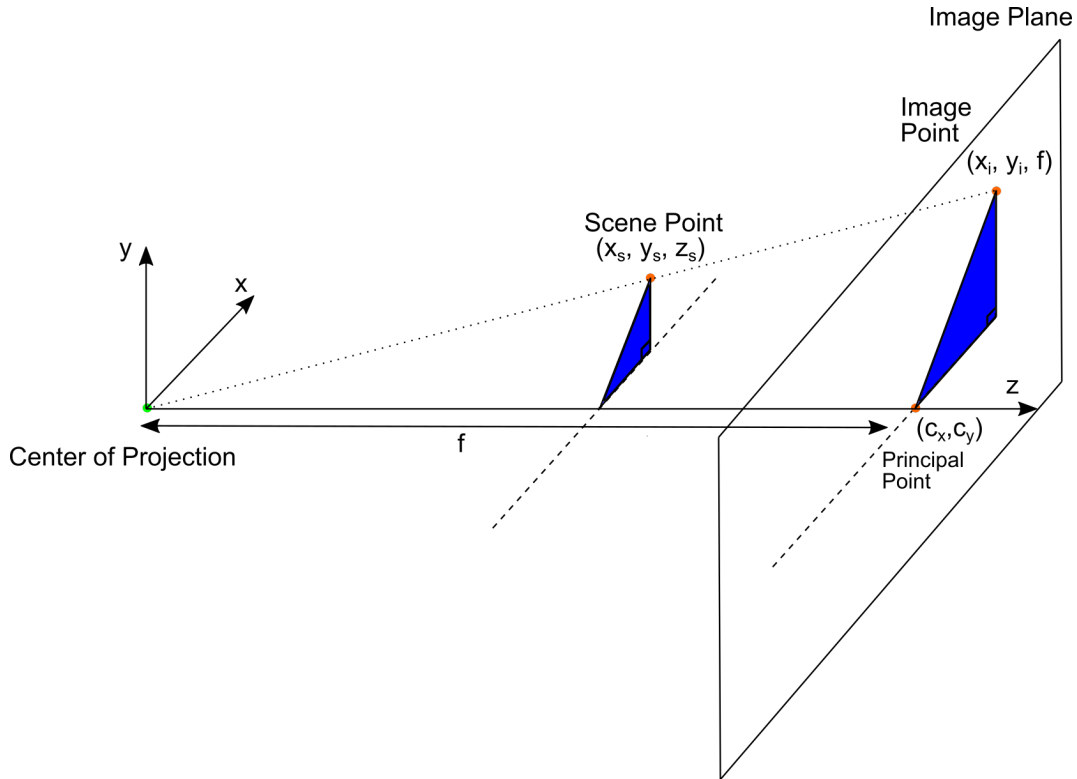


Figure 1-1. The geometry of perspective projection can be visualized by using similar triangles. The overall scaling of the image is based on the ratio of the focal length to the depth of the object.

$$\tilde{\mathbf{x}}_i = \begin{bmatrix} f' & 0 & 0 \\ 0 & f' & 0 \\ 0 & 0 & 1 \end{bmatrix} \tilde{\mathbf{p}}' \quad (1-18)$$

where

$$x_i = p'_x \frac{f'}{p'_z}$$

$$y_i = p'_y \frac{f'}{p'_z}$$

The standard image reference frame places the origin at the top left corner of the image, with the positive x-direction to the right, and the positive y-direction down. This introduces the idea of the principal point, (c_x, c_y) , which is the location where the optical axis of the camera intersects the image plane perpendicularly. In the camera model, the principal point is a translation starting at the image plane's origin (Eq. 1-19).

$$\tilde{\mathbf{x}}_i = \begin{bmatrix} f' & 0 & c_x \\ 0 & f' & c_y \\ 0 & 0 & 1 \end{bmatrix} \tilde{\mathbf{p}}' \quad (1-19)$$

where

$$c_x \approx \frac{W_{image}}{2}$$

$$c_y \approx \frac{H_{image}}{2}$$

Finally, we need to convert the image coordinates, $\tilde{\mathbf{x}}_i$, to pixel coordinates using the pixel scale factor (Eq. 1-20). The pixel scale factor is defined by the parameters k_x and k_y , which represent the number of pixels per unit distance in the x and y directions, respectively. By multiplying the perspective projection matrix by the pixel scale factor, we can obtain a new matrix that maps 3D points in world coordinates directly to pixel coordinates on the image.

$$\begin{aligned}\tilde{\mathbf{x}}_{pix} &= \begin{bmatrix} k_x & 0 & 0 \\ 0 & k_y & 0 \\ 0 & 0 & 1 \end{bmatrix} \begin{bmatrix} f' & 0 & c_x \\ 0 & f' & c_y \\ 0 & 0 & 1 \end{bmatrix} \tilde{\mathbf{p}}' \\ &= \begin{bmatrix} f_x & 0 & c_x \\ 0 & f_y & c_y \\ 0 & 0 & 1 \end{bmatrix} \tilde{\mathbf{p}}'\end{aligned}\quad (1-20)$$

where

$$f_x = k_x f' \text{ and } f_y = k_y f'$$

Are focal distances in units of pixels

At this point, we have placed an object in front of a camera using 3D transformations, and then projected the points of that object onto the image plane using a camera matrix and projective transform. A simple silhouette rasterization of the image would simply fill in the pixel values interpolated between each of the discrete points obtained from this projection. Generating a photo-realistic image would involve coloring, shading, and ray tracing, but this is unnecessary for this dissertation, and will not be discussed.

1.1.3 Image Processing

Digital image processing is a field of computer vision that deals with the manipulation, analysis, and interpretation of digital images. It focuses on algorithms and techniques that extract meaningful information from images and enhance visual quality. We can leverage these algorithms to efficiently and autonomously extract information relevant to model-image registration.

1.1.3.1 Filtering and Convolution

As previously discussed, image formation yields a collection of 2D points, \mathbf{x}_{pix} . We can write the intensity values at each pixel location as a digital signal, $f(\mathbf{x}_{pix}) = f(i, j)$, where (i, j) represents the pixel locations in the image, and the function returns the intensity value. We can then use standard methods of digital signal processing in order to extract meaningful information

from images.

The most widely used filter is a linear filter [116], where the output is some linear operation on the neighboring pixels (Eq. 1-21). This process is known as a *convolution*. In a convolution, the kernel, h , is shifted along the input image, f , and the resultant image, g , is the dot product of those two matrices at that specific location.

$$\begin{aligned} g(i, j) &= \sum_{k,l} f(i-k, j-l)h(k, l) \\ &= \sum_{k,l} f(k, l)h(i-k, j-l) \end{aligned} \quad (1-21)$$

Where we use the following notation

$$g = f * h$$

The convolution operation is *linear shift invariant*, which means that it obeys the superposition principle (Eq. 1-22) and the shift invariance principle (Eq. 1-23). This is a powerful property, because it will behave the same everywhere on the input signal/image (e.g. an edge detector will detect an edge, no matter where the edge is on the input image).

$$h * (f + g) = h * f + h * g \quad (1-22)$$

$$g(i, j) = f(i+k, j+l) \iff (h * g)(i, j) = (h * f)(i+k, j+l) \quad (1-23)$$

A common filter applied to images is the Gaussian kernel (Eq. 1-24). This kernel is shaped as a 2D discrete Gaussian, and has the effect of blurring an image and removing noise.

$$\text{Gaussian filter} = \frac{1}{256} \begin{bmatrix} 1 & 4 & 6 & 4 & 1 \\ 4 & 16 & 24 & 16 & 4 \\ 6 & 24 & 36 & 24 & 6 \\ 4 & 16 & 24 & 16 & 4 \\ 1 & 4 & 6 & 4 & 1 \end{bmatrix} \quad (1-24)$$

Another is the box kernel, which averages the value of the nearest K pixels (Eq. 1-25).

$$\text{Box filter} = \frac{1}{K^2} \begin{bmatrix} 1 & 1 & \dots & 1 \\ 1 & 1 & \dots & 1 \\ \vdots & \vdots & 1 & \vdots \\ 1 & 1 & \dots & 1 \end{bmatrix} \quad (1-25)$$

Edge filters can also be created to detect vertical (Eq. 1-26), horizontal (Eq. 1-27), or diagonal edges (Eq. 1-28). As each of the filters moves across the feature it is designed for, that region of the output will be more highly activated than other regions, extracting out the desired components. The orientation of each of these filters can be hand-selected to find desirable attributes in images.

$$\text{vertical edge filter} = \begin{bmatrix} 0 & 1 & 0 \\ 0 & 1 & 0 \\ 0 & 1 & 0 \end{bmatrix} \quad (1-26)$$

$$\text{horizontal edge filter} = \begin{bmatrix} 0 & 0 & 0 \\ 1 & 1 & 1 \\ 0 & 0 & 0 \end{bmatrix} \quad (1-27)$$

$$\text{diagonal edge filters} = \begin{bmatrix} 1 & 0 & 0 \\ 0 & 1 & 0 \\ 0 & 0 & 1 \end{bmatrix} \text{ and } \begin{bmatrix} 0 & 0 & 1 \\ 0 & 1 & 0 \\ 1 & 0 & 0 \end{bmatrix} \quad (1-28)$$

Lastly, we can use a corner filter to find corners in images (Eq. 1-29).

$$\text{Corner filter} = \frac{1}{4} \begin{bmatrix} 1 & -2 & 1 \\ -2 & 4 & -2 \\ 1 & -2 & 1 \end{bmatrix} \quad (1-29)$$

Entire subfields of computer vision and image analysis are devoted to creating increasingly useful and complex filters, or collections of filters. These include steerable filters, which determine information occurring in arbitrary directions [40], recursive filtering [88], and non-linear filtering [119].

1.1.3.2 Edge Detection

Edge detection is a highly motivated sub-field of image processing in computer vision due to the immense usefulness of algorithmically determining the edges in a given image. For a human operator, it can be relatively easy to identify edges of interest, but how can this be achieved computationally? The first approach might be in viewing an image topographically, with regions of different colors and intensity represented by different “heights”. Then, an edge simply becomes an area with a steep gradient (Eq. 1-30).

$$\mathbf{J}(\mathbf{x}) = \nabla I(\mathbf{x}) = \left(\frac{\partial I}{\partial x}, \frac{\partial I}{\partial y} \right)(\mathbf{x}) \quad (1-30)$$

Finding the direction of the steepest ascent/descent at any given location will give us the normal to the local edge at that point. However, the derivative operator will accentuate and amplify high frequencies in the image, causing noise to overpower the signal. Removing the high-frequency information (a low-pass filter) in the image results in gradient detection that is much more aligned with the salient edges of the image. The Gaussian kernel is a good option for

an isotropic low-pass filter on a 2D signal (image) (Eq. 1-31)

$$\begin{aligned}\mathbf{J}_\sigma(\mathbf{x}) &= \nabla[G_\sigma(\mathbf{x} * I(\mathbf{x}))] \\ &= \nabla G_\sigma(\mathbf{x}) * I(\mathbf{x})\end{aligned}\tag{1-31}$$

where

$$\nabla G_\sigma(\mathbf{x}) = \left(\frac{\partial G_\sigma}{\partial x}, \frac{\partial G_\sigma}{\partial y} \right) = [-x - y] \frac{1}{\sigma^2} \exp\left(\frac{-(x^2 + y^2)}{2\sigma^2}\right)$$

A widely-recognized edge detection algorithm was proposed by John Canny in 1986 [26], and utilizes a five-step process. First, a Gaussian kernel is applied as a low-pass filter (Eq. 1-31). Second, directional filters are used to find the gradients in each direction of the image. Third, a gradient magnitude threshold is applied to remove noise. Fourth, a double threshold is applied to remove both strong and weak edges. Last, edges are determined from hysteresis. The prevailing limitation of this algorithm is the need to set kernel size and edge-intensity.

1.1.3.3 Binary Image Processing

A binary image is a digital image that consists only of black and white pixels. It is often used for labeling or masking an underlying image, where the values of 1 and 0 represent the presence or absence of a particular feature or object. Binary images are often used in computer vision and image processing applications due to low computational overhead and quick analysis. They are also useful for storing and transmitting large amounts of data, as the use of only two values reduces the amount of information that needs to be stored and transmitted.

The primary method of processing binary images is morphological, which involves changing the shape of the “blob” in order to extract useful information from it.

Dilation and erosion are the two main operations that are used in model-image registration (1-32). These functions are each two-fold: first, a convolution operation is applied to the existing binary image, then a threshold is applied to the convolution output to determine if the central pixel is a 0 or 1. If f is the input image, s is the convolution kernel of 1s, and $c = f \otimes s$ is the number of 1s in the convolution output, then dilation and erosion can be expressed in the following way.

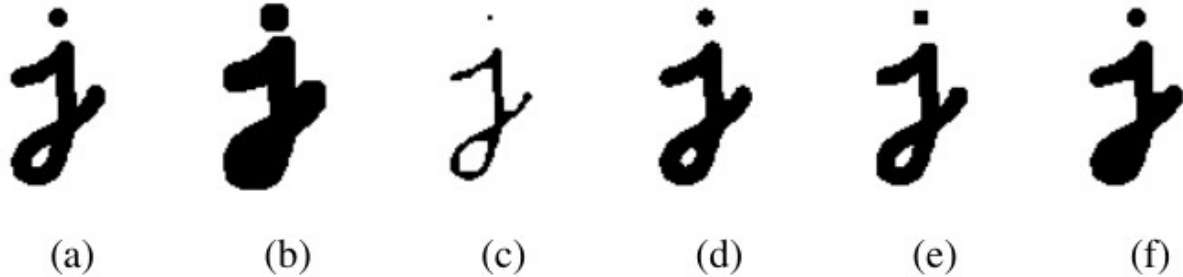


Figure 1-2. A collection of morphological operations on a binary image: (a) original image; (b) dilation; (c) erosion; (d) majority; (e) opening; (f) closing. Image from [116]

$$\begin{aligned} \text{dilate}(f, s) &= \theta(c, 1) \\ \text{erode}(f, s) &= \theta(c, S) \end{aligned} \quad (1-32)$$

Where θ represents a thresholding function.

$$\theta(f, t) = \begin{cases} 1 & \text{if } f \geq t \\ 0 & \text{else} \end{cases} \quad (1-33)$$

1.1.4 Image Similarity Metrics

One of the key components in model image registration is image similarity. This fundamentally involves determining how closely the user's synthetic image matches the actual fluoroscopic image. The choice of similarity metric will be influenced by several key factors, including the a-priori availability of implant/bone geometry and the knowledge of image quality and contrast. Broadly, there are two classes of image similarity when performing model-image registration: intensity-based and feature based.

1.1.4.1 Intensity Based

Intensity based measures are those that utilize specific pixel information in order to determine the difference between two images. This can be either a global image similarity metric or a measure of specific regions of interest within the image.

A canonical difference between two images would be the p-norm separating them

(Eq. 1-34), which iterates through each pixel of the two images and finds the p-norm difference between each pixel pair. Common p-norms are the L_1 norm (*absolute intensity differences* or *mean absolute difference*) [62] ($p = 1$) and the L_2 norm, or Euclidean norm (*squared intensity differences* or *mean squared difference*) [48] ($p = 2$).

$$\|A - B\|_p = \left(\sum_{x=0}^w \sum_{y=0}^h |a_{xy} - b_{xy}|^p \right)^{\frac{1}{p}} \quad (1-34)$$

In Equation Eq. 1-34, A and B are the two images being compared, w and h are the width and height of the images, and a_{xy} and b_{xy} are the intensity values at pixel (x,y) in the two images, respectively.

While conceptually easy to use, the main limitation of p-norm measures is their lack of spatial information. For example, an image that has been shifted by a linear transformation would not score well using a p-norm, despite the two images containing only a minor shift, scale, or rotation. One method for overcoming this limitation is to use the cross-correlation, or sliding dot product, between images [16, 48] (Eq. 1-35). When used in conjunction with projective geometry, this can help locate regions of interest for a model-based registration pipeline. The cross-correlation is calculated using the following equation:

$$\begin{aligned} (A \star B)[x, y] &= E[A_{xy} \cdot B_{x+\tau_x, y+\tau_y}] \\ &= \sum_{\tau_x=-\infty}^{\infty} \sum_{\tau_y=-\infty}^{\infty} a_{xy} b_{x+\tau_x, y+\tau_y} \end{aligned} \quad (1-35)$$

This will determine the regions of each image that are similar, causing the correlation function to “light up” at those areas in a similar way to the convolutional operation between two images. The normalized cross-correlation can also be used (Eq. 1-36), which removes noise coming from each of the original images.

$$\text{normalized cross correlation}(A, B) = \frac{A \star B}{(A \star A)(B \star B)} \quad (1-36)$$

1.1.4.2 Feature Based

Feature based image similarity metrics involve methods for identifying key features in images and using these features to measure differences between two images. These types of methods almost always involve some type of feature-extraction step, where the various features of interest are calculated and determined for subsequent use. The two main classes of features are *keypoints* and *edges*. The simplest method of keypoint detection is using a similar method to intensity-based matching, but having one of the “images” as a patch of the desired feature. With keypoints detected in the input image, one could determine the error of the current pose estimate by taking the Euclidean distance between all image keypoints and all projected keypoints: [24] (Eq. 1-37). With a-priori information about the keypoints, weights could be assigned to each keypoint in order to emphasize specific regions on the image and the model (Eq. 1-38)

$$\text{Keypoint Error} = \left(\sum_{i=0}^N (KP_{image,i} - KP_{proj,i})^2 \right)^{\frac{1}{2}} \quad (1-37)$$

$$\text{Weighted Keypoint Error} = \left(\sum_{i=0}^N w_i (KP_{image,i} - KP_{proj,i})^2 \right)^{\frac{1}{2}} \quad (1-38)$$

Keypoints are particularly useful when there are invariant features in images and 3D models, like morphological aspects of bones. However, if these features cannot be detected, alternative measures must be utilized.

Edges as Features Edges are a natural choice of feature when determining image similarity. Similar to intensity-based image similarity, the similarity between the contours of two images offers a promising metric for determining the overall similarity between two images. In model-image registration, the contours of the input image and the projected model can easily be compared, which presents a reliable scheme for measuring their similarity. When the edges are aligned, we say that the model is *properly registered* to the image. However, how can we determine when the edges are aligned?

As always, the simplest approach is to take the p-norm between the model and image

contours (Eq. 1-34), where instead of taking the difference between the two original images, one is taking the difference of the edges of the images. This function will be minimized when there is complete overlap between image and model contours.

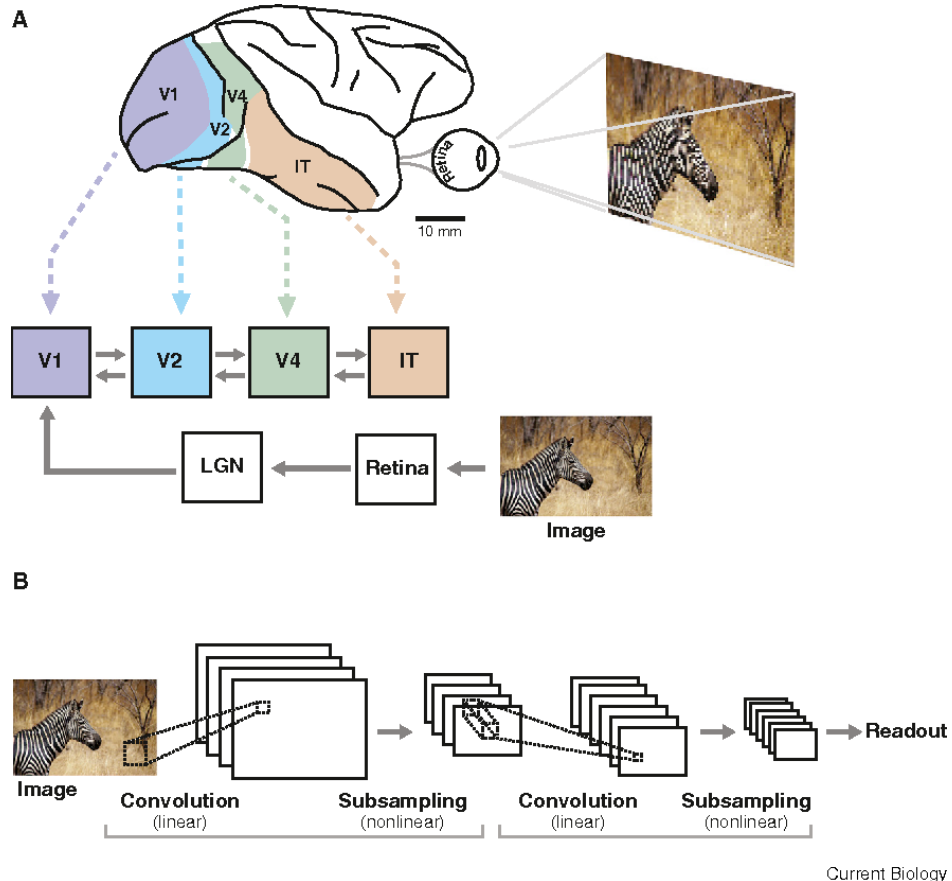
1.1.4.2.1. Drawback of Feature Based Similarity Metrics While they can be much more informative and specific, the main drawback of feature based image similarity metrics is the need for feature selection and extraction from the input image. Historically, this required an immense amount of domain-specific knowledge, and the image processing used to extract those features was often relatively limited in scope.

1.2 Deep Learning for Image Processing in Orthopaedics

A significant limitation of traditional image processing and filtering methods has been the necessity to manually create and fine-tune filters for feature extraction. Although this approach provides researchers with considerable control over filtering techniques, it tends to be time-consuming and challenging to generalize across diverse datasets. Deep learning and neural networks, however, offer algorithms where feature extraction is automated, introducing techniques that enhance the robustness of these algorithms to novel datasets.

1.2.1 The Purpose of Neural Networks for Image Processing

Neural networks in image processing aim to emulate the visual system of animals (Fig. 1-3), creating algorithmic analogies to the physical neuronal pathways used in visual perception. In the human brain, many aspects of our visual system, such as the ability to interpret images regardless of their orientation and extrapolate from known information, are often taken for granted. However, replicating these capabilities algorithmically poses significant challenges. Neural networks alleviate the need for manual feature selection, which has been a limitation of traditional image processing methods. This automation not only simplifies the process but also enhances the ability of these systems to interpret and process images in ways similar to the human brain, making neural networks a powerful tool in the realm of image processing.



Current Biology

Figure 1-3. An example of a neural network mimicking the human brain.

1.2.2 Neural Network Structure

Neural networks generally have the same constitutive elements, mixed and matched based on the desired performance and complexity of the model that you are trying to build.

1.2.2.1 Neural Network Building Blocks

Generally, neural networks are formed by collections of foundational units, which can generate increasingly complex architectures and yield incredible performance. However, it is always important to start with the fundamental “atoms” of the neural network.

The fundamental unit of a neural network is the perceptron (or neuron) (Fig. 1-4), comprising a summation of inputs each multiplied by their respective weights, a bias term, and typically a non-linear activation function.

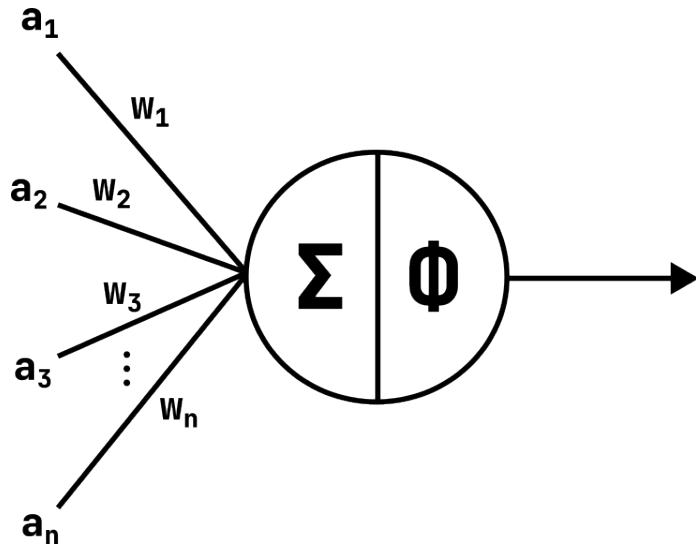


Figure 1-4. A schematic representing a single neuron that receives n inputs and applies ϕ as an activation function.

$$y = \phi\left(\sum_{i=1}^n a_i w_i + b\right) \quad (1-39)$$

Activation functions are a crucial component in neural networks as they allow for the introduction of non-linearity, which is essential for the network's ability to learn complex representations of the input data. Without activation functions, a neural network would only be able to learn linear relationships between the input and output. However, many real-world problems involve non-linear relationships that cannot be captured by a linear model alone. Activation functions provide a way to move beyond a linear relationship, allowing the neural network to learn more nuanced mappings between the input and output. The choice of activation function depends on the specific problem you are trying to solve and the architecture of your network. Some activation functions introduce more non-linearity than others and some trade-off between non-linearity and computational efficiency. Experimenting with different activation functions and observing the impact on the network's performance can be a useful technique for optimizing the performance of a neural network. A list of common activation functions and their equations is shown in Table 1-1.

Table 1-1. A list of activation functions and their corresponding mathematical formula

Activation Function	Equation
Linear	$\phi(x) = x$
Sigmoid	$\phi(x) = \frac{e^x}{1+e^x}$
Hyperbolic Tangent	$\phi(x) = \frac{e^x - e^{-x}}{e^x + e^{-x}}$
Rectified Linear Unit (ReLU)	$\phi(x) = \max(0, x)$
Leaky ReLU	$\phi(x) = \max(0.1x, x)$

1.2.2.2 Fully Connected Network

The fully connected network, also known as the multi-layer perceptron, is a basic type of neural network that utilizes the neurons previously discussed as building blocks. Its schematic representation is a familiar image to many when considering neural networks. By stacking the summations and multiplications of each neuron, we can derive the equation for a single layer of a fully connected network, which is simply a matrix multiplication (Eq. 1-40). In this equation, W represents the collection of weights for each neuron, a represents the input, b represents the bias, and ϕ represents the activation function.

A key strength of this network type is its utilization of non-linear activation functions, enabling the modeling of complex, non-linear relationships in data. A well-chosen activation function can greatly impact the network's performance and ability to achieve specific tasks. For example, in a binary classification task, the sigmoid activation function can be used at the output layer, constraining the output between 0 (false) and 1 (true). The output can then represent the probability of the given input being classified as 'true'. The ReLU activation function is another popular choice because it is computationally efficient and often used in hidden layers of deep networks. Additionally, the hyperbolic tangent (tanh) activation function is used in the context of a model where data follows a Gaussian distribution.

$$y = \phi(W^T a + b) \quad (1-40)$$

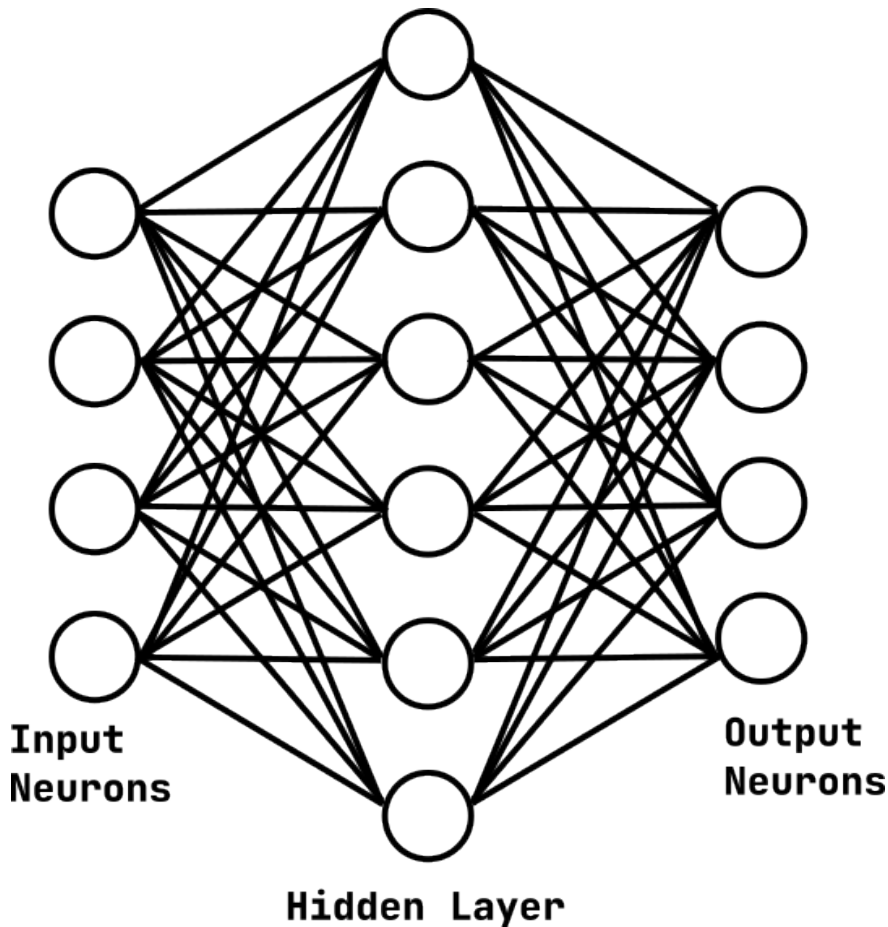


Figure 1-5. A basic fully connected network with a single hidden layer. Each of the neurons are exactly the same as the neurons shown in figure 1-4

Additional layers can be added by taking the output of one layer and sending that into the input of the next. Increasingly complex mappings can be generated by increasing either the size or the number of hidden layers in a network.

$$y = \phi_2(W_2^T(\phi_1(W_1^T a + b_1) + b_2)) \quad (1-41)$$

One of the main limitations of fully-connected networks is exponential increase in computational complexity as your input grows. For a standard 1024×1024 image, you have roughly 1 million input nodes, which can lead to hundreds of millions of parameters that need to be learned depending on the depth of the network. We can use standard image processing techniques to overcome some of these limitations as we explore different network architectures.

1.2.2.3 Convolutional Neural Networks

Alex Krizhevsky significantly renewed interest in deep learning in 2012 by employing a convolutional neural network to win the ImageNet challenge. [105] by more than 10 points over second place. Since then, neural networks have found their way into many different computer vision tasks, including those in the medical field. The power of convolutional neural networks lay in their ability to autonomously extract latent features from images useful for many processing and analysis tasks. The medical field has used them to segment and classify different bones, structures, and pathologies from a wide array of imaging modalities (CT, x-ray, MRI, etc). In most cases, it can completely remove the need for human supervision in many repetitive image processing tasks.

Convolutional neural networks (CNN) utilize the convolution operation (Eq. 1-21) in order to both reduce the size and complexity of the network and capture spatial information present in images. In the same way that the matrix W in the fully connected network is a learnable parameter in a FCN, the individual kernels are the learnable parameters in a convolution operation. In practice, with the correct cost function and optimization routine, this allows each of the kernels to learn the latent structure in the image and make connections between those structures. At a high level, these kernels often represent feature extractors for edges, lines, corners, curves, and other geometric primitives. However, as one traverses deeper into the network, the combinations of these features are often incomprehensible to a human (Fig. 1-6).

Typically, these networks will downsample the image to capture the most salient information, then upsample to regenerate the features from the underlying latent representations. This network architecture has been popularized by the U-Net, which is known as a standard autoencoder (Fig. 1-7). Each of the layers is composed of a collection of convolution kernels, and the downsampling occurs based on the stride or size of the kernel.

CNN architecture can be altered by changing the behavior and structure of the underlying kernels, namely size, stride, and shape. Stride controls the discrete steps the kernel takes as it is moving across the input image and can be used to downsample more aggressively. An atrous

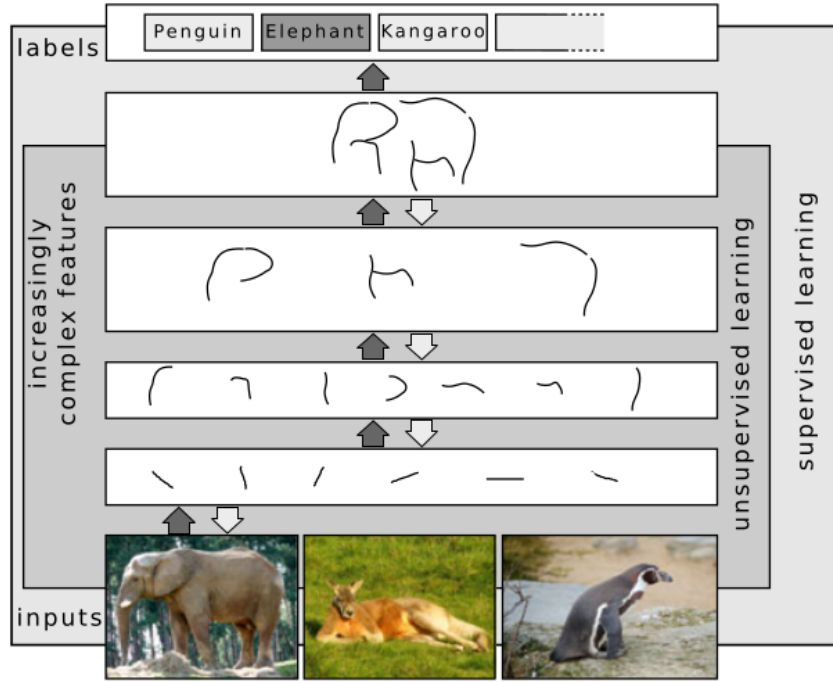


Figure 1-6. An example of extracted features from a convolutional neural network. As shown, the deeper into the network one explores, the combination of core features start to create higher level features that might represent the shape of a specific animal [106].

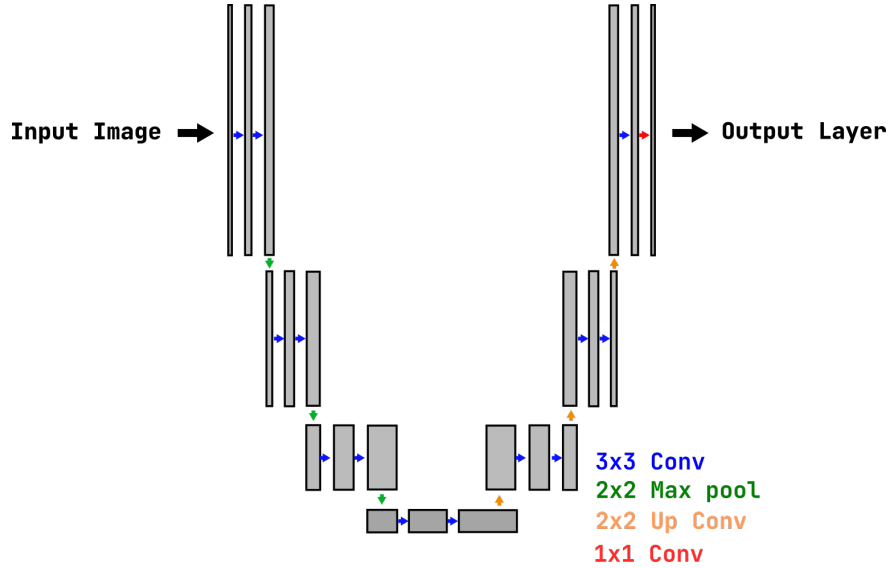


Figure 1-7. A standard U-Net architecture for a convolutional neural network. This architecture is the most common form of network used for biomedical image analysis and processing.

convolution involves internally padding the convolution entries with zeros. This also has the effect of more aggressively downsizing an image and capturing a larger region around the center pixel.

A convolutional neural network can have an additional fully connected network appended to the output in order to learn a mapping that involves a linear combination of the extracted features from the convolution operations. This is often used when a CNN is applied to a classification task, where the total number of outputs of the final FCN is the number of classes.

1.2.3 Training Neural Networks

The power of neural networks is that they are able to “learn” incredibly complex mappings from a set of training data. But how *exactly* do they learn?

1.2.3.1 Neural Network Cost Functions

The initial step in refining a machine learning pipeline is to identify the metric you aim to minimize (or maximize). This metric can encode specific insights about the task at hand, and it can also be used to promote a specific structure in the network itself (parsimony, sparsity, etc).

The **cost function** is exactly the metric that the learning algorithm is attempting to minimize. The application of different cost functions for different tasks in neural networks has been well studied. For regression, typically some type of distance metric is employed (mean absolute error, mean squared error, Kullback-Liebler distance), while classification tasks mostly utilize some type of cross-entropy or log likelihood metric [93].

1.2.3.2 Optimizing and Updating Weights

For convex problems, there often exists a closed-form solution for the parameters that minimize a given objective function. However, neural networks are highly non-linear and non-convex, forcing researchers to employ different methods of updating parameter values in a direction of minimizing the objective function. Backpropagation has emerged as the ubiquitous method for updating these highly non-linear systems [104]. This utilizes gradient descent (Eq. 1-42) and the chain rule (Eq. 1-43) in order to calculate the affect that each node has on the final output, and update it in the direction that maximally minimizes the current error. Researchers can control how aggressive the update is by changing the learning rate, η .

$$w^{(j+1)} = w^{(j)} + \Delta w$$

where

(1-42)

$$\Delta w = -\eta \nabla J(w^{(j)})$$

$$\frac{\partial J}{\partial w} = \frac{\partial J}{\partial e} \frac{\partial e}{\partial \phi} \frac{\partial \phi}{\partial v} \frac{\partial v}{\partial w}$$
(1-43)

One of the main limitations of gradient descent and backpropagation is the need to tune the learning rate. Too small a learning rate will result in extremely slow training of the network and almost always get stuck in local minima. Too large a learning rate can cause the network to “bounce out” of the global minima due to the rate of change being too large. Hyperparameter tuning often presents challenges, frequently relying on methodologies that extend beyond simple trial and error. Some groups have proposed different methods of incorporating dynamically changing update rules in order to incorporate physical properties into the network training stage. The most common is Adaptive Moment Estimation [67], which incorporates Root Mean Squared Propagation [50] and momentum learning.

1.3 Model-Image Registration for Measuring Kinematics from Fluoroscopic Images

3D/2D model-image registration utilizes the computer vision principles discussed previously to determine the position and orientation of the model, given an image containing that model. Relying on the idea that the projective scheme of the real-world camera can be emulated, then the goal is to find some type of similarity metric (Section 1.1.4) between a projected 3D model (Eq. 1-18, Section 1.1.2) and the existing image such that minimizing this metric indicates that our object has been “placed” correctly. Many different branches of computer vision and optimization have been explored for determining the kinematics of total knee arthroplasty components, each with varying levels of computational intensity, objective function (via image similarity), and optimization routine. General groupings of each will be discussed here, along with pitfalls and limitations that prevent the technique from being applicable in a clinical setting.

1.3.1 Pre-Computed Projective Geometries

Early methods of model-image registration were constrained by the limited computational resources available at the time. This forced researchers to find clever ways to determine image similarity metrics without the need to iteratively compute the projective geometry of the model thousands of times per second.

First established in the early 70s [95, 101, 121, 122], normalized Fourier descriptors provide a way to normalize 2-dimensional images using information from the latent 3D characteristics (position and orientation). This was used to determine TKA kinematics to high levels of accuracy [8, 9], so long as 3D shape information was known, and the camera matrix could be deduced. The employed image similarity metric was the L_2 difference between the normalized Fourier descriptors of the input image and the precomputed shape library at known rotations. Further interpolation was used to increase accuracy significantly.

In parallel, another group utilized pre-computed distance maps intrinsic to the 3D model [75, 137]. These distance maps could then be used to quickly determine the Euclidean distance between any node in the model and an arbitrary line in 3D space. Then, 3D vectors were created starting at sampled points along the contour of the implant, and concluding at the origin of the camera. Assuming an accurate focal distance, then the objective is simply minimizing the distance between all the vectors and their corresponding nearest node on the 3D model. Once minimized, the 3D object fell into the “slot” carved out for it by the pseudo-conical shape.

The main issue with these pre-computed geometries is need for the researchers to hand-select the contours belonging to the implant. Despite the recently available Canny edge-detector [26], one still needed to hand-label the specific edges of interest. This would be far too time consuming in a clinical setting.

1.3.2 Motion Capture

Motion capture is a common method in computer vision involving the tracking of reflective markers using multiple cameras to over-determine the location of the markers. Then, if the position of the markers relative to anatomic features is known, a series of transformation matrices

can be used to determine the location of the anatomic features, given the measurable location of the markers. Historically, this has taken two different approaches, skin-mounted and bone-mounted.

Skin mounted markers rely on a set of fiducial points on the body that are closely related to joint centers, such that relative translations and rotations can be resolved. However, there have been numerous studies showing that skin-motion during activity leads to high levels of inaccuracy at the joint [44, 45, 72, 78]. Such inaccuracies render this method clinically impractical for accurate measurement of joint kinematics.

Other groups have taken a much more accurate approach: drilling bone pins into the joints of interest and attaching motion-capture reflectors to the end of the pins [74]. While extremely accurate, this method is far too invasive and time consuming for a clinical setting.

1.3.3 Iterative Projections

Increased computational performance and widespread availability allowed for different types of methods of model-image registration that were previously untenable due to computational complexity. One of the main areas that saw increased speed-ups were in parallel computing, which drastically increased computer graphics performance. By leveraging improved computer graphics pipelines, researchers were able to project and render 3D implants in near real-time and perform image similarity metrics quickly. This seemingly overcame the need for pre-computed projection schemes.

Different groups have achieved strong performance using simulated annealing with direct image-to-image similarity metrics [81], and Lipschitzian optimization using contour matching [39]. Although powerful and rapid, these methods still depend on human supervision to escape local minima and set an initial pose estimate. Noisy images and the need to set hyperparameters for the edge detection scheme also reduce the scope of generalization to new data in a clinically practical way.

1.3.4 Fully Human Supervised

One of the more dominant softwares in measuring joint kinematics is JointTrack, which utilizes the strongest neural network available (the human brain) connected to one of the most dexterous manipulators available (the human hand) to make accurate measurements of joint kinematics from single-plane images [86]. This software works by accurately recreating the fluoroscopic system's projective matrix and allowing users to manipulate a 3D model of the desired bone or implant to align it with the provided image.

There were additional views that allowed the user to see the alignment from the coronal plane, as well as graphs demonstrating the kinematics throughout the movement, which allowed abnormal frames to be identified and dealt with quickly.

Hundreds of papers have been published using this software as the method for determining kinematics, and it has been extensively validated using many different methods offering ground-truth solutions to kinematics. The primary challenges with this method include the substantial time required for user training and the need for continuous human supervision during the measurement process.

1.3.5 Biplane Kinematics Measurements

One of the most effective methods for resolving single-camera limitations in measuring kinematics is to add a second camera! This offers much greater accuracy and resolution, especially when determining out-of-plane translations, because the out of plane translation for one camera is an in-plane translation for the second.

The groups that have used this have cited sub-mm and sub-degree accuracy for all translations and rotations [6, 24, 132], and have used a wide variety of optimization routines and image similarity metrics.

While this seems extremely promising, the general cost and unavailability of bi-plane fluoroscopic imaging systems presents a problem for integrating this technology into a clinical setting. For kinematic analysis to achieve widespread clinical adoption, it must be seamlessly integrated into the imaging systems present at most hospitals and clinics, which is single-plane

systems. However, the accuracy of bi-plane systems can be used to validation of performance for various single-plane pipelines [21].

1.3.6 Roentgen Stereophotogrammetric Analysis

Roentgen Stereophotogrammetry is one of the most accurate methods of measuring implant kinematics, popularized in the early 1970s [109]. Most often, it is used to determine implant micromotion in post-operative followups due to the extremely high resolution at which it measures pose and orientation. This method utilizes highly radio-opaque tantalum beads of known shape and size implanted on and adjacent to the implants. Using methods akin to motion capture, algorithms can determine the location of tantalum beads with extreme accuracy, providing a good estimate for the location of the implant to which they are attached.

The largest limitation of this method is two-fold (1) the need for additional surgical steps precludes this from being a widely applied method, and (2) the need for biplane imaging system poses a problem to availability and portability.

1.4 Automating Measurements of Kinematics from Fluoroscopic Images

The proposed method overcomes the various limitations of previous attempts to autonomously measure kinematics from single plane fluoroscopy. The key feature of all these limitations is that they prevent the adoption of this technique in a clinical setting, due to the labor overhead or equipment required in order to generate an accurate kinematic report. The proposed combination of methods will alleviate these requirements, and the extensibility of the software will allow this technology to be used in a clinical setting without disrupting the standard clinical workflow.

1.4.1 Autonomous Implant Detection

Determining the location of an object in an image is a historically intractable problem. These are one of those tasks that are often relegated to the corner of “easy for humans, extremely difficult for computers”, especially when there is very little a-priori information available. However, as discussed in Section 1.2, deep learning has paved the way for computer vision programs to be able to perform tasks that were once only possible by humans. Two convolutional

neural networks were trained to segment that tibial and femoral components from the single plane fluoroscopic images. The network architecture used was the High-Resolution Net [123], which leverages low-level features with higher resolution parallel processing in order to better determine the spatial characteristics of the image and produce a better output. At the time of writing, this network sets the state-of-the-art standard for performance on the COCO and ImageNet datasets, demonstrating robustness for use in many different arenas.

Many of the historic methods of determining kinematics were limited by the researchers ability to quickly and reliably determine the location in the implant. The contours were either hand-segmented [8, 137], or a normal edge detector was used, which introduces extra tuning parameters for any given study due to variations in image quality.

1.4.1.1 Neural Network Robustness

One of the main problems with neural networks is overfitting. With millions of parameters to tune, it can be extremely easy to “overfit” on your training set, leading to the network’s inability to perform well on any image that was not directly in the training set. When dealing with fluoroscopic images, this might look like a neural network that can perform extremely well on high-quality, high frame rate, low blur images from a hospital that has a budget to support such a machine, while failing to segment images from a machine more than a decade old. We overcame this challenge through a mixture of additional image augmentations [25] and using a wide range of training data. The neural networks were trained on roughly 8000 images from 7 different human-supervised total knee kinematics studies spanning the last two decades. The image qualities range from extremely clear and high quality to nearly indiscernible without intense human supervision. The goal of this two-pronged approach was to have both artifical and real “low quality” images for the network to train on so that any hospital or researcher, regardless of the available equipment, might be able to leverage this technology in their practice. The authors hope that this approach provides equal access to this informative measurement.

1.4.2 Initial Pose Estimation

Hand-in-hand with implant detection is the initial pose estimate that very often needs to be input into the optimization routine. Once the contour of the implant was determined, many methods required a human operator to place the implant in the “capture region” of their optimizer in order for it to eventually find the correct solution. This takes human supervision to get correct, thus adding another impediment toward getting this technology into the clinic.

To determine an initial estimate, we must rely on those methods that can leverage information present in the camera projection (Section 1.1.2) and the 2D CNN output (Section 1.4.1). The primary method that takes advantage of this information utilizing normalized fourier descriptor shape libraries, and extracting each of the 6 degrees-of-freedom from either the normalized coefficients or matching with the closest entry in the library [8, 9, 121, 122]. The key feature that makes this method tractable for autonomous measurements is the availability of the implant pixels from the convolutional neural network.

1.4.2.1 Generating Normalized Fourier Descriptors

The Fourier Transform is one that takes in a continuous and repeating function and represents it as a sum of sinusoidal signals. Because the implant contour is self intersection, we can view it as a continuous function that has period 2π radians, as it will loop back onto itself and start over. This allows us to take advantage of the Fast Fourier Transform (FFT) [31], which operates on a discrete set of points rather than a continuous function. First, the contour of the segmented implant is taken then resampled into 128 equi-spaced points. The choice of 2^n points allows the FFT algorithm to perform much more quickly than another choice of points. Each contour point on the image (x, y) is then represented as a single complex point, $x = jy$, such that the 1D FFT algorithm can be used. If $s(n)$ represents the complex sequence of equi-spaced contour points in the implant, and $S(i)$ represents the frequency-domain representation of those points after the FFT is applied, then we can represent these functions as shown in Eq. 1-44.

$$\begin{aligned}
S(i) &= \sum_{n=-\frac{N}{2}+1}^{\frac{N}{2}} s(n)e^{-j(2\pi in)/N} \\
&\text{for } -\frac{N}{2} + 1 \leq i \leq \frac{N}{2} \\
s(n) &= \frac{1}{N} \sum_{i=\frac{N}{2}+1}^{\frac{N}{2}} S(i)e^{j(2\pi in)/N} \\
&\text{for } -\frac{N}{2} + 1 \leq n \leq \frac{N}{2}
\end{aligned} \tag{1-44}$$

As discussed in Section 1.1.4, spatial information in images is difficult for computers to understand without explicit calculation. So, we use the properties of the FFT to normalize each of the shapes based on location, rotation, and size in order to accurately compare the segmented mask to a generated library.

Normalize Position By the properties of the FFT, we know that $S(0)$ is the geometric centroid of the contour. Thus, we can set this to zero for all contours to give a consistent reference point that is independent of the location of the input contour. We can save this value as the “position normalization coefficient” to determine the (x,y) location of the implant later in the process. And, because of our usage of the 1D FFT, we know that the real portion of this coefficient is the x-value and the imaginary portion is the y-value.

$$\text{Position Coefficient} \leftarrow S(0) \tag{1-45}$$

$$S(0) = 0$$

Normalize Size Because the implant is not self-intersecting, we know that $S(1)$ is the coefficient with the largest size, and it also represent the scale of the shape of the implant. So, we can normalize each shape by dividing each coefficient by the overall size of the contour, shown below.

$$\begin{aligned}
\text{Size Coefficient} &\leftarrow |S(1)| \\
S(i) &= \frac{S(i)}{|S(1)|} \\
&\text{for } -\frac{N}{2} + 1 < i < \frac{N}{2}
\end{aligned} \tag{1-46}$$

Normalize In-Plane Rotation and Contour Starting Point One of the most difficult parts of measuring the similarity between two contours, especially when they are composed of a set of discrete points, is that any distance measurement necessarily takes into account those discrete points in the order that they are presented. To illustrate this example, imagine two squares, each defined by the location of the corners A_i, B_i, C_i, D_i . If these two squares are perfectly overlapping, one might imagine that the Euclidean distance between each of the points, $(\sum_{P \in A, B, C, D} (P_1 - P_2)^2)^{\frac{1}{2}}$ would be equal to zero. This would only be true if the starting point of the contour was the same for each square (e.g. Corner A was always the top left corner). If each square had A starting in different locations, then even when the contours are perfectly aligned, the distance metric would be non-zero and uninformative.

We can use properties of the FFT to normalize the starting position of the contour in each of the segmentations as well as the general orientation of the contour. We can leverage the starting point shift property of the fourier transform (Eq. 1-47) and the rotation property (Eq. 1-48) in order to normalize both of these factors and ensure that similar shapes have the same orientation and starting point.

$$s(n - T) \xrightarrow{DFT} S(i)e^{-jiT} \tag{1-47}$$

$$s(n)e^{j\theta} \xleftrightarrow{DFT} S(i)e^{j\theta} \tag{1-48}$$

To normalize the starting point and rotation, we find k such that $S(k)$ is the coefficient of second largest magnitude. We then apply a mixture of the starting point shift and the rotation property of the FFT to orient each contour (Eq. 1-49). We also want to find the “rotation

normalization coefficient”, which is the angle through which the contour needs to rotate to reach the normalized orientation. This is done by determining the phase of the normalization equation at $i = 0$, which controls the overall orientation of the contour. If u is the phase of $S(1)$, and v is the phase of $S(k)$, then we can find the normalized orientation.

$$\begin{aligned} \text{Rotation Normalization Coefficient} &\leftarrow \frac{v - ku}{k - 1} \\ S(i)_{norm} &= S(i)e^{j\frac{(i-k)u + (1-i)v}{k-1}} \\ \text{for } -\frac{N}{2} + 1 \leq i \leq \frac{N}{2} \end{aligned} \quad (1-49)$$

Once the in-plane rotations have been normalized, the contour has been completely normalized for x, y, z translations and z rotations. And, by storing these values, we are able to utilize them in determining an initial pose estimate. Then, we can use a library made up of known x, y rotations, and compare the segmentation to this library to determine all 6 degrees-of-freedom.

1.4.2.2 Shape Library

A shape library is created using a flat panel projection (Section 1.1.2) of the implant at known x and y rotations, while holding all positions and orientations constant, then applying the normalization protocol described above to determine the normalized coefficients of each library entry. If $s_{x,y}(n)$ is the flat-panel projection of the implant with x and y rotations, then we can generate a library using the following procedure, where FFT is the fast fourier transform (Eq. 1-44) and NFD is the process of normalizing the contour and extracting the relevant coefficients (Section 1.4.2.1).

$$S_{x,y}^{lib}(i) = NFD(FFT(s_{x,y}(n))) \quad (1-50)$$

Once the shape library is generated for a specific implant, we can start to determine the pose estimates for each degree of freedom.

1.4.2.3 Generating a Pose Estimate

First, we compare the Euclidean distance of the normalized segmentation contour to each value of the shape library; the x and y rotations that minimize this function are taken as the x and y rotations of the implant (Eq. 1-51).

$$(\theta_{x,est}, \theta_{y,est}) = \operatorname{argmin}_{x,y} \left(\sum_{i=-\frac{N}{2}+1}^{\frac{N}{2}} (S^{seg}(i) - S_{x,y}^{lib}(i))^2 \right)^{\frac{1}{2}} \quad (1-51)$$

Then, we can determine the z rotation estimate by comparing the values of the normalized θ values that were needed in Eq. 1-49. This process is shown in Eq. 1-52.

$$\theta_{z,est} = \theta^{seg} - \theta_{x,y}^{lib} \quad (1-52)$$

where $\theta^{seg,lib} \equiv$ Rotation Normalized Coefficient

We can then use the principals of projective geometry (Fig. 1-1) and similar triangles to determine the out-of-plane translation of the implant, given that the library was projected at a known depth. Using similar triangles, we are able to determine that the depth is inversely proportional to the overall magnitude of the projection, captured by the “Size Coefficient” (Eq. 1-53). We also make the assumption that we have a weak perspective projection, meaning that the out-of-plane translations are small compared to the focal length of the fluoroscopy imaging setup.

$$\begin{aligned}
\frac{M^{seg}}{f} &= \frac{h}{z_{est}} \\
\frac{M^{lib}}{f} &= \frac{h}{z_{lib}} \\
&\rightarrow \\
z_{est} &= \frac{M^{lib}}{M^{seg}} z_{lib}
\end{aligned} \tag{1-53}$$

where

$M^{seg,lib}$ \equiv Size Coefficients

$h \equiv$ Implant Size

The x and y translations can be determined using the value of the z translation estimate, along with the location of the centroid, saved as the “Position Coefficient”. This is then refined further to account for the rotation of the implant and the distance of the implant’s centroid to its origin. We can express this with a single matrix multiplication multiplied by a scale factor (Eq. 1-54).

$$\begin{pmatrix} x_{est} \\ y_{est} \end{pmatrix} = \begin{pmatrix} Re(S^{seg}(0)) \\ Imag(S^{seg}(0)) \end{pmatrix} - \begin{pmatrix} \cos(\theta_z) & -\sin(\theta_z) \\ \sin(\theta_z) & \cos(\theta_z) \end{pmatrix} \begin{pmatrix} Re(S_{x,y}^{lib}(0)) \\ Imag(S_{x,y}^{lib}(0)) \end{pmatrix} \times \begin{pmatrix} \frac{z_{est}}{z_{lib}} \end{pmatrix} \tag{1-54}$$

Once this step is complete, we have accounted for x and y rotations (Eq. 1-51), z rotations (Eq. 1-52), x and y translations (Eq. 1-54), and z translations (Eq. 1-53). This provides a robust initial estimate when the only information available is the implant geometry and the segmentation output from the neural network. Furthermore, this can be done without any human supervision, providing a fully autonomous initialization for any pose refinement strategy, so long as the estimate is within the convergence region.

1.4.3 Objective Function

In a perfect situation, our objective function would directly measure the error between our 3D model’s current pose and the true pose of the object. However, if we had a-priori access to the

true pose of the object, then this entire pipeline would be worthless. Thus, we must find an objective function that can act as a heuristic for the difference between true pose of our model and the current pose of our model. Our access to the segmentation output from the CNN and the ability to project the silhouette of our model quickly makes contour comparison a natural choice for an objective function. The only assumptions that we make are (1) our projective algorithm and camera definition are the same as the camera that was used to take the original fluoroscopic image and (2) our 3D model is the same 3D model that is present in the image. If these two assumptions are correct, then the alignment of the image contour and the projected contour necessarily means that our pose is correct, unless you have a symmetric object (Section 2.2).

First, we apply a Canny edge detector [26] to extract the edges from our segmentation contour, S , and our projected 3D model, P , where edges are 1, and every other pixel is 0. We can then iterate over each pixel and take the absolute values of the L_1 norm between our segmented and projected contours (Eq. 1-55).

$$J = \sum_i^{Height} \sum_j^{Width} |S_{ij} - P_{ij}| \quad (1-55)$$

Unfortunately, the contours of the projected model are extremely sensitive to pose, especially when representing angles using Euler decomposition. This results in a chaotic similarity function that has an extensive amount of local minima. Past methods have overcome this by dilating the contour of the projected image (Eq. 1-32) and performing the same L_1 optimization routine. However, a lack of an isolated contour for the fluoroscopic image still lead to a slightly noisy objective function. Our proposed method takes advantage of the segmentation output for the neural network and dilates both the segmentation contour and the projected contour for a much smoother objective function allowing for a wider search range. As our objective function is minimized, we can decrease the level of dilation to return the metric back into its original form, which most accurately describes the difference between the projection and image.

1.4.4 Optimization Routine

Broadly, optimization is the process of minimizing or maximizing an objective function, $f(\mathbb{R}^n) \rightarrow \mathbb{R}$, potentially subject to some constraints (e.g. $x \in \Omega$) [5]. We formalize this below (Eq. 1-56). The simplest optimization problems have an analytic form of the gradient of f that can be solved directly, typically by setting the first derivative to zero (e.g. least squares).

$$\operatorname{argmin}_x \{f(x) : x \in \Omega\} \quad (1-56)$$

A drawback to our pipeline is that there is no analytic form of the objective function between each segmentation and projected contour; they must be resampled over a specified range in order to approximate objective function values and gradients. This defines a *black box* optimization routine, which is well studied in the literature [5]. In this type of function, it is not possible to use gradient-based methods to determine a minimum value for the objective function, one must use heuristics or ad-hoc methods to find the minimum location. Lipschitzian optimization offers an appealing black box optimization approach because it satisfies our need for a global search algorithm with provable convergence. First, we start with the definition of Lipschitz continuous, which places bounds on the rate of change of a function specified by some constant, called the Lipschitz constant. With a known Lipschitz constant, it is possible to find the value for the global minimum of optimization function [36].

Definition 1-1 (Lipschitz Continuous). *The function g is said to be Lipschitz Continuous on the set $\mathbf{X} \in \mathbb{R}^n$ if and only if there exists a scalar $K > 0$ for which*

$$\|g(x) - g(y)\| \leq K\|x - y\|$$

for all $x, y \in \mathbf{X}$

*The scalar K is called the **Lipschitz Constant** of g relative to the set \mathbf{X} .*

We can illustrate this convergence with a simple example: consider the function

$f(x) \rightarrow \mathbb{R}, x \in [a, b]$. If we know that the function is Lipschitz continuous, the following conditions are true on the domain $x \in [a, b]$. This corresponds to the positive and negative slopes, K , applied to the extrema of the domain, and the intersection, x is selected as the choice for subdivision. This process is repeated, where the region is further subdivided based on the lowest value of $f(x_i)$. The iterative process is stopped once the difference between successive domain splitting is below a pre-specified global tolerance.

$$\begin{aligned} f(x) &\geq f(a) - K(x - a) \\ f(x) &\geq f(b) + K(x - b) \end{aligned} \tag{1-57}$$

While powerful, a-priori knowledge of the Lipschitz constant is needed for determining the global minima. Without it, there is no way of determining intersection points, and no way of selected new regions for subdivision and sampling. Shubert's Algorithm also has slow convergence, due to the inability to define parameters for when to explore local vs. global search. The Lipschitz constant, K , acts as a weight that places larger emphasis on global serach when high, and local search when low.

Fortunately, methods exist for utilizing the power of Lipschitzian optimization without the need for explicit knowledge of the Lipschitz constant [60]. These can both overcome the need for an a-priori knowledge of the Lipschitz constant, as well as offer some solutions of the slow convergence by providing methods for exploiting both local and global search simultaneously to find the minimum function values.

Jones et al. [60] propose a method by which the center, c , of a domain is sampled, rather than the endpoints. This produces the equations below (Eq. 1-58). The inequalities represent slopes $+K$ and $-K$, respectively, and provide a maximum value for the lower bound of the function at the endpoints, a and b . The midpoints of $[a, c]$, and $[c, b]$ are then calculated and the process is then repeated (Fig. 1-9). The power of this method is that you can determine potentially optimal regions of the domain by choosing those points along the lower convex hull of the graph plotting sub-domain size vs center point function value. The points along this hull are

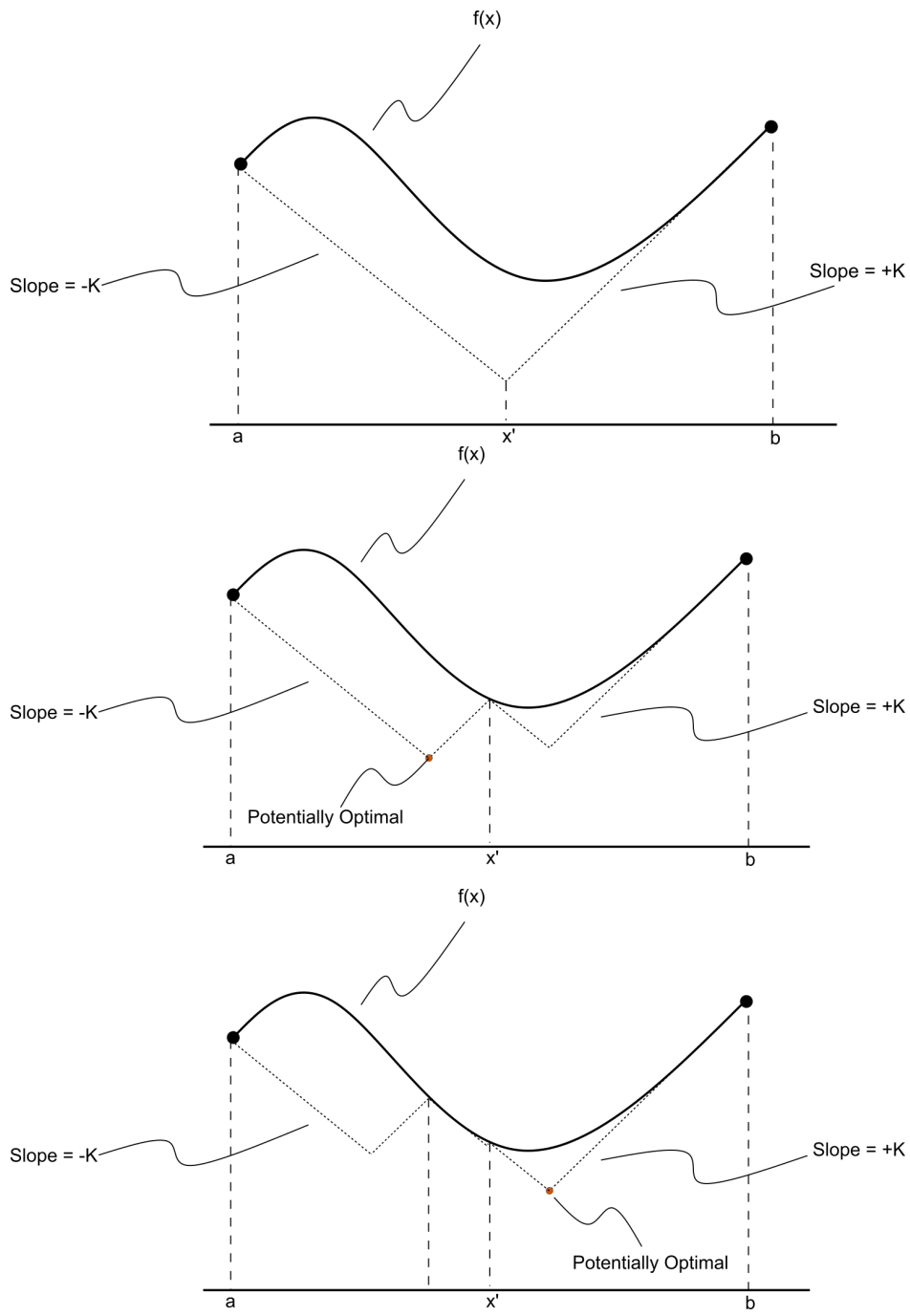


Figure 1-8. A visual representation of Shubert's algorithm, which finds the global minima iteratively through a repeated calculation of the intersection of two lines with slope $\pm K$. If K is known, it will always find the global minimum.

those that could potentially include the function minimum, and each is chosen for further sub-sampling (Fig. 1-10). Determining the convex hull is a problem well studied in the literature [15, 30, 46, 56]. This elegantly mixes local vs. global search, and drastically increases the speed of convergence.

$$f(x) \geq \begin{cases} f(c) + K(x - c) & \text{if } x \leq c \\ f(c) - K(x - c) & \text{if } x \geq c \end{cases} \quad (1-58)$$

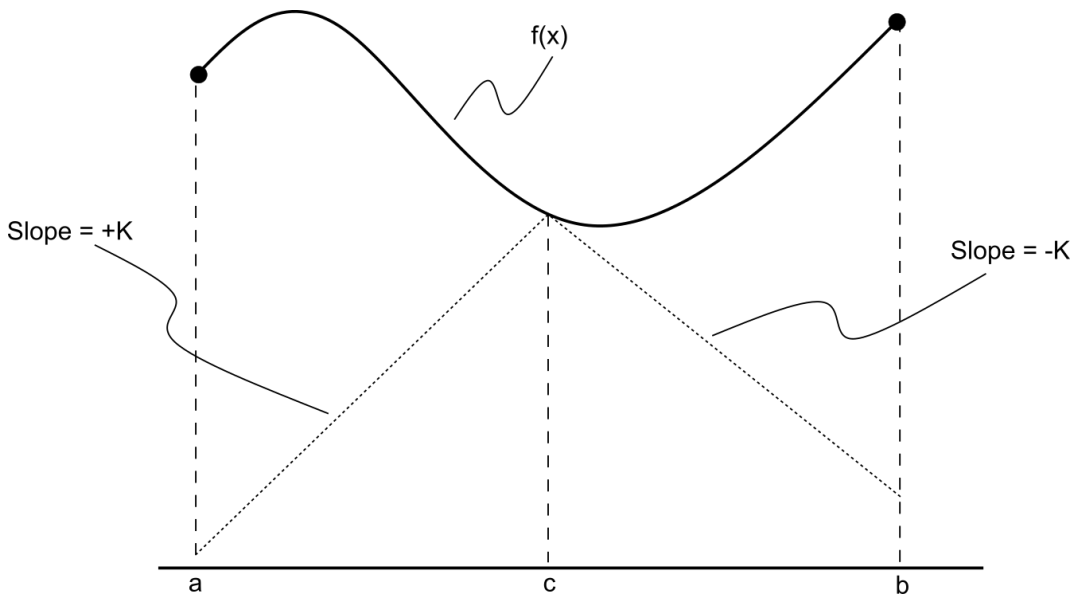


Figure 1-9. The DIviding RECTangles (DIRECT) algorithm in one dimension. It can find the global minimum of a function without a-priori knowledge of the Lipschitz constant. The value of the line with slope $\pm K$ at each of the end-points represents the theoretical minimum for the value of the function in that region. Thus, the size of the region and the value of the function at the center help the algorithm determine potentially optimal sub-regions.

This can be extended into multiple dimensions without loss of generality. First, each dimension in the domain is normalized to the range $[0, 1]$, and a hypercube is created in \mathbb{R}^D , where D is the dimension of the domain you are searching. The first iteration trisects this hypercube along an arbitrary dimension, and further iterations trisect along the largest dimension of the hypercube. We select potentially optimal hypercubes by identifying points along the lower convex hull of the graph plotting hypercube size vs center point function value.

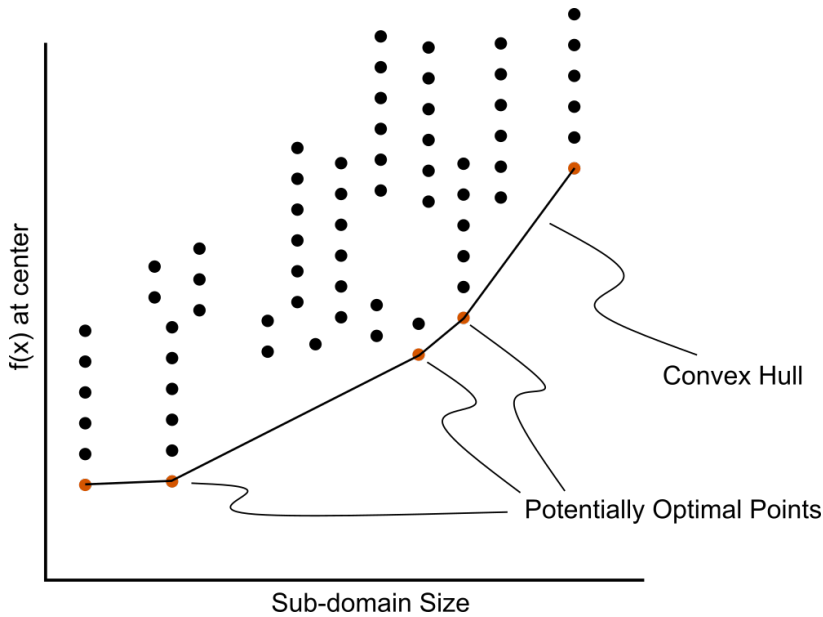


Figure 1-10. The potentially optimal regions of the DIRECT algorithm are those points that lay along the lower convex hull of the scatter plot of sub-domain size vs function value at center. This is due to those regions being the locations where the maximum possible rate of change in the function might be a minimum, without any prior knowledge of the Lipschitz constant.

For our purposes, we construct a hypercube along each of the 6 degrees-of-freedom that describe the pose of the implant in space, using bounds set by the user. The first epoch involves minimizing the objective function with larger bounds and a larger dilation. After all iterations have been used up, the algorithm is re-started with a smaller dilation and tighter bounds. The last epoch typically has the tightest bounds and no dilation. This pyramidal scheme offers a smooth objective function when the bounds are largest, which assists in escaping local minima, and an aggressive objective when the bounds are tight, and fewer local minima are present.

1.4.5 Overcoming Single-Plane Limitations

Despite a fully autonomous solution for measuring total knee arthroplasty kinematics, there are some fundamental limitations when using monocular vision to determine the three dimensional position and orientation of an object. Section 2.2 discusses methods for overcoming these limitations. So far, incorporating digital ligaments into the cost function has been used to a great deal of success.

CHAPTER 2

THE AIMS OF THIS DISSERTATION

2.1 Aim 1: JointTrack Machine Learning: An Autonomous Method of Measuring 6-DOF TKA Kinematics from Single-Plane Fluoroscopic Images

The primary aim of this dissertation is to test the feasibility of the fully autonomous pipeline, and validate the results against known gold-standard kinematics measurements to test reproducibility and accuracy. These measures are discussed and quantified in the attached paper (Chapter 3). The work presented in this aim won the HAP Paul Award for Best Paper at the International Society for Technology in Arthroplasty's 2022 Annual Meeting, and is published in the Journal of Arthroplasty.

2.2 Aim 2: Correcting Symmetric Implant Ambiguity in Measuring Total Knee Arthroplasty Kinematics from Single-Plane Fluoroscopy

While establishing a pipeline for the fully autonomous measurements of TKA kinematics, we encountered many of the different limitations present in using single-plane fluoroscopy. Fundamentally, this is a problem that exists inherently in the system, as you have a severely underconstrained problem, leading us to the inverse problem of computer vision (Definition 2-1).

Definition 2-1 (Inverse Problem). *The inverse problem in computer vision is the process of calculating the causal factors (kinematics) the produced a set of observations (fluoroscopic images).*

One of the more pernicious limitations in single-plane fluoroscopy is an issue that we've dubbed the "symmetry trap", which causes multiple global minima when using a strictly contour-based objective function. The major contributor to these issues is symmetric tibial implants, which are mediolaterally symmetric (i.e. no different between right and left implants).

Definition 2-2 (Symmetry Trap). *A symmetry trap occurs when a symmetric object has a projective geometry with more than one unique pose that can produce it. The simplest case is*

a sphere, where all poses produce the same circular projective geometry.

This aim focuses on establishing a post-processing pipeline that can be used to address symmetry traps fully autonomously, solving an issue facing researchers studying single-plane kinematics for nearly 30 years! We also propose imaging recommendations to reduce the occurrence of symmetry traps in clinical data.

The work presented in this aim is currently under review for publication in the Journal of Biomechanics.

2.3 Aim 3: Musings on Latent Kinematics Space and Synthetic Biomechanics Data

The third aim of this thesis aims to express some of the non-publishable thoughts that the author has on his attempts to define a robust “kinematics translator”, which would, for example, “translate” a patients “stair rise” kinematics into “walking” kinematics. Additionally, the author explores many of the issues in the lack of standardization among different groups measuring TKA kinematics, and why that lack of standardization will make consistent clinical applications difficult. He hopes this chapter is useful for others in this space to establish research protocols that can bring kinematics into both the clinical sphere and the “big data” world.

Ultimately, the hope is that there can be a standard operating procedure for measuring kinematics, such that the resultant measurements have post-operative predictive power with respect to function, stability, and modes of failure.

2.4 Aim 4: This Will Definitely Work on Shoulder Implants, Right?

The final aim outlines the process of applying the autonomous kinematics measurement platform to total shoulder arthroplasty (TSA) implants. Major shortcomings are discussed, as well as multiple avenues forward that bring analysis down to geometric first principles.

The final section of this aim is under preparation for submission to publication.

CHAPTER 3

JOINTTRACK MACHINE LEARNING: AN AUTONOMOUS METHOD OF MEASURING 6-DOF TKA KINEMATICS FROM SINGLE-PLANE FLUOROSCOPIC IMAGES

Total Knee Arthroplasty (TKA) is a standard procedure for alleviating symptoms related to osteoarthritis in the knee. In 2018, orthopaedic surgeons performed more than 715,000 TKA operations in the United States [2]. This number is projected to increase to 3.48 million by 2030 [73] due to an aging population and increased obesity rates. While TKA largely relieves symptomatic osteoarthritis, roughly 20% of TKA patients express postoperative dissatisfaction, citing mechanical limitations, pain, and instability as the leading causes [7, 18, 107]. Standard methods of musculoskeletal diagnosis cannot quantify the dynamic state of the joint, either pre- or post-operatively; clinicians must rely on static imaging (radiography, MRI, CT) or qualitative mechanical tests to determine the condition of the affected joint, and these tests cannot easily be performed during weight-bearing or dynamic movement when most pain symptoms occur. Unfortunately, most of the tools used to quantify 3D dynamic motion are substantially affected by soft-tissue artifacts [44, 78, 113], are prohibitively time-consuming or expensive [34], or cannot be performed with equipment available at most hospitals.

Model-image registration is a process where a 3D model is aligned to match an object's projection in an image [22]. Researchers have performed model-image registration using single-plane fluoroscopic or flat-panel imaging since the 1990s. Early methods used pre-computed distance maps [75, 137], or shape libraries [8, 121, 122] to match the projection of a 3D implant model to its projection in a radiographic image. With increasing computational capabilities, methods that iteratively compared implant projections to images were possible [39, 79, 81]. Most model-image registration methods provide sufficient accuracy for clinical joint assessment applications, including natural and replaced knees [13, 14, 24, 70], natural and replaced shoulders [66, 80, 84, 114], and extremities [27, 28, 35]. One of the main benefits of this single-plane approach is that suitable images can be acquired with equipment found in most hospitals. The main impediment to implementing this approach into a standard clinical workflow is the time and expense of human operators to supervise the model-image registration process.

These methods require either (1) an initial pose estimate [39, 79], (2) a pre-segmented contour of the implant in the image [22, 75], or (3) a human operator to assist the optimization routine out of local minima [81]. Each of these requirements makes model-image registration methods impractical for clinical use. Even state-of-the-art model-image registration techniques [39] require human initialization or segmentation to perform adequately.

Machine learning algorithms automate the process of analytical model building, utilizing specific algorithms to fit a series of inputs to their respective outputs. Neural networks are a subset of machine learning algorithms that utilize artificial neurons inspired by the human brain's connections [82]. These networks have shown a great deal of success in many computer vision tasks, such as segmentation [29, 103, 123], pose estimation [64, 127], and classification [71, 97, 98]. These capabilities might remove the need for human supervision from TKA model-image registration. Therefore, we propose a three-stage data analysis pipeline (Fig. 3-1) where a convolutional neural network (CNN) is used to segment, or identify, the pixels belonging to either a femoral or tibial component. Then, an initial pose estimate is generated comparing the segmented implant contour to a pre-computed shape library. Lastly, the initial pose estimate serves as the starting point for a Lipschitzian optimizer that aligns the contours of a 3D implant model to the contour of the CNN-segmented image.

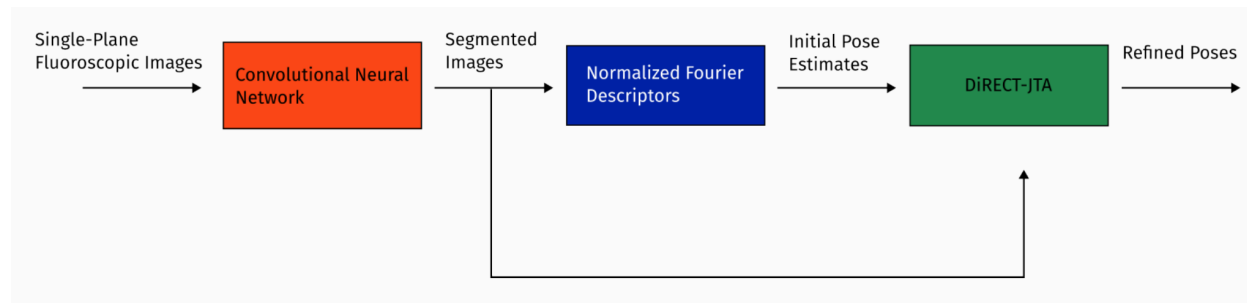


Figure 3-1. An overview of the pipeline for autonomous measurements of total knee arthroplasty kinematics. First, the data is processed through a convolutional neural network to locate the pixels belonging to the femoral and tibial implants [123], then, Normalized Fourier Descriptor shape libraries are used to determine and initial pose estimate [8], and lastly, DIRECT-JTA [39] is run on those segmented images using the NFD estimates as initializations for pose.

This paper seeks to answer the following three questions: (1) How well does a convolutional neural network segment the femoral and tibial implants from fluoroscopic and flat-panel images? (2) Can a Fourier descriptor-based pose estimation method produce useful initial guesses of 3D implant pose from the CNN-segmented images? (3) Can the Lipschitzian optimizer, given reasonable initial guesses, replicate human-supervised TKA kinematic measurements?

3.1 Methods

Data from seven previously reported TKA kinematics studies were used for this study [57, 63, 91, 92, 108, 124, 125]. These studies utilized single-plane fluoroscopy or flat-panel imaging to measure tibiofemoral implant kinematics during lunge, squat, kneel, and stair climbing movements from 8248 images in 71 patients with implants from 7 manufacturers, including 36 distinct implants. From each of these studies, the following information was collected: (1) deidentified radiographic images, (2) x-ray calibration files, (3) manufacturer-supplied tibial and femoral implant surface geometry files (STL format), and (4) human supervised kinematics for the tibial and femoral components in each of the images. CNNs were trained with images from six of the studies using a transfer-learning paradigm with an open-source network [123]. CNN performance was tested using two image collections: a standard test set including images from the six studies used for training and a wholly naïve test set using images from the seventh study, where the imaging equipment and implants were different from anything used in training (Fig. 3-2). We used both test image sets to compare human-supervised kinematics with autonomously measured kinematics. Separately, two independent groups utilized our software to assess the accuracy of TKA kinematics measurements compared to their previously reported reference standard systems using RSA [118] or motion capture [34].

3.1.1 Image Segmentation

Images were resized and padded to 1024x1024 pixels. Images containing bilateral implants had the contralateral knee cropped from the image. Segmentation labels were created by taking the human-supervised kinematics for each implant and generating a flat-shaded ground-truth projection image (Fig. 3-3). Two neural networks [123] were trained to segment the tibial and

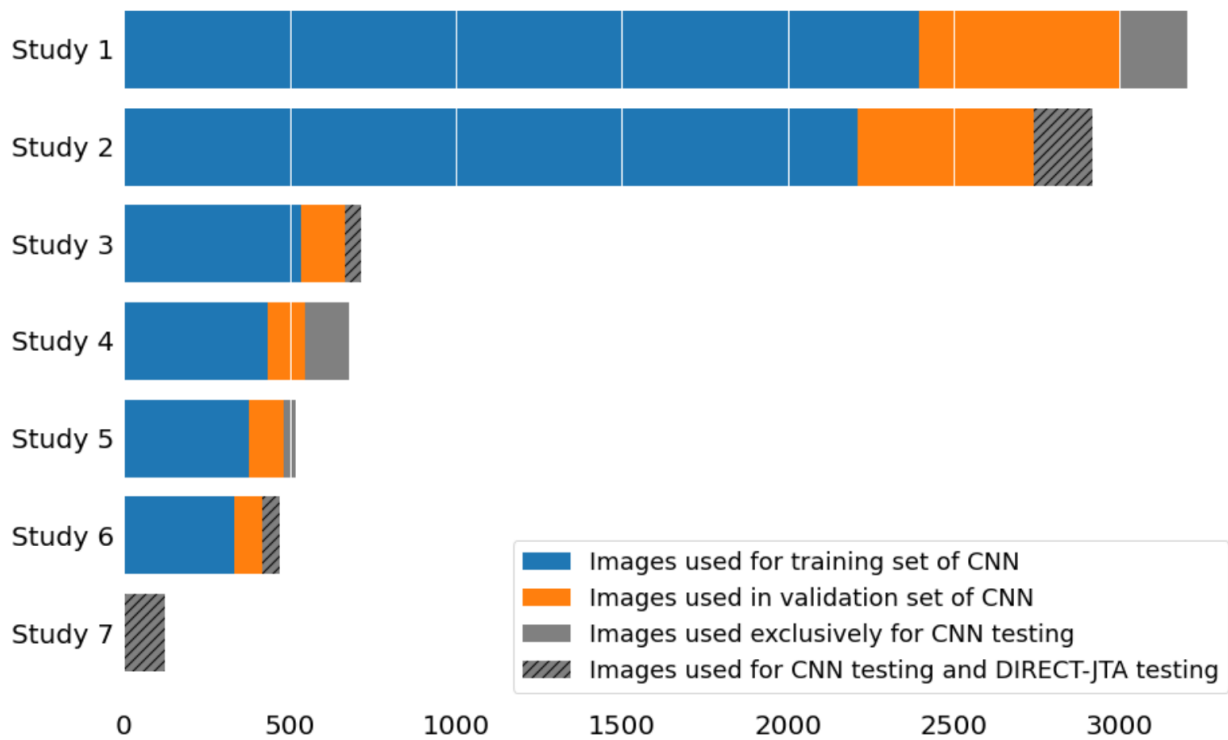


Figure 3-2. Data from seven studies were used to train and test the TKA kinematics measurement pipeline. Color coding in the figure identifies how many images were used for the training, validation, and testing functions. Images from the seventh study were used exclusively for testing the measurement pipeline that was trained using images from the other six studies.

femoral implants, respectively, from the x-ray images. Each network was trained using a random 6284/1572 (80/20) training/validation split. Augmentations were introduced in the training pipeline to improve the network's generalization to new implants and implant types [25]. Each neural network was trained on an NVIDIA A100 GPU for 30 epochs. The performance of the segmentation networks was measured using the Jaccard Index [55]. This calculates the intersection between the estimated and ground-truth pixels over the union of both sets of pixels. The ideal Jaccard index is 1.

3.1.2 Initial Pose Estimates

Initial pose estimates were generated from bounding contours of the CNN-segmented implant regions using Normalized Fourier Descriptor (NFD) shape libraries [8, 121, 122]. Shape libraries were created by projecting 3D implant models using the corresponding x-ray calibration

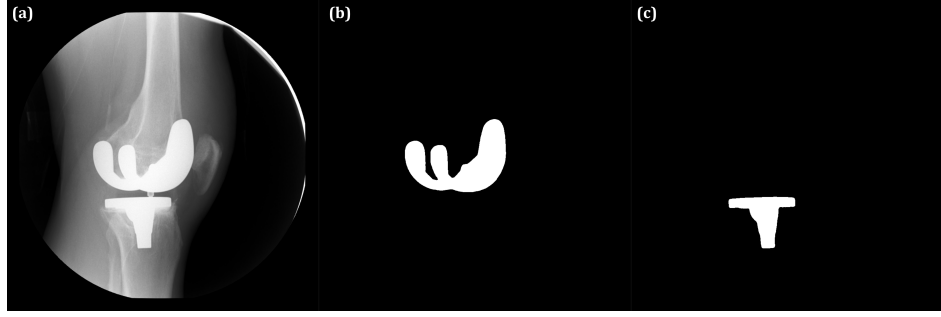


Figure 3-3. A representative fluoroscopic image is shown (a) with corresponding femoral (b) and tibial (c) ground-truth images created by flat-shaded projections of registered implant models.

parameters with $\pm 30^\circ$ ranges for the out-of-plane rotations at 3° increments (Fig. 3-4). Pose estimates were determined as previously described [8] NFD-derived femoral and tibial implant poses were transformed to anatomic joint angles and translations [47] and compared to the human-supervised kinematics for the same images using RMS differences for each joint pose parameter. The performance of this method was also assessed using flat-shaded projection images with perfect segmentation as a ground-truth reference standard.

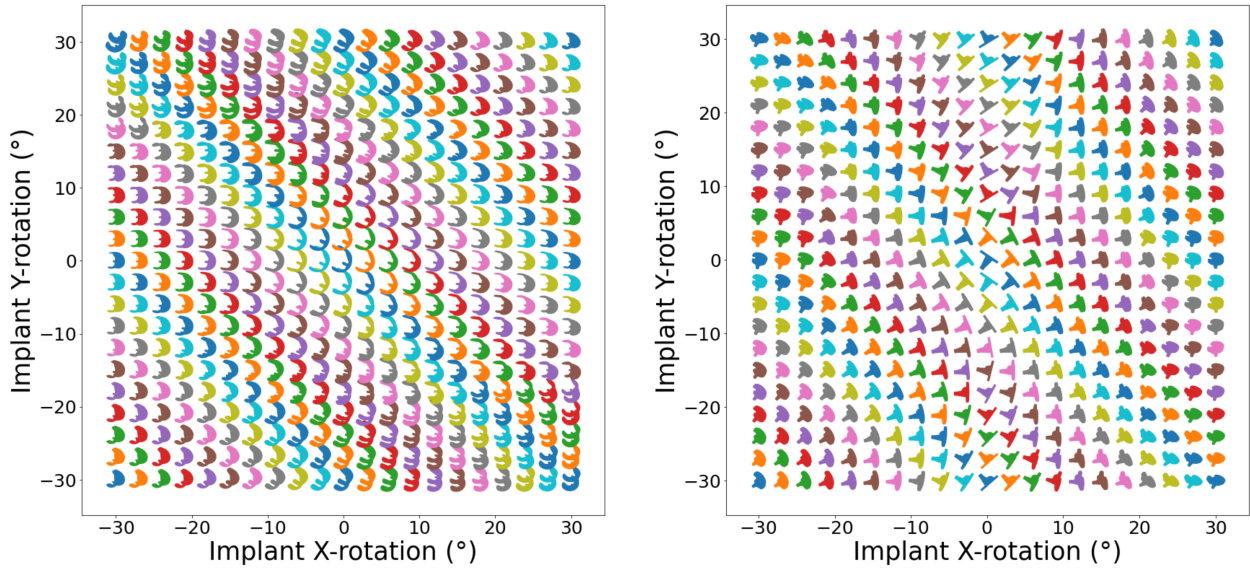


Figure 3-4. Femoral (left) and tibial (right) NFD shape libraries were generated to capture the variation in projection silhouette geometry with out-of-plane rotation [8]. Initial pose estimates were generated by comparing the NFD contour from the x-ray image to the shape library.

3.1.3 Pose Refinement

A modified Dividing Rectangles (DIRECT) algorithm called DIRECT-JTA [39] generated the final pose estimates. This method of Lipschitzian optimization divides the search into three stages, the “trunk,” “branch,” and “leaf.” Each of the three stages was assigned distinct cost function parameters and search regions. The cost function used a computationally efficient L1-norm between the dilated contour from the segmentation label and the projected implant. Successively decreasing the dilation coefficient allowed the optimization routine to escape local minima, and the leaf branch served to find the optimal out-of-plane translation. Transversely symmetric tibial implants posed problems during registration because two distinct poses produced roughly identical projections [65]. Because of this pose ambiguity, the tibial implant was always optimized after the non-symmetric femoral implant. In addition to the dilation metric, the tibial mediolateral translation and varus/valgus rotations relative to the femur were penalized. Final implant poses were transformed into knee joint rotations and translations [47] and compared to the human-supervised kinematics for the same images using RMS differences for each joint pose parameter. Squared differences between data sets were compared using one-way MANOVA with post-hoc multiple pair-wise comparisons using the Games-Howell test (R v4.2.0 using R Studio, rstatix, and stats).

3.1.4 Pose Ambiguities and Registration Blunders

A blunder was defined as an image frame with the squared sum of rotation differences greater than 5° between autonomous and human-supervised measures. These blunder frames contain errors considerably larger than would be clinically acceptable and warrant further exploration. Blunders were analyzed with respect to the tibial implant’s apparent varus/valgus rotation relative to the viewing ray (Fig. 3-5). A probability density function and cumulative density function were calculated for the blunder likelihood. Due to the high likelihood of blunders in this region, an ambiguous zone was defined for all apparent tibial varus/valgus-rotation less than 3.6 degrees, which is the mean + 1std of the blunder distribution (Fig. 3-5). Squared measurement differences between images inside and outside the ambiguous

zone were also compared using one-way MANOVA with post-hoc multiple pair-wise comparisons using the Games-Howell test.

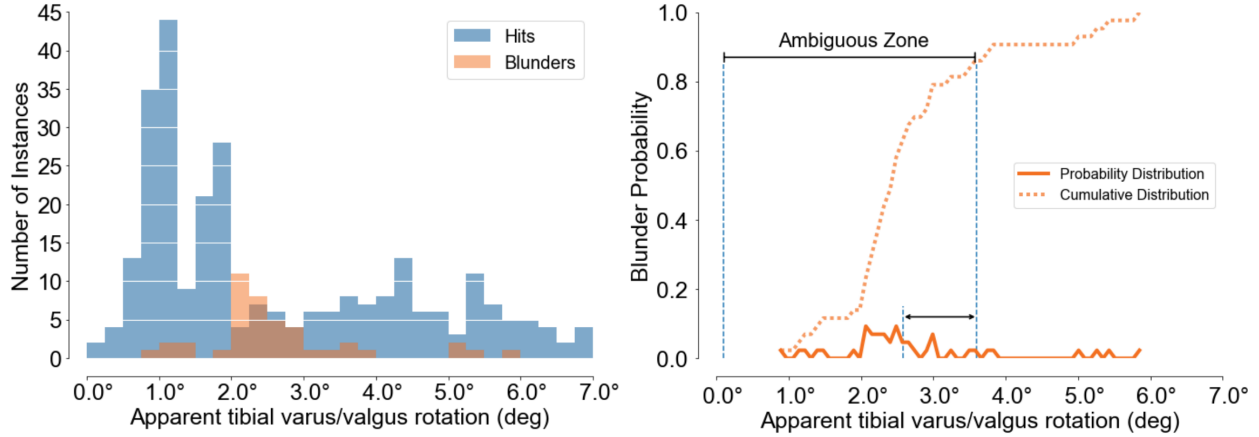


Figure 3-5. The histogram (left) shows the correctly registered frames (Hits, blue) and incorrectly registered frames (Blunders, orange) plotted as a function of the apparent tibial varus/valgus angle relative to the viewing raw. The probability plot (right) shows the distribution of blunders (solid orange) and the cumulative probability of blunders (dotted orange). The Ambiguous Zone is defined as apparent tibial varus/valgus rotations less than the mean + one standard deviation of the blunder probability distribution, capturing approximately 85 % of the blunders.

3.2 Results

CNN segmentation of standard test set images produced Jaccard indices of 0.936 for the femoral and 0.883 for the tibial components. CNN segmentation performance on the completely naïve test set was lower, 0.715 and 0.753, respectively.

The initial pose estimates were within the range of convergence for the DIRECT-JTA optimizer and offered a robust initialization for optimization (Table 3-1). The RMS differences for initial pose estimates on ground-truth images were smaller (better) than for CNN-segmented images, but the differences were mostly within a few millimeters or degrees. Due to poor sensitivity for measuring out-of-plane translation with monocular vision, the mediolateral translation had the largest RMS differences for both image types.

Table 3-1. RMS differences between NFD initial estimates and human supervised kinematics

Implant	Images	$x_{trans}(mm)$	$y_{trans}(mm)$	$z_{trans}(mm)$	$z_{rot}(\circ)$	$x_{rot}(\circ)$	$y_{rot}(\circ)$
Femoral	CNN	2.37	0.71	17.59	2.54	2.45	4.75
Femoral	Ground-Truth	2.06	0.57	13.53	0.85	1.42	4.00
Tibial	CNN	2.06	1.49	29.93	0.94	5.59	9.47
Tibial	Ground-Truth	2.05	0.87	14.60	0.55	4.73	6.23

RMS differences between DIRECT-JTA optimized kinematics and human-supervised kinematics were sub-millimeters for all in-plane translations (Table 3-2). Mediolateral translations and out-of-plane rotation differences were smaller when the pose of the tibia was outside the ambiguous zone. The RMS differences for the completely naïve test set were within 0.5 mm or 0.5 deg compared to the standard test set, indicating similar performance on the entirely novel dataset.

Table 3-2. RMS differences between DIRECT-JTA optimized and human supervised kinematics

Test Set	Image Group	Num. Images	A/P (mm)	S/I (mm)	M/L (mm)	Flx/Ext (°)	I/E (°)	V/V (°)
Standard	Inside AZ	187	0.69	0.52 ^b	1.75 ^a	0.73 ^a	3.38	1.94 ^a
Standard	Outside AZ	83	0.69	0.47 ^c	0.917	1.03	1.81	0.61
Naive	Inside AZ	47	0.80	0.74	1.72	1.39	4.04	2.48 ^d
Naive	Outside AZ	75	0.69	0.64	0.69	1.031	1.15	0.85

^a Pairwise difference ($p < 0.05$) for Standard Inside AZ vs Standard Outside AZ

^b Pairwise difference ($p < 0.05$) for Standard Inside AZ vs Naive Inside AZ

^c Pairwise difference ($p < 0.05$) for Standard Outside AZ vs Naive Outside AZ

^d Pairwise difference ($p < 0.05$) for Naive Inside AZ vs Naive Outside AZ

AZ = Ambiguous Zone

There was one femoral blunder and 43 tibial blunders out of 392 test images. Using the definition of the ambiguous zone as apparent tibial varus/valgus rotation less than 3.6 deg, 11% of images have a tibial blunder within this zone, compared to 3.2% outside. Sixty-six percent of tibial blunders were due to symmetry ambiguities (Fig 3-6).

One-hundred thirteen image pairs from an RSA study of TKA were used to independently assess the accuracy of the autonomous kinematics measurement for single-plane lateral TKA images. RMS errors were 0.8mm for AP translation, 0.5mm for SI translation, 2.6mm for ML translation, 1.0° for flexion/extension, 1.2° for abduction/adduction, and 1.7° for internal/external rotation. At a different institution, 45 single-plane radiographic images were acquired with an instrumented sawbones phantom that was independently tracked using motion capture. Comparing the motion capture and autonomously measured radiographic kinematics, the RMS

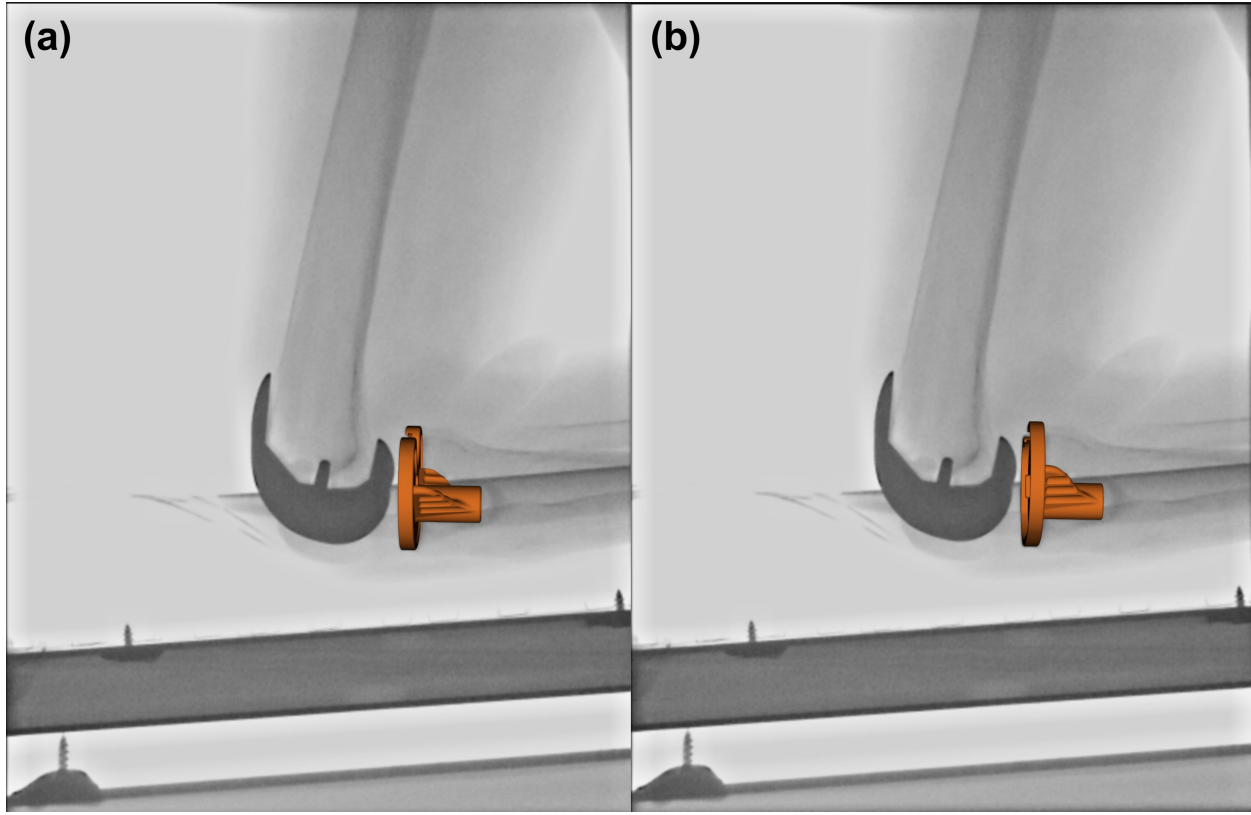


Figure 3-6. The figure shows the same radiographic image with two registered tibial implant poses: (a) shows a correctly registered tibial implant, while (b) shows an implant caught in a local cost function minimum corresponding to a nearly symmetric pose.

errors were 0.72mm for AP translation, 0.31mm for SI translation, 1.82mm for ML translation, 0.56° for flexion-extension, 0.63° for abduction-adduction, and 0.84° for internal-external rotation.

3.3 Discussion

Dynamic radiographic measurement of 3D TKA kinematics has provided important information for implant design and surgical technique for over 30 years. Many surgeons have expressed an interest in utilizing this type of measurement in their clinical practices; however, current methods are impractical. We developed a completely autonomous TKA kinematics measurement pipeline that can potentially provide a practical method for clinical implementation. This study sought to answer three questions, (1) How well does a neural network segment TKA implants from fluoroscopic and flat-panel images? (2) How well can an NFD shape library estimate the pose of a TKA implant given a CNN-segmented image? And (3) How well does a

Lipschitzian optimization routine replicate human-supervised kinematics for TKA implants given an approximate initial guess?

CNN image segmentation of TKA implants worked well, with Jaccard indices greater than 0.88 for the standard test set, and greater than 0.71 for the naïve test set. Segmentation performance for the standard test set outperformed published examples by 0.05-0.1 Jaccard points [102, 135], with the naïve test set on par with other segmentation examples. The most notable decrease in segmentation performance occurred along the perimeter of the segmented pixel region, especially in areas where implant projections occluded each other. These imperfectly segmented perimeter regions likely affect the initial pose estimate and the DIRECT-JTA optimization solution since both methods rely heavily on the segmented implant boundary. Further improvements can be made for the perimeter segmentation results by introducing intelligent augmentations during training using generative models [49] and performing neural network bolstered contour improvement strategies [133].

Our initial pose estimates were satisfactory as an initialization for the DIRECT-JTA optimization, falling within the convergence region of $\pm 30^\circ$ [39]. However, the performance for the ground-truth projections was not as good as the cited method [8], which achieved errors of less than 1mm for in-plane translation and 2° for rotation. The cited method utilized an additional refinement step for the NFD estimation, interpolating the apparent out-of-plane angles between nearest shapes in the library. This extra step was not done because only approximate initial pose estimates were needed. In addition, the current study incorporated a vastly larger set of implant shapes (36 vs. 2) and image quality and calibration variations. Distinct implant shapes manifest unique normalization maps, where there can be discontinuities or jumps in normalization angles which affect the best-fitting library entry (Fig. 3-4) [121, 122]. These details are easily upgraded with additional code using previously reported methods but were not pursued because the initial pose results were well within the DIRECT-JTA convergence region. The initial pose estimates for the CNN-segmented images were not as good as for the ground-truth projections. This follows directly from the fact that the perimeter of the segmented implants was not as accurately rendered,

leading to poorer results with the edge-based NFD method. Finally, the out-of-plane translation estimates were relatively poor for both ground-truth projects and CNN-segmented images. This translation estimate is extremely sensitive to model projection and edge detection details and can be adjusted for better results if required.

RMS differences between human-supervised and DIRECT-JTA optimized kinematics demonstrate the two methods provide similar results. In-plane translation differences of less than 0.8mm and out-of-plane less than 1.8 mm, indicate good consistency in determining the relative locations of TKA implants. Rotation differences of 4° or less for frames within the ambiguous zone, and less than 1.7° for frames outside the ambiguous zone, indicate joint rotation measures with sufficient resolution to be clinically useful. We observed two important characteristics in the measurement comparisons that will affect future implementations and use. First, we identified an ambiguous zone of apparent tibial rotations wherein there is a higher incidence of registration errors. These errors resulted in significant differences in measurement performance for the out-of-plane translations and rotations. This phenomenon, resulting from the nearly symmetric nature of most tibial implants [8, 39, 75, 81, 137] prompts either practical modification to imaging protocols to bias the tibial view outside the ambiguous zone or modifications of the model-image registration code to enforce smooth kinematic continuity across image frames and/or to impose joint penetration/separation penalties [86]. Second, we observed similar measurement performance for the standard and naïve test sets, which differed only in the superior/inferior joint translation. This suggests that the autonomous kinematic processing pipeline can provide reliable measures for implants and imaging systems that were not part of the training set, which will be important for application in novel clinical environments.

Two independent research teams utilized our software to evaluate the accuracy of our autonomous measurement pipeline compared to their reference standard methods using implants and image detectors that were not part of our training sets. In both cases, the accuracy results were comparable to results reported for contemporary human-supervised single-plane model-image registration methods for TKA kinematics [8, 13, 14, 39, 70]. Interestingly, the

independent accuracy results appeared superior to our assessment of differences between autonomous and human-supervised measures of TKA kinematics. In both cases, the independent centers used high-resolution flat-panel detectors that provided better spatial resolution and grayscale contrast than most of the imaging systems included in our datasets. With images of similar quality, it is reasonable to expect similar measurement accuracy.

This work has several limitations. First, the image data sets resulted from previous studies in our labs, so there was no prospective design of which implant systems and image detectors should be included for a pipeline that generalizes well to other implants and detectors. Nevertheless, the naïve data set and the independent assessments, all involving implants and detectors not used for training, performed well and suggest that the method can usefully generalize to measurements of traditionally configured TKA implants. Future work is required to evaluate measurement performance with partial knee arthroplasty or revision implants. Second, many methodologic and configuration options and alternatives remain to be explored, and the current pipeline implementation should not be considered optimal. How best to disambiguate tibial poses and determine the most effective and robust optimization cost functions are areas of current effort.

We present an autonomous pipeline for measuring 3D TKA kinematics from single-plane radiographic images. Measurement reproducibility and accuracy are comparable to contemporary human-supervised methods. We believe capabilities like this will soon make it practical to perform dynamic TKA kinematic analysis in a clinical workflow, where these measures can help surgeons objectively determine the best course of treatment for their patients.

CHAPTER 4

CORRECTING SYMMETRIC IMPLANT AMBIGUITY IN MEASURING TOTAL KNEE ARTHROPLASTY KINEMATICS FROM SINGLE-PLANE FLUOROSCOPY

Measuring total knee arthroplasty (TKA) kinematics from fluoroscopic images has been an important contributor to knee implant design, post-operative assessment, and predictive modeling for wear and failure patterns for nearly 30 years [11, 13, 41]. However, the application of this technology has been limited to research use by the challenges of performing these measurements quickly and reliably, as they often require expensive equipment and time-consuming processes [8, 74, 81, 137]. Recent advancements in computer vision and machine learning have opened up the possibility of using a single fluoro-camera for fully autonomous TKA kinematic measurement [21, 58], making it more accessible and cost-effective for hospitals and clinics. Nonetheless, this approach faces inherent limitations in accurately resolving orientation and location information using only one fluoro-camera view [8, 39, 81, 128, 137].

One of the key issues researchers encounter when dealing with imaging from a single camera arises from symmetric implant geometries. Under a weak perspective/nearly orthographic projection paradigm [116], symmetric implants have distinct 3D orientations that produce nearly indistinguishable 2-dimensional projective geometry. (Fig. 4-1). Due to the model-image registration process relying on the information present in the 2D fluoroscopic image, this causes multiple local minima for many optimization algorithms. Human-supervised kinematics measurements for TKA with symmetric tibial implants frequently rely on the relative location of the fibula in the fluoroscopic image to disambiguate difficult poses. Unfortunately, fully autonomous solutions can't utilize this reference point, causing difficulty in algorithmic implementation.

In this paper, we utilize 12,592 images from seven studies that utilized human-supervised TKA kinematics [57, 63, 91, 92, 108, 124, 125] to explore the potential of a novel method to classify and correct “symmetry trap” poses in single-plane TKA kinematic measurements. The goal is to improve the accuracy and resolution of single-plane TKA measurements and enable more accessible and reliable kinematic data for orthopaedic applications.

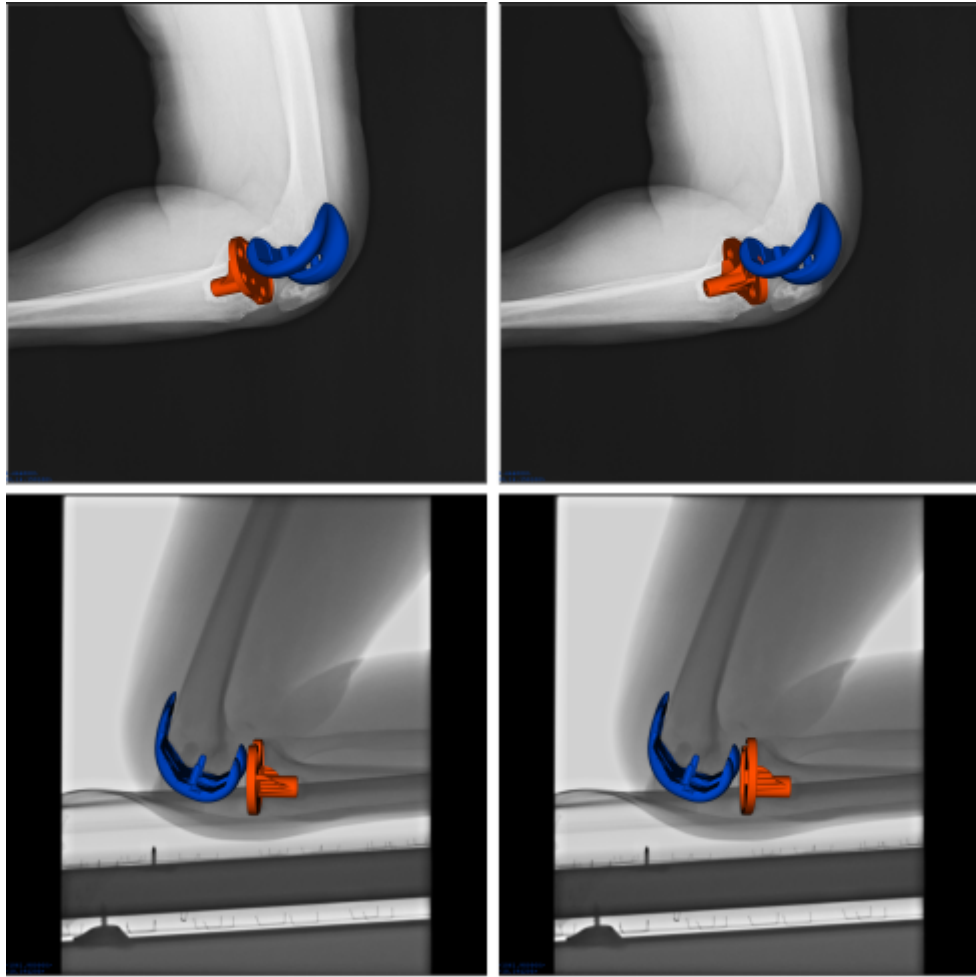


Figure 4-1. Two examples of symmetry pose dyads with the correct (left) and symmetry trap (right) kinematics. For some orientations, the symmetry trap is obviously incorrect (top), and for others, it is more ambiguous (bottom).

This research paper will answer two key questions: (1) How effectively can machine learning methods distinguish between “true” and ‘symmetry trap’ poses in cases involving symmetric implants? (2) How well can we systematically correct “symmetry traps” arising in kinematics sequences obtained from fluoroscopic images?

4.1 Methods

4.1.1 Study Design and Sample

In this paper, we are addressing the issue of “symmetry traps” in TKA kinematics measurements from single-plane fluoroscopy. To do so, we take a data-driven approach. We start with a collection of human-supervised “true” kinematic measurements, then determine the

respective “symmetry trap” orientation using a novel algorithm. Using this collection of both “true” and “symmetric” poses, we train eight different machine learning classifiers and evaluate their performance on both an internal and external test set. However, for more ambiguous poses, it is typically the case that both the “symmetry trap” and “true” pose appear “true”. To account for these, we then take the highest performing classifier and use it to establish an algorithm that takes as input a contiguous sequence of kinematics measurements, and imposes continuity constraints to fix “symmetry traps” in real-world data. We report the performance of our cubic spline correction algorithm on a dataset of autonomously measured kinematics [58]. All programs were written in Python 3.10.

The dataset used for development of the methodology comprises seven total studies [57, 63, 91, 92, 108, 124, 125] comprising 12,592 images of radiographic data. We completely withheld data from one study [91] during training to use later as an external test set.

4.1.2 Determining Symmetric Orientations

First, “symmetry trap” poses were identified from “true” poses through a novel algorithm devised to “flip” any given pose into its symmetric counterpart (Fig. 4-2). The algorithm proceeds as follows:

1. Determine the viewing ray from the object origin to the camera origin. Denote this as \vec{v} , where $||\vec{v}|| = 1$.
2. Determine the symmetric axis of the object, \vec{s} , where $||\vec{s}|| = 1$. This symmetric axis is equivalent to the normal vector of the “mirror plane” of symmetry for the object.
3. Determine the axis and angle of rotation between \vec{s} and \vec{v} and construct the equivalent rotation matrix.
 - (a) The axis is the cross product, $\vec{m} = \vec{v} \times \vec{s}$.
 - (b) The angle is the normalized dot product, $\psi = 2 \times \cos^{-1} \frac{\vec{v} \cdot \vec{s}}{||\vec{v}|| ||\vec{s}||}$
4. Apply body-centered rotation to the symmetric object about \vec{m} by ψ .

For each projective geometry, there exist exactly two poses (i.e., a dyad) that produce it, thus applying this algorithm twice will return the original pose.

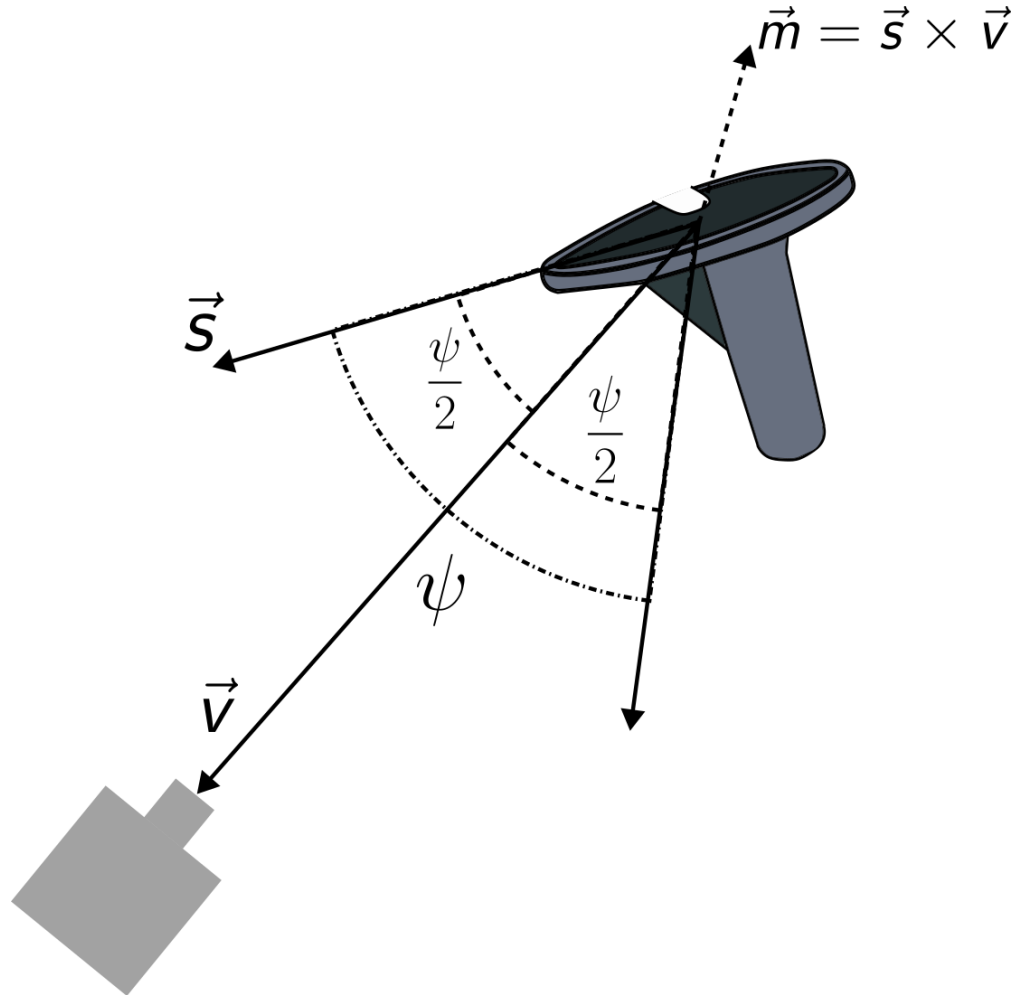


Figure 4-2. A visualization of the “symmetry flipper” algorithm that converts 3D orientations into their symmetric counterpart.

4.1.3 Constructing Dataset

We collected data from seven studies utilizing human supervised total knee arthroplasty kinematics, totaling approximately 12,592 individual images. Anatomic tibiofemoral kinematics were stored as “true” poses. The proposed algorithm was then applied to each image’s tibial implant, generating corresponding “symmetric” poses, for a total of 25,184 samples (Fig. 4-3). Solid angle distances (ψ) obtained from the symmetry flipper algorithm were also stored, and the dataset was stratified based on the solid-angle value and split into 67% training and 33% testing

sets for unbiased evaluation. Data from one study [91] was completely withheld from training to be used as an external test set.

Thus, for each sample, the input was $\{\theta_{Int/Ext}, \theta_{Flx/Ext}, \theta_{Var/Val}, \psi\}$ with $\theta_{Int/Ext}, \theta_{Flx/Ext}, \theta_{Var/Val}$ representing anatomic internal/external rotation, flexion/extension, and varus/valgus respectively. The target was either ‘true’ or ‘symmetry trap’.

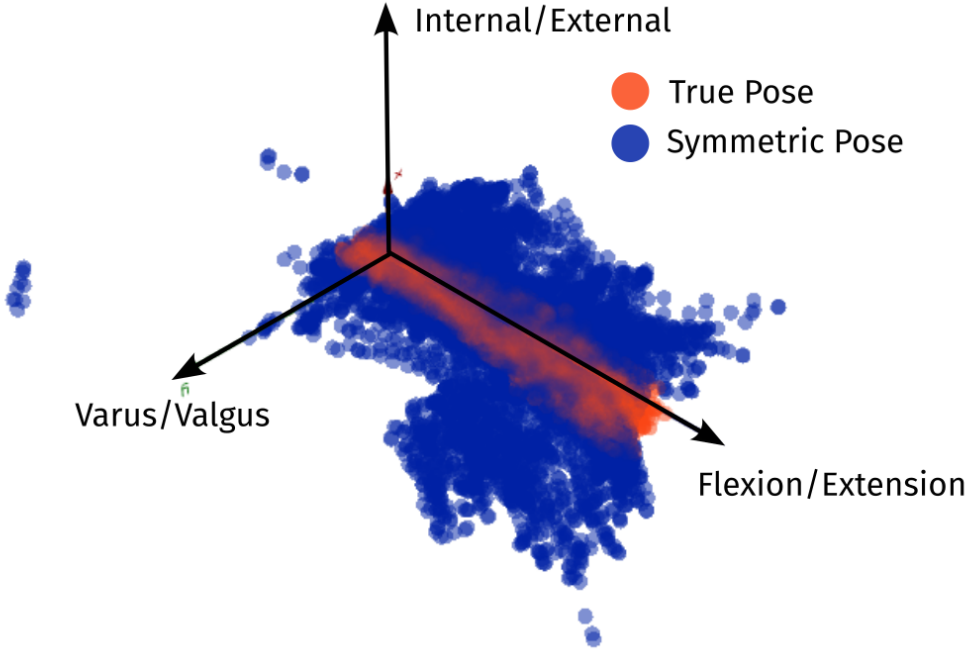


Figure 4-3. A 3D scatter plot of our training data with ‘true’ poses in orange and ‘symmetry trap’ poses in blue. Of note, there are distinct regions of exclusively ‘symmetry trap’ poses, while the region of predominately ‘true’ poses (orange cylinder along Flexion/Extension axis) also has many ‘symmetry trap’ poses.

4.1.4 Classification Algorithms

In this study, we implemented a selection of classification algorithms that use a range of different learning strategies (Table 1) from Scikit-learn [94] to classify any individual input pose as “true” or “symmetry trap”. The chosen algorithms were K-Nearest-Neighbors (KNN) [38], Support Vector Machines (SVM) [32], AdaBoost [42], Histogram Gradient Boosting [43], Bagging Meta-Estimator [20], Stacked Generalization [112, 126], and (majority) Voting Classifier. The hyperparameters for each method were tuned using stratified 5-fold cross validation using grid-search to test all possible combinations. Stacked generalization and the

voting classifier used the tuned hyperparameters from each of the other estimators in their predictions. We recorded sensitivity [131], specificity [131], accuracy [54], and the F1 score [117] for each algorithm on both our internal and external test sets. For the highest performing individual classifier on the internal test set, we also evaluated these metrics on stratified partitions of the internal test set to determine relative performance for different ψ values.

4.1.5 Fixing Incorrect Symmetry Trap Poses

The primary objective of this study is to accurately measure the kinematics of all images in a TKA kinematics sequence and to robustly fix incorrect symmetry trap poses. However, due to the inability to know a-priori which poses are “true” or in a “symmetry trap”, we must employ a separate procedure for systematically correcting individual images. Thus, for every kinematics sequence we employ the following procedure:

1. Determining Ambiguous and Non-ambiguous Poses for each image
 - (a) For each image, we generate the ‘symmetric’ pose corresponding to the input pose.
 - (b) We run both the input and its symmetric pose through the highest performing classification algorithm.
 - (c) If the input pose and its symmetric pose are differently labeled by the classifier (i.e., one is labeled “true”, and the other “symmetry trap”), take the pose labeled “true” as the actual pose.
 - (d) If both poses return the same label (i.e., both “true” or both “symmetry trap”), label the pose as “ambiguous” and move to step 2.
 - (e) If no poses were labeled “ambiguous”, the procedure is finished.
2. Construction of 3-Dimensional cubic b-spline of the movement
 - (a) A spline is individually fit through the flexion/extension, internal/external rotation, and adduction/abduction angles for all images that were **not** labeled ambiguous.
3. Correcting Ambiguous Poses

- (a) We sample the cubic spline at image locations of ambiguous poses.
- (b) We compare the solid-angle difference between the input and symmetric pose to the pose at the sampled spline location.
- (c) Whichever pose is closer to the spline, we take this as the ‘true’ pose.

To evaluate this procedure, we used a dataset of kinematics generated from a fully autonomous method [58] to emulate the real-world use case of this algorithm as a post-processing operation. This test set has robustly quantified the presence of “symmetry traps”, and so allows us to report sensitivity, specificity, accuracy, and the F1 measure of its ability to correct symmetry traps in a clinical setting.

4.2 Results

4.2.1 Machine Learning Classification Performance

Classification accuracy on the internal test set ranged from 87.8% to 94.0%, sensitivity ranged from 92.9% to 94.7%, and specificity ranged from 83.5% to 93.6% for all eight methods evaluated (Table 4-1). Stacked generalization and the voting classifier tended to outperform the other classifiers, as they both incorporated a combination of the other models in their decision-making. For the external test set, accuracy ranged from 90.9% to 94.2%, sensitivity from 93.6% to 97%, and specificity from 88.4% to 91.9% (Table 1). The SVM with Radial Basis Function kernel had the highest accuracy and F1 score, at 94% and 0.94 respectively. Stacked generalization performed slightly worse in the external test set. Overall, the performance in the external test set was comparable to the performance on the internal test set, with some classifiers seeing decreased performance (K-Nearest-Neighbors, Stacked Generalization), and others seeing slightly increased performance (Support Vector Machines, AdaBoost, Voting Classifier).

Table 4-1. Machine Learning Classifier Performance

Classifier	Hyperparameters	Test Set	Accuracy (%)	Sensitivity (%)	Specificity (%)	F1-Score
Support Vector Machine (RBF)	$C = 1000$	Internal	92.08	94.75	89.73	0.92
		External	94.21	97.12	91.64	0.94
Support Vector Machine (Poly)	$C = 1000$ Poly Degree = 2	Internal	87.65	92.54	83.8	0.87
		External	92.08	96.58	88.38	0.92
K-Nearest-Neighbors	$N = 4$ Minkowski Dist.	Internal	93.12	93.96	92.32	0.93
		External	90.93	93.62	88.55	0.91
AdaBoost	$N = 200$	Internal	88.78	91.08	86.74	0.88
		External	92.86	97.23	89.22	0.93
Histogram Gradient Boosting	$L.R. = 0.1$	Internal	93.11	94.98	91.4	0.93
		External	93.24	96.67	90.29	0.93
Bagging Estimator	$N = 500$	Internal	93.32	94.28	92.41	0.93
		External	93.82	95.95	91.88	0.94
Stacked Generalization	N/A	Internal	94.3	94.78	93.84	0.94
		External	92.86	94.94	90.96	0.93
Majority Voting Classifier	N/A	Internal	92.63	95.85	89.86	0.92
		External	93.34	96.87	90.31	0.93

Table 4-2. Stratified- ψ test set stacked generalization classification performance

Psi Range	Sample Size	Accuracy (%)	Sensitivity (%)	Specificity (%)	F1-Score
0 – 5°	488	71.04	71.43	70.7	0.69
5 – 10°	1132	88.21	90.53	85.98	0.88
10 – 15°	1224	93.0	92.78	93.2	0.93
15 – 20°	1107	96.13	96.97	95.31	0.96
> 20°	3568	98.28	98.32	98.24	0.98

4.2.2 Stratified ψ Test Set Performance

As the value of ψ increases, the performance of stacked generalization classification increases (Table 4-2). At values closer to a pure-lateral view (0°), accuracy is roughly 71%, and once the implants exceed 5° off-lateral, accuracy increases to above 88%.

4.2.3 Symmetry Trap Correction Performance

When applying the procedure to correct symmetry traps, we achieve an accuracy of 91.1%, a sensitivity of 67.4% and a specificity of 94% on an external test set. The average “distance to symmetric pose” (ψ) was 16.6° for the images correctly classified, and 7.12° for the images incorrectly classified. For our initial internal test set, the distance to the symmetric pose was 25.6° for images correctly classified, and 9.65° for incorrectly classified images. Thus, the incorrect images are closer to a true lateral single-plane image, meaning the difference between the symmetric dyad of poses is smaller.

4.3 Discussion

Orthopaedic surgeons desire a practical method to clinically quantify TKA kinematics for post-operative assessment or exploration of unsatisfactory outcomes [10]. To date, manual methods for quantifying TKA kinematics from single-plane radiographic images have been too time-consuming for clinical use. However, the application of machine learning methods has significantly enhanced their convenience [58]. Modern autonomous kinematics measurement software, implemented on a modest laptop with a dedicated graphics card, demonstrates efficient processing capabilities, requiring approximately 5–15 seconds for analyzing a single image [58]. A critical step in making this technology ready for clinical use is to address the pose ambiguity issue that arises from single-camera views of symmetric tibial implant components in a time-efficient manner. We found that several machine learning algorithms were able to robustly identify and correct symmetric erroneous poses with greater than 90% accuracy, making these measurement methods sufficiently autonomous and robust to be considered for clinical use.

We demonstrated that classical machine learning techniques are extremely adept at handling the classification of “true” and “symmetry trap” TKA kinematics measurements from

single-plane fluoroscopy. As a first study in this domain, benchmark comparisons with other metrics, datasets, or algorithms are not available. As a first study in this domain, benchmark comparisons with other metrics, datasets, or algorithms are not available. However, an accuracy level of at least 87% establishes a useful performance benchmark in terms of clinical applications of these methods and for future research in this field. As expected, stacked generalization [112, 126], where “the worst possible performance is the highest of any individual estimator” held true for our internal test set, and outperformed all other algorithms. Interestingly, the same trend did not hold for our external test set, which contained kinematics from patients, imaging machines, and surgeons that were completely withheld from training. In our external test set, SVMs with radial basis function kernel seems to outperform the other classifiers.

Our symmetry trap correction procedure has strong performance in the accuracy ($> 91\%$) and specificity ($> 94\%$). We note decreased sensitivity related to decreasing values of our ψ term, consistent with intuition: when two possible poses are closer together, they are harder to disambiguate. When performance is measured based on ψ values greater than 5 or 10 degrees, we see that our symmetry trap correction algorithm boasts notably increased performance (Table 2). Previous work has also shown an increase in the prevalence of symmetry traps in low- ψ poses [58]. We also note that in real-world data, we have imbalanced class representation because most symmetry traps are caught in the initial kinematics measurement, leaving only the most difficult cases for this algorithm to correct. These reasons both culminate with an expected decreased sensitivity when trying to correct symmetry trap poses. Future work might be able to address this problem using time-series machine learning algorithms like recurrent neural networks [51] and transformers [120] to isolate specific images that have fallen into symmetry traps based on local and global relationships with other kinematics in that particular sequence. Additionally, 3D geometries could be used to impose penetration and separation penalties that are further used to refine ambiguous poses.

The performance of autonomous measurements of single-plane fluoroscopy kinematics measurements already achieve clinically acceptable levels of error. Despite this, measurement

errors still occur and roughly 67% of images that are incorrectly optimized fall into symmetry traps [21, 58]. With the techniques proposed in this work, we can drastically improve the overall performance of autonomous single-plane TKA kinematics measurements and remove the largest source of inaccuracy.

Stratifying measurement performance by (Table 2), it is clear that the joint viewing perspective is a dominant contributor to pose ambiguities. This suggests a modification to imaging protocols for measuring TKA kinematics is needed to minimize the number of images that fall into the “ambiguous zone”. Instead of “pure lateral” imaging that attempts to perfectly center the knee in the image frame, we suggest positioning the center of the knee 1–2 inches away from the center of projection, and to rotate the plane of the observed leg by 5 degrees from parallel with the image detector. These small adjustments to the imager/patient alignment would cause all kinematics to have $\psi > 5^\circ$, which improves classification accuracy by at least 20%. Similar imaging protocol improvements have been proposed for bi-plane RSA[89].

This study has some limitations. In this study, we use human-supervised kinematics from single-plane images, where there is always the possibility that the human operator fell into error when distinguishing between “true” and “symmetry trap” poses in a sequence of images. This can occur due to a myriad of factors, including low image quality and near-lateral imaging angles. To mitigate this, validated ground truth kinematics would be necessary to create a robust algorithm without any errors in the training data.

The correction algorithm recommended in this study assumes that the femoral implant has been properly registered with correct kinematics. While this is typically a good assumption because most femoral implants are asymmetric, and have an extremely low likelihood of falling into their own “symmetry traps” [58], improper registration of both a symmetric tibial implant and symmetric femoral implant would decrease the feasibility of the proposed procedure.

4.4 Concluding Remarks

This study presents a novel method of overcoming one of the most pernicious issues facing researchers measuring TKA kinematics from single-plane fluoroscopy. Our algorithm combines 3

elements (1) calculating “symmetry trap” poses from “true” poses, (2) classical machine learning algorithms to classify a single pose as “true” or “symmetry trap” and (3) a procedure that applies those machine learning outputs to a contiguous sequence of kinematics to construct a spline and correct symmetry traps in real-world data. Additionally, the “symmetric flipper” algorithm provides a strong foundational approach for any symmetric object in a weak-perspective paradigm and can drastically reduce the complexity of many optimization algorithms by reducing the search space. Because this algorithm is model-agnostic, it could be used in many applications where orientation ambiguities arise. Our results also suggest slight alterations to imaging angles, which could reduce errors due to ambiguous poses resulting from symmetrical tibial implants. We believe that this method, along with recent advancements in autonomous kinematics measurements, will soon make it practical to perform dynamic TKA kinematics measurements in a clinical setting without the inherent limitations of single-plane radiographic imaging.

CHAPTER 5

MUSINGS ON LATENT KINEMATICS SPACE AND SYNTHETIC BIOMECHANICS DATA

5.1 Introductory Remarks

In order to make autonomously measuring joint kinematics a clinically viable tool, the movements and motions being measured must be standardized. Similar efforts have been put into standardized post-operative outcome metrics like the Knee Society Score (KSS), Knee Injury and Osteoarthritis Outcome Score (KOOS), the Forgotten Joint Score, the Western Ontario and McMaster Universities Osteoarthritis Index (WOMAC), among others. Standardizing these metrics enables reliable and objective comparisons across different groups, implants, and surgical techniques. This same need for standardized metrics exists when quantifying joint kinematics for research and clinical purposes. Unfortunately, no such standardization exists for quantifying joint kinematics. While most groups perform similar activities of daily living (Some form of walking, stair rise, chair rise, kneel, lunge, and squat), variations in how these activities are executed hinder direct comparison accuracy.

So, this chapter describes a data-driven approach toward being able to select the highest yield activities to be included in a clinical kinematics examination. To render the autonomous measurement of joint kinematics a viable clinical tool, the time to collect the data must not be excessive, and so a brief and succinct set of activities is preferred. From these constraints, the first approach stems from the thought, “All kinematics data is coming from the same patient. Are there underlying characteristics from one activity that translate to all activities?” An example might arise: “Can we predict the patient’s stair rise kinematics from their walking kinematics?” The motivating intuition behind these ideas is that they all come from the same patient, and are being driven by the same underlying musculature. The following chapter will detail the beginning of an experimental procedure, and why the data was insufficient for answering the above questions. However, another question arises: “Given the statistical parameters surrounding a “good outcome” or “bad outcome”, might we be able to generate synthetic patient data to overcome the lack of real-world kinematics data?” This question is particularly relevant in the context of ‘big data’ and its growing impact. Many modern algorithms leverage an enormous amount of data,

often more than traditional methods of quantified biomechanics are able to generate. Additionally, HIPAA requirements make it incredibly difficult to share data, slowing down the rapid progress in curated algorithms for biomechanics data that we see with open datasets like ImageNet [105].

And so, the following chapter will contain some background information toward solving these problems.

5.2 Latent Kinematics Space and Reducing the Number of Movements Required for a Full Kinematics Evaluation

In the field of Natural Language Processing (NLP), the concept of a ‘latent space’ is used to represent the underlying structure and meaning of language, beyond what is explicitly observable in the text [61]. For instance, in NLP, words are transformed into vectors in a high-dimensional space, where the distances and directions between these vectors capture the subtle relationships and contextual nuances of language. This transformation enables algorithms to ‘understand’ and process language in a way that mirrors human comprehension.

Drawing a parallel to kinematics, we can view each movement pattern as a ‘sentence’ composed of ‘words’ that are the discrete kinematic data points (such as angles, velocities, and accelerations). Just as sentences in language express complex ideas constructed from simpler words, movement patterns in kinematics are complex expressions composed of simpler biomechanical elements. These elements interact in a high-dimensional ‘kinematic space,’ analogous to the latent space in NLP. The goal of our kinematics translator, then, is akin to a language translator in NLP. It seeks to understand the ‘grammar’ of movement in this latent space, allowing us to translate one set of movements (like walking) into another (like stair climbing), based on their underlying biomechanical structure. This could enable clinicians to infer a wide range of kinematic patterns from a limited set of observed movements, much like how a skilled linguist might infer meaning from a limited set of words or sentences.

5.2.1 Brief Mathematical Preliminary and Notation

Let \mathfrak{X}_{mvt} be the ambient kinematics space from which a particular sample is measured, where $mvt \in \{\text{stair, walk, lunge, } \dots\}$. Essentially, this is the space of all possible kinematics patterns for a particular movement. For simplicity, we can assume that this space \mathfrak{X}_{mvt} follows

some distribution, μ_{mvt} . The “latent space” of our kinematics is \mathfrak{Z} and follows some fixed distribution, ξ . For a universal translator, wherein the expressiveness of outputs resembles the underlying musculoskeletal system of that particular patient, you would not have a latent space for each movement, (\mathfrak{Z}_{mvt}), but rather, the single latent space would (hopefully) encode all relevant information about the patient.

Mathematically, we can view this translator as a collection of an encoder, F , which takes us from the ambient space to the latent space, $F : \mathfrak{X}_{mvt,1} \mapsto \mathfrak{Z}$, and a decoder, G which takes us from the latent space back to our ambient space, $G : \mathfrak{Z} \mapsto \mathfrak{X}_{mvt,2}$. The encoder-decoder architecture is a design decision outside the scope of this dissertation, but common choices include Variational Autoencoder (VAE) and Transformer-based networks [120]. However, we can generally say that our encoder architecture is parametrized by some collection of variables, ϕ , and our decoder parametrized by θ . And so, notationally, we can view this problem as minimizing the distance between $\xi_\phi = F_\phi \mu_{mvt}$ and ξ , as well as minimizing the distance between $\mu_{mvt,\theta} = G_\theta \xi_\phi$ and μ . The specifics of the math are outside the scope of this dissertation, but for interested readers, I recommend reading Jong Le’s Geometry of Deep Learning, Chapter 13 [129], which discusses metrics on probability spaces, multiple forms of divergence, and the requisite geometric and statistical intuition behind how these types of architectures work.

5.2.2 A Kinematics Translator

The primary goal of a kinematics translator is to develop a sufficiently rich representation of a patient’s latent kinematic space, \mathfrak{Z} , with the smallest possible number of images required. This is achieved by enabling the “translator” to decode, for example, “stair rise” kinematics from “walking” kinematics without needing to explicitly measure “walking” kinematics. This has obvious benefits if one is trying to reduce the clinical footprint of autonomous kinematics measurements.

5.2.2.1 Methods and Data

The training data used to build this network would come from the same published studies used for training our segmentation neural network and validating our autonomous algorithm

(Chapter 3). To start, kinematics were grouped by movement (e.g. walking, stair rise, lunge, etc.), and then we created “translation pairs” for different movements from each patients. We standardized all kinematics data using B-splines and interpolation so that each movement was represented with 100 points. These 100 points at each anatomic rotation/translation measurement can be thought of as a “word” in our translation paradigm, meaning that for any given translation task, we are translating six “words” into six “words”. Each of these 6 kinematics measurements for movement one would be the input to our network, and the desired output are the six kinematics measurements from movement two. With a sufficient amount of data, this would build up a rich representation of our latent space, \mathcal{Z} , such that it can be directly sampled or analyzed to learn about the underlying kinematics of a patient. Unfortunately, a lack of standardization caused three major problems when performing this analysis: (1) Different groups calling the different movements the same thing, (2) Different groups using different movements, and (3) Different groups measuring kinematics at different and non-standard flexion angles.

5.2.3 Problem 1: Groups calling different movements the same thing

Even with a brief literature search, one can find many examples of different groups calling the different activities the same name. The three most pernicious movements were “squat”, “lunge”, and “deep knee bend”. “Step Up” also had inconsistencies in the height of the stair. Typically, research done by the same group was standardized, but between groups there was minor resemblance, but never quite the same exact movement.

A lunge ranged between both feet on the floor, to a raised stair of variable height. The distance between the feet was typically not specified. When images were shown, the width of the feet ranged from nearly back-toe touching front-heel, to a more standard lunge with at least a foot between the back foot and front foot.

A squat typically involves both feet next to each other, and the participants bending down as far as they can. However, the placement of the feet with respect to each other (narrow or wide), and the direction of the toes (straight forward or pointed outward) were often not specified. Additionally, some groups defined a squat as having staggered feet, which bears striking

similarity to what other groups appear to call a “deep knee bend”. Unfortunately, the specifications of the movements were often not provided, just the name, causing tremendous difficulty in pairing different kinematics sequences between research groups.

5.2.4 Problem 2: No standardized set of movements to measure

Because kinematics measurements are primarily a research tool and have not been adopted as a clinical standard of care, the activities performed are entirely at the discretion of the research group. This leads to different research groups having their study participants perform different sets of activities. When trying to build a universal translator, one of the key components is having a large enough set of paired movements from single patients. For example, a large set of both “walking” and “stair rise” kinematics are needed to reliably build a network that could translate between the two. Unfortunately, few groups measured the same two movements reliably, leading to a paucity of paired kinematics data on which a translation algorithm could be built.

5.2.5 Problem 3: Groups measuring kinematics at different flexion angles

Another key issue in the proposed datasets is the flexion-angle resolution at which different groups measure kinematics. Some groups measure kinematics at every n^{th} frame, typically resulting in a flexion resolution of $2 - 5^\circ$. These measurements are able to accurately capture the knee during the entire range of motion, and hopefully, provide a robust analysis of small kinematics changes between patients.

However, other groups only measure kinematics at prescribed flexion angles (typically 30, 60, 90, 120), which loses resolution and comparative power for small motions. If, for example, the main difference between a healthy and pathological post-operative knee occurs between $30 - 60^\circ$, then these lower resolution measurements will be relatively useless at providing meaningful data for a comprehensive database or kinematics translation paradigm. The interpolated values between these two extrema of measurement would fill the latent space with, at best, useless, at worst, completely incorrect, values.

Of note, one of the main reasons for the choice of performing measurements at these prescribed angles, which typically only requires 3/4 measurements per movement sequence, is

the time to generate a report. Manual registration is time-consuming, and some groups do not feel that the extra time to measure the entirety of the movement is worth the additional accuracy. However, with widespread adoption of the proposed JointTrack Machine Learning (Chapter 3), the human supervision for these measurements is completely eliminated, allowing these groups to take more robust measurements without the previously necessary manual registration.

5.3 Toward Generating Synthetic Biomechanics Data

Many of the issues encountered during the “kinematics translator” are directly applicable to generating synthetic kinematics data as well. Fundamentally, the core challenge remains consistent: converting an interpretable latent space into actionable kinematics measurements. This process necessitates a robust latent space as the source for generating synthetic data, which runs into exactly the same difficulties as trying to build a kinematics translator. The lack of standardization of kinematics measurements, as well as consistently reported post-operative outcomes, means that it would be nearly impossible to train a latent space that is both interpretable (e.g. being able to generate a “healthy” or “failing” kinematics sequence) and robust (i.e. $\xi_\phi \pm \delta = \xi$).

One of the main benefits of having a tool to easily, accurately, and autonomously measure kinematics data is that the door will be open to creating standard procedures for these measurements. The next step in adopting this technology clinically involves establishing a universal framework that both clinicians and researchers can utilize when performing a kinematics evaluation. With the spread of anonymized health datasets, a kinematics dataset containing thousands of patients all performing the same activities, and each having the same post-operative metrics recorded, would pave the way for quantitative assessment and correlation of kinematics data to outcome.

CHAPTER 6

THIS WILL DEFINITELY WORK ON SHOULDER IMPLANTS, RIGHT?¹

Another common arthroplasty (TSA) procedure is total shoulder replacement, which involves the removal and replacement of the distal end of the glenoid/scapula and the proximal end of the humeral head. Researchers, implant manufacturers, and surgeons, driven by similar motivations for understanding post-operative Total Knee Arthroplasty (TKA) kinematics, show equal interest in examining post-operative TSA kinematics. Despite differing from TKA outcomes, a significant portion of TSA patients report dissatisfaction, predominantly attributing it to mechanical limitations or instability.

For the past twenty years, researchers have explored both anatomical and reverse total shoulder arthroplasty kinematics [23, 66, 83, 85, 114], attempting to draw connections between different implants and surgical techniques to postoperative shoulder dynamics and range of motion. For the same reasons that a reliable, fast, clinically practical, and fully-autonomous kinematics measurement platform would be desirable for clinicians operating on post-operative total knee arthroplasty (Chapter 3), it would also be desirable for clinicians working on total shoulder arthroplasty.

Unfortunately, the direct application of the same pipeline to shoulder implants proved unsuccessful. This dissertation chapter is structured into three sections. Initially, the methods and results of applying the existing framework to measuring TSA implant kinematics will be discussed, including an exploration of encountered pitfalls. Subsequently, modifications made to the model-image registration cost function aimed at addressing some of the limitations specific to TSA kinematics will be examined. Finally, a geometric first-principles approach adopted to further diagnose inherent issues in kinematics measurement will be detailed, along with methodological recommendations for others interested in conducting similar measurements. The concluding chapter is currently under review for publication in the Journal of Computers in Biology and Medicine.

¹No

6.1 JointTrack Machine Learning on Total Shoulder Arthroplasty Implants

6.1.1 Introduction

The successful application of JTML to TKA implants suggested potential applicability to other implant types and joints. This hypothesis gained credence from JTML's consistent performance across diverse TKA implant styles, spanning posterior stabilized and cruciate retaining designs, as well as variations in the peg design of the tibial baseplate. Consequently, the TKA experimentation framework was replicated, applying it to TSA implant data, to assess whether this success could be mirrored in a different joint context. This section systematically categorizes the challenges encountered in adapting JTML for TSA, detailing each issue and its implications on the results.

6.1.2 Methods

The study utilized 823 post-operative reverse TSA (rTSA) images, complete with human-supervised kinematics, sourced from Nagoya University in compliance with IRB guidelines. These images were obtained using single-plane fluoroscopy to measure glenohumeral kinematics in patients performing anonymized movements. The collected data for each patient included deidentified radiographic images, imaging calibration files, and manufacturer-supplied glenoid and humeral implant surface geometry files.

The same CNN architecture previously used for TKA implants [123] (Chapter 3) was employed, maintaining an 80/20 training/testing split. A key consideration in the methodology was the limited availability of human-supervised rTSA images with kinematics compared to TKA. To address this, the training set was augmented with non-affine transformations, specifically grid distortion and elastic transform [25]. While such transformations increased training times in the TKA pipeline, their computational intensity was manageable given the smaller rTSA image dataset, enhancing the network's generalization capability for rTSA image segmentation.

Next, the DIRECT-JTA algorithm from the JTML suite was applied to rTSA images, evaluating the autonomous kinematics measurement platform. The efficacy of the algorithms will be assessed by comparing the root-mean-square difference between autonomous and

human-supervised kinematic measurements on this novel test set.

6.1.3 Results

Table 6-1. Root mean squared differences between JointTrack Machine Learning optimized kinematics and manually registered kinematics on single-plane fluoroscopy

Implant Type	x_{trans} (mm)	y_{trans} (mm)	z_{trans} (mm)	x_{rot} (°)	y_{rot} (°)	z_{rot} (°)
Humeral	8.46	8.64	152.78	22.59	64.74	11.81
Glenosphere	0.97	1.44	32.58	13.72	26.40	8.30
Femoral	0.57	0.39	26.95	0.66	0.73	0.60
Tibial	0.67	0.64	27.17	1.63	2.74	0.66

6.1.4 Discussion

The results obtained were suboptimal, defying the general intuition that a robust segmentation network would naturally lead to successful outcomes. It appears this challenge is akin to the so-called “symmetry trap” encountered with tibial implants, where a symmetric axis in a 3D object presents difficulties in model-image registration optimization. Broadly, the errors were categorized into two main groups. The first category related to the internal/external rotation axis. The semi-cylindrical shape of the humeral implant along the internal/external rotation axis is likely to decrease sensitivity to changes in shape during different rotation angles. This decreased shape sensitivity, compounded by any imperfections in the segmentation, likely made it extremely difficult for the optimization routine to identify the global minima. To address the issue of decreased shape sensitivity, a first-principles geometric approach to shape descriptors has been embarked upon, which will be elaborated upon in the Shape Sensitivity Analysis study (Section 6.3). The second category involved the distal end of the humeral implant registering correctly, while the proximal articular surface did not align as expected. This issue may arise from the image similarity cost function’s lack of preference for any specific region along the implant’s contour, thereby allowing it to become trapped in a semi-reasonable local minima. To mitigate the issue stemming from the cost function’s non-preferential treatment of the contour, development of novel cost functions is underway, as will be discussed in the subsequent section (Section 6.2).

6.2 Improving Model-Image Registration

6.2.1 Introduction

Given the relatively poor performance of the standard optimization algorithm (DIRECT [39, 60]) and the cost function (L_1 -distance or Hamming Distance [39]), this study initially investigated the potential for a more robust image similarity representation to enhance performance (Section 1.1.4). The identification of global minima in this model-image registration challenge was facilitated by exploring several approaches to enhance image similarity representation.

The first approach involved attempts to enhance the convexity of the problem. With the existing formulation, the cost was observed to reach maximum error ($\sum I + P$) when there was no overlap between the projection and the CNN, regardless of the projection's deviation, whether it be 5 or 500 pixels. This highlighted the need for a more nuanced error gradient.

Secondly, an exploration of the perceptual psychology of shape was undertaken [3, 4]. Given that manual registration is considered the benchmark for ground-truth kinematics, an understanding of human perception of shape differences and overlaps was deemed crucial. Consultations with surgeons and engineers were conducted, providing invaluable insights into refining the registration approach, with an emphasis on identifying effective procedures and features.

Exploring the addition of new cost parameters for JointTrack Machine Learning faced certain constraints. The introduction of new cost functions was required to be non-conflicting with the Hamming Distance, necessitating their concurrent minimization with the Hamming Distance for all additional metrics. Furthermore, the algorithm was required to support parallel processing in CUDA without significantly increasing the computational burden per image. Lastly, maintaining the existing efficiency, characterized by the necessity for only one kernel per iteration to preserve application performance, was considered crucial.

6.2.2 Improving Error Gradient

For gradient enhancement, it is essential to establish notions of *closeness* and *farness* in the image plane, which transcends the basic *hits* and *misses* of the Hamming distance calculation.

Functions that satisfy this property and provide consistent minima with the Hamming distance are defined as *surface distances* [99, 100]. A surface distance represents the mathematical formulation which captures the concept of closeness or farness between contours in an image plane. Within surface distances, a notable subcategory is *symmetric surface distances*, characterized by the equality $d(a, b) = d(b, a)$; however, this symmetry is not a prerequisite for a metric to be useful. Four primary metrics are widely recommended for the evaluation of surface distance [99, 100].

The first is the Normalized Surface Distance or Normalized Surface Dice (Figure 6-1) [90]. However, surface DICE encounters a similar limitation as the Hamming distance, being maximized at points of no overlap, without discerning between closer and farther estimations.

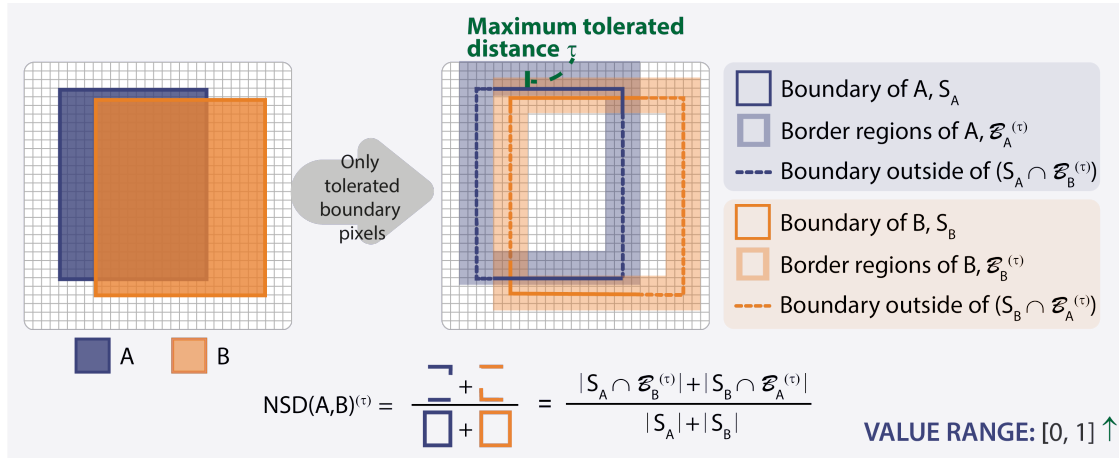


Figure 6-1. A graphical representation of the Normalized Surface Distance from [99, 100].

The second is the Mean Average Surface Distance or Mean Surface Distance (Figure 6-2) [17]. This metric calculates the average of the mean shortest distances from every point on one boundary to any point on the other boundary [99, 100]. A significant drawback of this method lies in its requirement to spawn a sub-kernel for each sampled pixel on the target and estimated contour, substantially increasing the computational load.

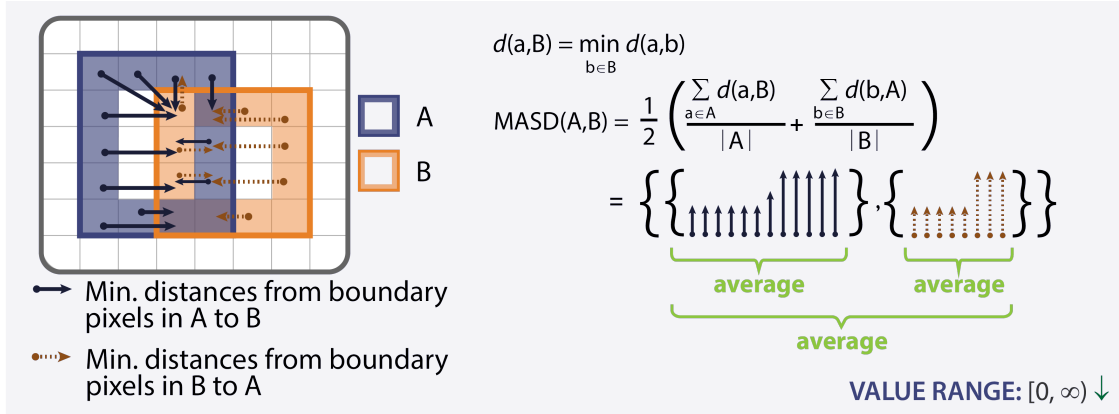


Figure 6-2. A graphical representation of the Mean Average Surface Distance from [99, 100].

The third is the Average Symmetric Surface Distance (Figure 6-3) [130]. This metric represents a symmetric variation of the mean average surface distance, calculating the average distance from each contour to the other, rather than the mean of the average shortest distances. Similar to the Mean Average Surface Distance, this metric also necessitates sub-kernels for each sampled point, significantly increasing the computational requirements per iteration.

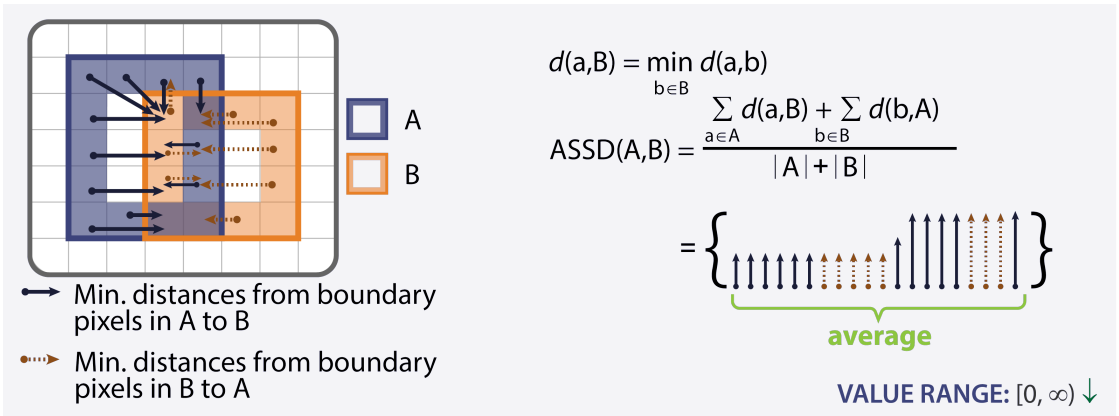


Figure 6-3. A graphical representation of the Average Symmetric Surface Distance from [99, 100].

The last is the Hausdorff Distance (Figure 6-4) [37, 52, 53]. The Hausdorff distance is the maximum distance from a point on one boundary to the nearest point on another boundary. Typically the Hausdorff distance for an entire countour is taken as the average of the Hausdorff distances for a series of sampled points on the target contour. Like the previous two, the Hamming distance requires sub-kernels for every sampled point, and so it is not feasible.

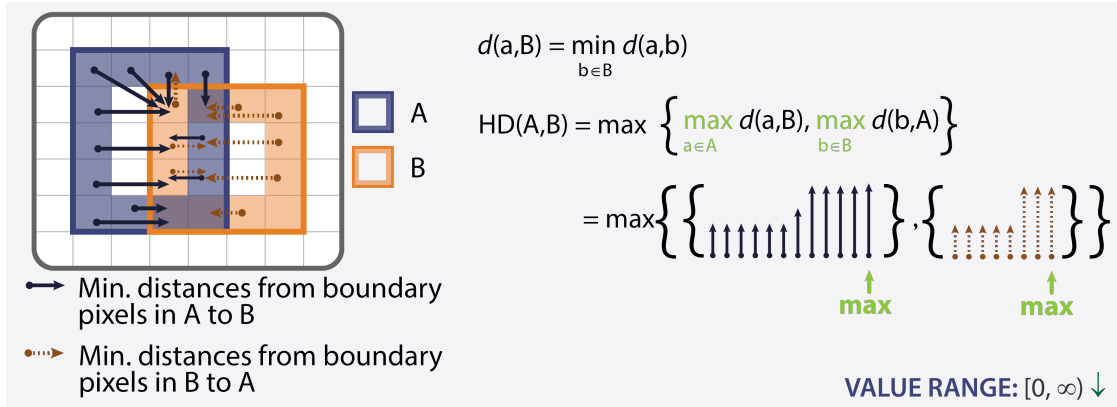


Figure 6-4. A graphical representation of the Hausdorff Distance, taken from [99, 100].

At this point, none of the recommended distance metrics were found to satisfy the criteria for a feasible cost function capable of introducing an error gradient. Based on the limitations identified in each approach, the pre-computation of as many values as possible to reduce the algorithmic load during optimization was considered ideal. In previous studies, 3D distance maps were pre-computed to facilitate medical model-image registration [75, 137]. Consequently, a cost function was devised that utilizes pre-computed distance maps to introduce an error gradient, without the need to spawn multiple kernels during each optimization iteration.

6.2.3 Modified Mean Distance Cost Function

Initially, rather than calculating the average distance across all target points – a process that would necessitate spawning multiple sub-kernels – a distance map encoding the distance to the *nearest point* on the target contour was introduced.

With an arbitrary image point defined as p_{xy} , and the target contour defined as T , we can express this distance map as a grid, $DM_{xy}(T) = \min_{t \in T} d(p_{xy}, t)$, where $d(p_{xy}, t)$ is any distance function that you want to use. In our case, we use the L_1 -distance for efficient computation. We use OpenCV's `distanceTransform()` function for this [19].

With an arbitrary image point defined as p_{xy} , and the target contour defined as T , this distance map can be expressed as a grid, $DM_{xy}(T) = \min_{t \in T} d(p_{xy}, t)$, where $d(p_{xy}, t)$ represents any chosen distance function. In this case, the L_1 -distance was selected for efficient computation, utilizing OpenCV's `distanceTransform()` function for this purpose [19].

Subsequently, a notion of distance between the projected contour and the target contour can be expressed by calculating the average of the element-wise multiplication between the projection and the pre-calculated distance map (Eq. 6-1). This approach offers the significant advantage of requiring only a single kernel for each iteration (iterating once per projection and performing a multiplication and atomic addition in memory) as well as sharing a minimum with the Hamming distance. This is evident by observing that $DM_{x,y} = 0$ for points on the target contour, indicating that if $Proj_{x,y}$ were perfectly aligned with this contour, the summation would result in the addition of zeros.

$$J = \frac{\sum_{(x,y) \in \text{Image}} Proj_{x,y} DM_{x,y}}{\sum_{(x,y) \in \text{Image}} Proj_{x,y}} \quad (6-1)$$

Unfortunately, the results of this endeavor did not improve the overall performance of the DIRECT algorithm in finding a global minimum for rTSA implants. The performance was found to be very similar to the previously poor performance when using the Hamming distance cost function.

6.2.4 The Psychology of Shape and Mimicking Human Operators

Early research in computer vision was closely tied to the psychology and neurology of human perception. Humans possess a remarkable ability to describe what they see, either through language or mathematical notation. The task of programmatically replicating this skill in computers continues to present significant challenges. Although some multi-modal speech/vision models have shown promise in a general sense, they lack a deep technical understanding of the visual content they process.

Historically, the first attempts to mathematically describe shapes, vision, images, and curves were rooted in psychological literature [3, 4, 68, 69]. This foundation appears appropriate for enhancing rTSA model-image registration. The task essentially involves decomposing a contour into its basic shape and elemental components.

In the mid-1950s, psychologist Fred Attneave made significant contributions to the understanding of visual information redundancy and the identification of regions in images and

shapes that humans perceive as highly salient [3, 4]. He discovered that humans could recognize most images even when the shapes were significantly simplified, retaining only the most relevant features. Attneave identified regions of high curvature, areas with a relatively high change in the normal vector, as carrying the most information about a shape (Fig. 6-5). He observed that most other line segments were superfluous for shape recognition.

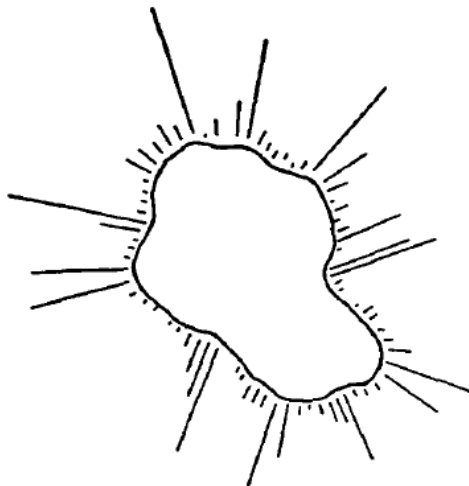


FIG. 2. Subjects attempted to approximate the closed figure shown above with a pattern of 10 dots. Radiating bars indicate the relative frequency with which various portions of the outline were represented by dots chosen.



FIG. 3. Drawing made by abstracting 38 points of maximum curvature from the contours of a sleeping cat, and connecting these points appropriately with a straightedge.

Figure 6-5. Some representative examples of the experiences that Fred Attneave performed to establish the primacy of high curvature as salient in shape recreation and recognition, from [3].

This understanding resonates with surgeons and engineers experienced in manual registration of rTSA implants. They report that transitioning an image frame from “good” to “great” hinges on achieving visually precise alignment between the corners and edges of the projected 3D model and the fluoroscopic image. Their emphasis on the importance of accurately aligning high-curvature regions aligns with Attneave’s findings.

6.2.5 Developing a Cost Function for Aligning High-Curvature Regions

Informed by these findings, the aim was to develop a cost function that facilitates the alignment of high-curvature regions between the target shape and the projected shape. The



Figure 6-6. Some different model views of a manually registered humeral and glenoid implant in an rTSA system. Of note, each view gives the user a different type of feature to focus on. The original view allows the user to determine the relative orientation based on shading, the transparent view allows the user to see the underlying fluoroscopic image, and the solid view allows the user to focus on specific regions of error. Each is crucial to performing manual registration.

constraints, as outlined in the previous chapter, remained: any new cost functions must reach a global minimum concurrently with the Hamming distance, and computational efficiency is paramount.

Given that there is a finite number of high-curvature regions for any given implant, and that their total count can be limited, the disadvantages associated with many surface distances appeared mitigatable. This mitigation strategy would involve focusing exclusively on these high-curvature regions rather than every pixel along the surface. However, this approach introduced the challenge of having to spawn sub-kernels for each iteration.

To circumvent this, an *asymmetric surface distance*, where $d(a,b) \neq d(b,a)$, became necessary. Such a distance metric would allow for the pre-computation of a distance map based on the target shape. Since this target does not change with each iteration, and memory usage is manageable due to the small number of points required for distance calculation, this approach seemed promising. By focusing on pre-computed distances for critical high-curvature points, it was possible to maintain computational efficiency while potentially improving the accuracy of alignment.

6.2.5.1 Finding Regions of High Curvature

The first step in implementing this cost function involves determining the regions with high curvature in the contour, a task that is not as straightforward as it may appear. This requires a contour-extraction algorithm, a discrete curvature equation, and a method for automatically selecting regions of high curvature.

OpenCV's `findContours` function [19] is utilized, which provides a pre-specified number of contiguous contour points following an algorithm proposed by Suzuki and Abe [115]. For the implementation at hand, 200 contour points are extracted.

For a discrete implementation of curvature, we turn to Menger's Algorithm [77]. This method defines the discrete curvature as the reciprocal of the radius of a circle fit through three points along the contour (Eq. 6-2). Typically, a window of size t is defined to expand the proximity of the three points along the curvature and make the calculations more robust to noise. In our implementation, $t = 18$.

For a discrete implementation of curvature, Menger's Algorithm [77] is implemented. This method defines the discrete curvature as the reciprocal of the radius of a circle fit through three points along the contour (Eq. 6-2). Typically, a window of size t is defined to increase the proximity of the three points along the curvature, making the calculations more robust to noise. In this implementation, $t = 18$.

$$C_i = \frac{1}{radius(p_{i-t}, p_i, p_{i+t})} \quad \text{where} \quad (6-2)$$

$$radius(x, y, z) = \frac{4 \cdot Area}{|x - y||y - z||z - x|}$$

Given the utilization of neural network segmentation for the contour, the presence of some noise in the contour (Fig. 6-7) is inevitable, leading to noise in the curvature calculations. Noise was mitigated by applying a 1-D Gaussian convolution to the array of curvature values,

employing a 9-wide Gaussian kernel. Regions of the highest curvature were then represented as peaks along the plot (Fig. 6-7).

To programmatically extract regions with high curvature, two steps were undertaken. Initially, curvature values were filtered to exclude those where $c_i \leq \mu_{curvature} + 1.5\sigma_{curvature}$, ensuring the selection of only high curvature points. Subsequently, inflection points of the first derivative were identified to locate regions where the curvature transitioned from a positive to a negative derivative, indicative of the "peak" of that curvature region. The points identified by this algorithm correspond precisely to the points where the specific contour exhibits the highest curvature, aligning with the regions that human operators intuitively identified as high curvature areas.

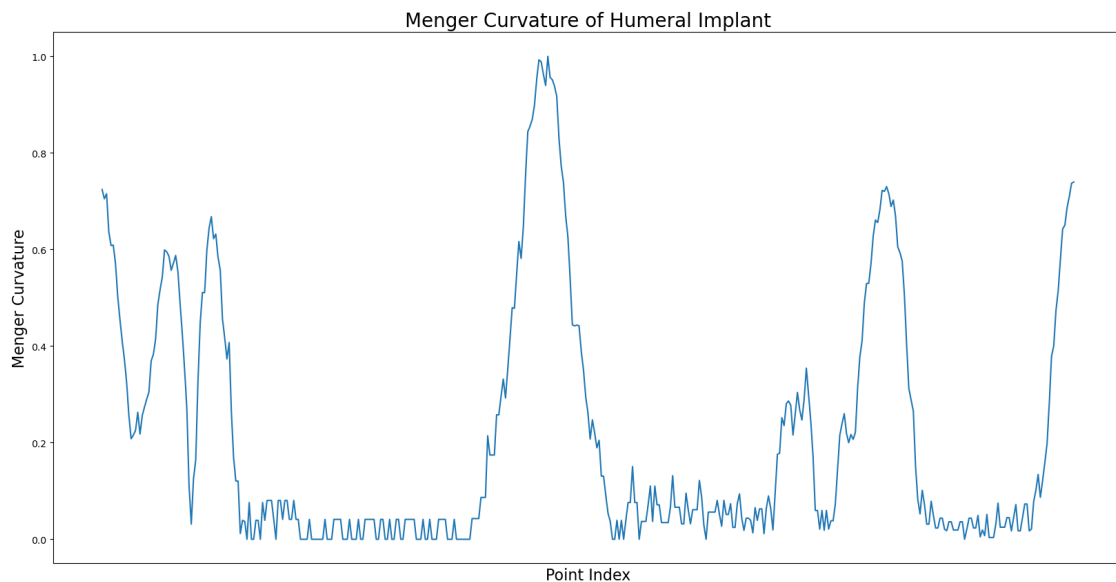


Figure 6-7. A plot demonstrating the values of the Menger Curvature along the contour of an rTSA humeral implant. The regions of high curvature are the peaks of the plot.

6.2.5.2 Modified Asymmetric Surface Distance

Upon establishing a set of keypoints representing the regions of the highest curvature, the next step involved determining a pre-computable distance metric for creating a cost function. The Hausdorff distance was ruled out due to its focus on the maximum distance point rather than incorporating each point's contribution to the overall distance. The Symmetric distance was also

dismissed in favor of seeking an asymmetric function to avoid the necessity of spawning sub-kernels during iteration calls. Thus, the Mean Surface Distance was selected. The modified approach eliminated distance calculations from the projection to the target (creating asymmetry) and focused only on distances centered at the selected keypoints. Distance maps to each keypoint were pre-computed using OpenCV’s `distanceTransform()`, and element-wise multiplication was applied to identify the nearest projected point to each keypoint (Eq. 6-3).

$$J = \frac{\sum_{k \in \mathbb{K}} (\min_{p \in Proj}(p \cdot DM_k))}{N}$$

where

\mathbb{K} = Set of all keypoints (6-3)

N = Number of keypoints

DM_k = Distance map for keypoint k

p = Single point on projection silhouette

Unfortunately, this approach also resulted in suboptimal performance. Despite algorithmically identifying salient image features and minimizing the distance of these points to the estimation, the optimization routine failed to accurately match the solution to human-supervised registration.

6.2.6 Discussion

This section delved into the exploration of applying JointTrack Machine Learning to reverse Total Shoulder Arthroplasty implants. Although the applications did not yield a successful solution for rTSA model-image registration, they contributed to expanding the body of knowledge in the field.

First, all algorithms were rigorously tested on TKA implant registration to ensure no adverse impact on the established performance of JTML. Given the strengths listed for each algorithm, they might offer stronger and more robust performance than the traditional Hamming

distance for TKA implants. This hypothesis warrants further testing and evaluation, suggesting that the described additions could significantly improve JTML’s convergence speed and overall accuracy.

Moreover, although the methods did not succeed in aligning rTSA implants, they demonstrated a comprehensive understanding and a valuable resource for model-image registration endeavors. The methodical and calculated approach to employing a wide array of mathematical tools to tackle a challenging problem is beneficial for anyone facing a similar technical obstacle.

Lastly, the inability of the methods to accurately perform model-image registration highlighted potential deficiencies in the overall pipeline. One such deficiency could be attributed to the performance ceiling of the CNN segmentation, though this seems unlikely given the state-of-the-art IOU scores. Incorporating a surface-based metric into the neural network error functions might yield a more robust segmentation. Another limitation could be the use of Euler angles in the optimization process, where a more robust rotation parametrization, such as Quaternions, might mitigate the non-commutativity issues. Additionally, the shape of humeral implants compared to TKA implants, which are more “cylindrical,” suggests that minor orientation changes do not significantly alter the projected shape, complicating optimization efforts.

Each identified deficiency represents a promising avenue for future research and development. The exploration of these potential areas of improvement could lead to significant advancements in model-image registration techniques. The final section of this chapter will address the potential sensitivity of the projected shape to input orientation, further exploring the nuances of this complex and evolving area of study.

6.3 2D Shape Projection Sensitivity Analysis

Understanding the in-vivo kinematics of total joint replacement has been essential in implant design, post-operative assessment, and predicting wear and failure patterns for nearly three decades [11, 13, 41]. Recent advancements in computer vision and machine learning have

enabled these analyses for total knee arthroplasty (TKA) in a fully autonomous and clinically practical setting, utilizing single-plane fluoroscopy [21, 58]. However, using only a single camera inherently limits the measurement accuracy due to loss of depth perception and the introduction of ambiguous projected shapes during optimization [8, 39, 81, 137]. The observed limitation, predominantly impacting mediolaterally symmetric tibial implants, led to a phenomenon termed “symmetry traps.” In such instances, two distinct three-dimensional orientations of the implant produce indistinguishable two-dimensional projected geometries. A machine learning algorithm was developed to address these symmetry traps in symmetric tibial implants. This algorithm was trained to recognize accurate anatomic orientations and correct images caught in optimization minima [59]. However, this approach required the symmetric implant to register into one of the two potential local minima, each corresponding to a distinct “symmetry trap.”

The application of the same optimization routine and cost function [39, 58] to reverse total shoulder arthroplasty (rTSA) resulted in significantly lower performance compared to its application in TKA implants (Table 6-1) [58]. This suboptimal performance manifested primarily along the internal/external rotation axis, which has salient features often occluded by the glenosphere implant in frontal-plane fluoroscopy (Fig. 6-8). Additionally, this axis is nearly rotationally symmetric for both the humeral and glenosphere implants. Poor rotation registration also increases translation errors, as the silhouette shape of the estimated pose is wholly different from the fluoroscopic image, causing imprecise translation alignment along all axes. In a manual registration setting [86], different combinations of model and image views are utilized to overcome these limitations (Fig. 6-6).

The current investigation delves into the fundamental shape aspects of each arthroplasty system, with a focus on developing a method for autonomously measuring rTSA kinematics from single-plane fluoroscopy. Central to this is the use of Invariant Shape Descriptors, particularly the Invariant Angular Radial Transform Descriptor (IARTD), which offers a mathematically robust approach to describe object shapes [76]. These descriptors are immune to variations in scale, translation, or orientation [134], and are adept at quantifying the relative “nearness”, “farness”,



Figure 6-8. A representative example of poor internal/external rotation of the humeral implant after automated model-image registration using JointTrack Machine Learning [58].

and “uniqueness” of shapes as vector differences. Such properties are valuable for object categorization [101, 121, 122] and kinematics measurement [8], with IARTD’s sensitivity to radial shape differences [76] being particularly beneficial for detailed contour analysis.

The focus of this analysis is on the sensitivity of projected 2D shapes, as depicted by IARTD, to changes in their 3D orientation. This is key to understanding the impact of subtle orientation variations on the projected shape, an aspect integral to shape-based optimization metrics. The ultimate aim is to highlight performance differences in autonomous kinematics measurements between TKA and rTSA implant systems. Additionally, the study seeks to identify areas where imaging methods can be improved to boost the algorithm’s performance.

6.4 Methods

6.4.1 Data Collection

For shape sensitivity analysis, representative 3D models of rTSA humeral and glenosphere implants, as well as TKA femoral and tibial implants, were obtained from a manufacturer. The study focused on a single size for each implant type, as the scale of the shapes was normalized using an Invariant Shape Descriptor, rendering multiple sizes unnecessary for this analysis.

6.4.2 Image Generation

Each implant’s binary silhouette was rendered to a 1024×1024 image plane using an in-house CUDA camera model (CUDA Version 12.1) [87]. The model featured a 1000mm focal

length and 0.3mm per pixel resolution, which are quite typical projection parameters for fluoroscopic images. All imaging tasks utilized an NVIDIA Quadro P2200 GPU.

6.4.3 Invariant Angular Radial Transform

The Invariant Angular Radial Transform Descriptor (IARTD) was selected for its radial direction sensitivity, enabling the detection of subtle contour changes in projected shapes [76]. This sensitivity allows us to address minor changes along the contour of the projected shape, which is a desirable property for determining the minor changes in shape with respect to input orientation.

IARTD computation involves aggregating orthogonal basis components across the unit polar disk, forming a complex moment. Each basis function has an order (n) and a repetition (p). The order can be visualized as concentric rings on the polar disk, and the repetition as the count of slices partitioning the unit disk along θ . For these calculations, the image is normalized so that the center is at $(0, 0)$, and the four corners are at $(\pm 1, \pm 1)$.

Each angular radial transform (ART) coefficient is a complex double integral (Eq. 6-4) over the image in polar coordinates, $f(\rho, \theta)$ multiplied by the ART basis function, $V_{np}(\rho, \theta)$ (Eq. 6-5).

$$F_{np} = \int_0^{2\pi} \int_0^1 f(\rho, \theta) V_{np}(\rho, \theta) \rho d\rho d\theta \quad (6-4)$$

$$V_{np}(\rho, \theta) = A_p(\theta) R_n(\rho) \quad (6-5)$$

The radial basis function includes a complex exponential, $A_p(\theta)$ (Eq. 6-6), ensuring rotational invariance, and a trigonometric transform, $R_p(\theta)$ (Eq. 6-7), to establish orthogonality.

$$A_p(\theta) = \frac{1}{2\pi} e^{ip\theta} \quad (6-6)$$

$$R_n(\rho) = \begin{cases} 1 & n = 0 \\ 2\cos(\pi n \rho) & n \neq 0 \end{cases} \quad (6-7)$$

Phase correction is applied to each ART coefficient (Eq. 6-8, Eq. 6-9) to adjust for differences in in-plane rotation.

$$\phi'_{np} = \phi_{np} - \phi_{n,1} \quad (6-8)$$

$$F'_{np} = F_{np} e^{-jp\phi_{n,1}} \quad (6-9)$$

Subsequently, the final feature vector is formulated by the polar decomposition of each coefficient at every order and repetition (Eq. 6-10). Values from the first two repetitions are excluded, as they do not provide significant information [76]. The complete IARTD feature vector encompasses values of $n = 0, \dots, 3$ and $p = 0, \dots, 8$ per the original authors' suggestion [76].

$$IARTD = \{|F'_{np}|, \phi'_{np}\} \text{ where } n \geq 0, p \geq 2 \quad (6-10)$$

6.4.4 Shape Differences and Sensitivity

In order to quantify the overall change between shapes, a readily interpretable value must be established. To simplify notation, successive rotations are denoted as subscripts, with $R_z R_x R_y$ being represented as $R_{z,x,y}$. If more than 3 rotations are applied successively, the full rotation sequence will be captured as $R_{r_1, r_2, r_3, \dots, r_n}$. Similarly, the application of the IARTD equation to an implant at a specific input orientation $R_{z,x,y}$ is denoted as $IARTD(R_{z,x,y})$. Shape differences were calculated using the central difference equation on the IARTD vector produced from two different orientations. The grid of sampled orientations had extrema of $\pm 30^\circ$ with a step size of 5° for each of the x , y , and z axes. The “differences” along each axis were computed using a positive and negative rotation ($\pm\delta$) of 1 degree. Therefore, for every set of x, y, z rotations, three distinct shape differences are computed, one each for δ_x , δ_y , and δ_z (Eq. 6-11).

For notational brevity, we will condense the total equation to a single $\Delta S(\delta)$, (representing $\Delta Shape$ for a differential rotation δ).

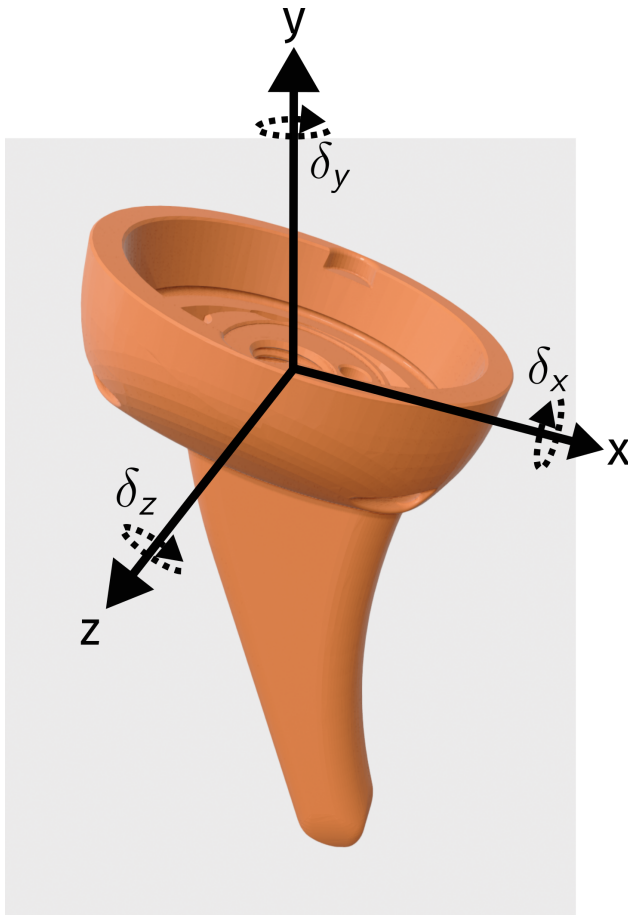


Figure 6-9. A generic manufacturer-provided humeral implant with label x, y, and z rotation axis. Additionally, each of the δ_x , δ_y , and δ_z are shown, corresponding to the rotational directions of each shape descriptor difference.

$$\begin{aligned} \Delta S(\delta)_{z,x,y} \equiv & IARTD(R_{z,x,y,+ \delta}) \\ & - IARTD(R_{z,x,y,- \delta}) \\ \forall \delta \in & \{\delta_x, \delta_y, \delta_z\} \end{aligned} \quad (6-11)$$

The disparate scales of IARTD vector elements necessitate their normalization, ensuring a balanced assessment of global behavior without overemphasis on any individual element. Z-scaling provides a practical approach to normalizing each element relative to its distribution. After z-scaling, the Euclidean norm of each $S(\delta)_{z,x,y}$ is calculated to quantify the total shape

change for a specific differential rotation (Eq. 6-12).

The final step takes advantage of two factors: first, that the in-plane rotations are the first in the Euler sequence (z -axis), and second, that this type of rotation does not affect the in-plane shape. For each x and y input rotation, an average is computed from values where x and y remain constant while z varies (Eq. 6-13). The final values are obtained from this equation, denoted by \mathbb{S} . Individual plots were created for $\mathbb{S}_{x,y}$, corresponding to each differential rotation in x , y , and z , and for each of the four implant types. An analysis of these plots were conducted to assess the performance of JTML optimization and to explore areas where low shape-sensitivity will pose significant challenges for registration-based optimization.

$$\|S(\delta)_{z,x,y}\|_2 \quad (6-12)$$

$$\mathbb{S}(\delta)_{x,y} = \frac{\sum_z \|S(\delta)_{z,x,y}\|_2}{N} \quad (6-13)$$

6.5 Results

The humeral implant exhibited the lowest mean $\mathbb{S}(\delta_y)$ across all implant types (Fig. 6-10) (Table 6-2). This rotation represents the final rotation in our Euler rotation sequence (Z-X-Y) and captures the internal/external rotation of the humeral implant. Additionally, the surface plotted by the humeral shape sensitivity for all $\delta_{x,y,z}$ is much smoother than any of the other plots, demonstrating the relative lack of shape difference for a wide range of input orientations. Several plots showed regions with relatively low sensitivity. Specifically, the glenosphere's δ_y sensitivity along the $y = 0$ axis (Fig. 6-11) and the tibial implant's δ_y sensitivity along the $x = 0$ axis (Fig. 6-13). The femoral implant had the highest average sensitivity ($\frac{\mathbb{S}(\delta_x) + \mathbb{S}(\delta_y) + \mathbb{S}(\delta_z)}{3}$) among all implant types .

6.6 Discussion

The findings correspond closely with initial expectations regarding the sensitivity measurement of projected shapes relative to 3D object orientation and are consistent with areas challenging for JTML optimization. Specifically, the humeral implant showed a generally smooth

Table 6-2. Average projected-shape sensitivity values for each of the implant models.

Implant Type	Average $\mathbb{S}(\delta_x)$	Average $\mathbb{S}(\delta_y)$	Average $\mathbb{S}(\delta_z)$
Humeral	8.83	4.82	7.08
Glenosphere	6.37	6.22	4.86
Femoral	6.88	8.68	4.93
Tibial	9.0	5.52	3.72

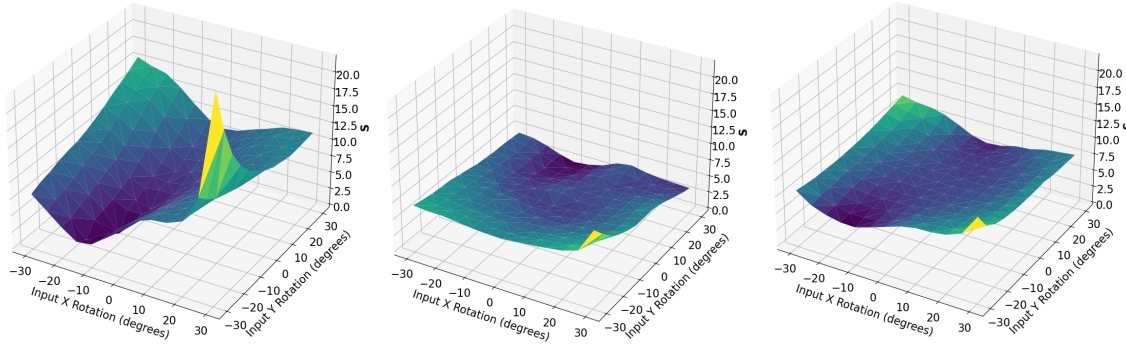


Figure 6-10. The \mathbb{S} plot for a humeral implant for δ rotations along the x, y, and z axis, respectively.

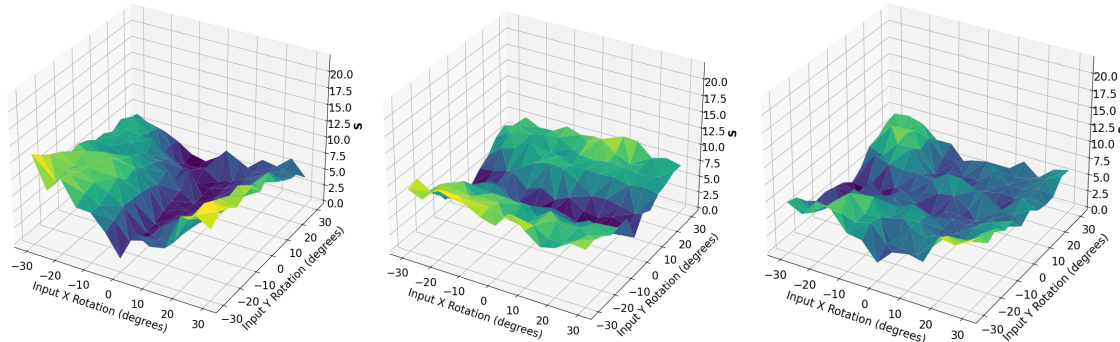


Figure 6-11. The \mathbb{S} plot for a glenosphere implant for δ rotations along the x, y, and z axis, respectively.

and minimal shape sensitivity profile, particularly for δ_y rotations (Table 6-2). Along this axis, the humeral implant is the most cylindrical, meaning we would not expect to see a significant change in the shape descriptor with minor δ_y rotations. Furthermore, it is noteworthy that this axis presented the most significant difficulties in JTML optimization.

Similar intuitive outcomes are observed with the glenosphere implant, which exhibited the lowest average $\mathbb{S}(\delta)$ among all the implant types. This implant primarily consists of an articulation surface closely approximating a spherical shape. Given that the projection of a sphere

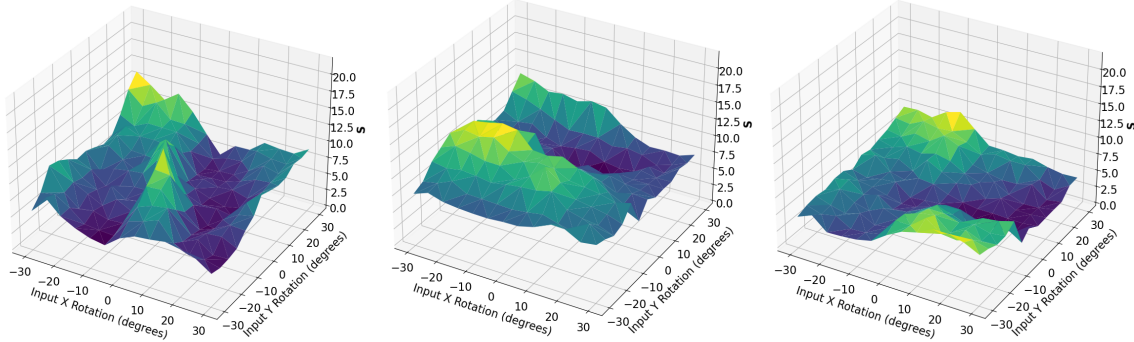


Figure 6-12. The \mathbb{S} plot for a femoral implant for δ rotations along the x, y, and z axis, respectively.

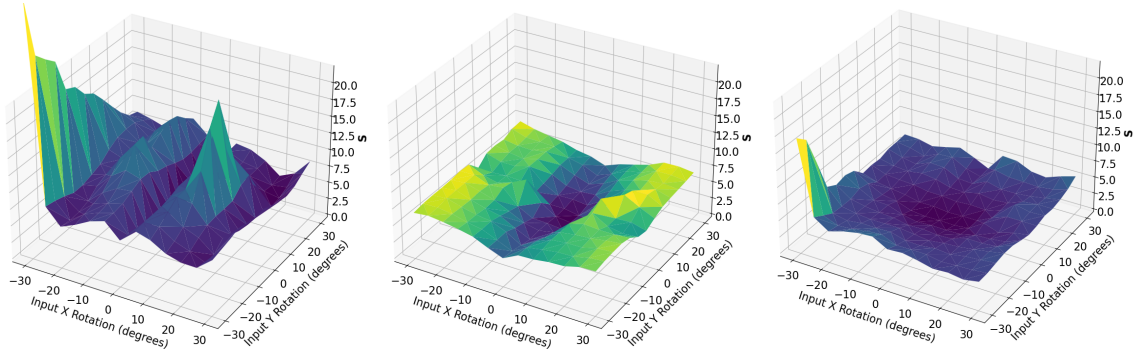


Figure 6-13. The \mathbb{S} plot for a tibial implant for δ rotations along the x, y, and z axis, respectively.

(a circle) remains constant regardless of the sphere's orientation, the closer a shape is to a spherical form, the lower its overall shape sensitivity is expected to be.

The observed shape sensitivity of the tibial implant with respect to δ_y rotation aligns with the concept of symmetry traps. There is a consistently low shape sensitivity along the line where $x = 0$. This axis, associated with internal/external rotation, is the same one that contributes to symmetry traps, where two different 3D orientations result in an identical projected shape. In terms of this analysis, the ΔS value would be 0 for these two orientations of the tibial implant.

This study sheds light on an important aspect of JointTrack Machine Learning, particularly the use of Euler angles in the DIRECT-JTA optimization routine. Currently, the optimization does not involve independently varying all angles within a body-centered reference frame, as this approach is not conducive to hyperbox creation [39, 60]. Instead, optimization is performed over a range of ordered rotations, projected through the sequence $R_zR_xR_y$. The challenges the humeral

implant encounters in aligning the y -axis illustrate that this ordered sequence, especially with a symmetric final axis, can hinder the convergence process.

Beyond the inherent shape sensitivities, such optimization limitations motivate exploring alternatives to Euler angles. Performing registration optimization directly on the Special Orthogonal group $SO(3)$ poses an intriguing direction. $SO(3)$ encapsulates all possible 3D rotations in a mathematically convenient structure (A *Lie Group*, which is both a manifold and a group) [110, 136]. By optimizing on this manifold instead of Euler angle parametrizations, issues with gimbal lock and cascading rotation effects can be avoided. However, most manifold optimization is specifically tailored to derivative-based optimization, which is not currently supported by the DIRECT-JTA algorithm that JointTrack Machine Learning incorporates [39, 58, 60]. This limitation motivates either a restructuring of the current optimization methods to incorporate derivative information, or to explore the potentials of derivative-free (black-box) optimization [5] over manifolds.

Historical manual registration software heavily relied on bony landmarks within images to disambiguate challenging implant poses. As landmarks, the tibial tuberosity, fibula, and bicipital groove were vital in identifying the specific orientation of implants, all of which are visible and utilized by the user in a manual registration setting (Fig. 6-6). To accurately assess implant kinematics in highly symmetric unicompartmental knee arthroplasty, surface meshes of femoral and tibial components were incorporated into the registration process [12]. These bone models were particularly beneficial in addressing implants' internal/external rotation along semi-symmetric axes. Additionally, the use of densely selected keypoints in the precise measurement of preoperative shoulder kinematics through biplane fluoroscopy has been documented [23], with keypoint registration achieved via a modified Perspective-N-Points optimization routine. Furthermore, intensity-based metrics have played a crucial role in the accurate determination of healthy tibiofemoral kinematics [6]. Rather than minimizing the Euclidean distance of projected model keypoints, these methods leverage digitally reconstructed radiographs and directly compare the intensity values of the x-ray image and the projection

estimate. Thus, utilizing bony landmarks for measuring implant kinematics presents a robust and reliable approach to measuring accurate joint kinematics in clinical environments.

6.7 Concluding Remarks

This study demonstrates intrinsic differences between implant types regarding projected 2D shape sensitivity. Measurement difficulties aligned with low sensitivity along problematic axes—humeral internal rotation and tibial symmetry traps. Fundamentally, small orientation changes yielded negligible 2D variability for near-symmetrical geometries and axes. While inherent shape constraints limit data extractable solely from single-plane fluoroscopic silhouettes, incorporating additional image information like bone offers promise. Despite unavoidable ambiguity along select dimensions, boosting descriptor sensitivity and employing precise anatomical constraints could enable robust clinical tracking. Overall, relating optimization performance to shape response underscores routes toward accurate autonomous kinematic analysis.

LIST OF REFERENCES

- [1] *BMUS: The Burden of Musculoskeletal Diseases in the United States*, <https://www.boneandjointburden.org/>.
- [2] Agency for Healthcare Research and Quality, *HCUP Fast Stats*, <https://hcup-us.ahrq.gov/faststats/NationalProcedures>.
- [3] Fred Attneave, *Some informational aspects of visual perception.*, Psychological Review **61** (1954), no. 3, 183–193.
- [4] Fred Attneave and Malcolm D. Arnoult, *The quantitative study of shape and pattern perception.*, Psychological Bulletin **53** (1956), no. 6, 452–471.
- [5] Charles Audet and Warren Hare, *Derivative-Free and Blackbox Optimization*, Springer Series in Operations Research and Financial Engineering, Springer International Publishing, Cham, 2017.
- [6] N Baka, M de Bruijne, T van Walsum, B L Kaptein, J E Giphart, M Schaap, W J Niessen, and B P F Lelieveldt, *Statistical Shape Model-Based Femur Kinematics From Biplane Fluoroscopy*, IEEE TRANSACTIONS ON MEDICAL IMAGING **31** (2012), no. 8, 11.
- [7] P. N. Baker, J. H. van der Meulen, J. Lewsey, and P. J. Gregg, *The Role of Pain and Function in Determining Patient Satisfaction After Total Knee Replacement: Data From the National Joint Registry for England and Wales*, The Journal of Bone and Joint Surgery. British volume **89-B** (2007), no. 7, 893–900.
- [8] S.A. Banks and W.A. Hodge, *Accurate measurement of three-dimensional knee replacement kinematics using single-plane fluoroscopy*, IEEE Transactions on Biomedical Engineering **43** (1996), no. 6, 638–649.
- [9] Scott A. Banks, *Model based 3D kinematic estimation from 2D perspective silhouettes - application with total knee prostheses.pdf*, Ph.D. thesis, 1992.
- [10] _____, *What Postoperative Outcome Measures Link Joint Stability to Patient Satisfaction?:*, Journal of the American Academy of Orthopaedic Surgeons **25** (2017), S40–S43.
- [11] Scott A. Banks, Evan Deckard, W. Andrew Hodge, and R. Michael Meneghini, *Rationale and Results for Fixed-Bearing Pivoting Designs in Total Knee Arthroplasty*, The Journal of Knee Surgery **32** (2019), no. 07, 590–595.
- [12] Scott A. Banks, Benjamin J. Fregly, Filippo Boniforti, Christoph Reinschmidt, and Sergio Romagnoli, *Comparing in vivo kinematics of unicondylar and bi-unicondylar knee replacements*, Knee Surgery, Sports Traumatology, Arthroscopy **13** (2005), no. 7, 551–556.
- [13] Scott A. Banks and W. Andrew Hodge, *2003 Hap Paul Award paper of the International Society for Technology in Arthroplasty*, The Journal of Arthroplasty **19** (2004), no. 7, 809–816.

- [14] Scott A. Banks, George D. Markovich, and W. Andrew Hodge, *In vivo kinematics of cruciate-retaining and -substituting knee arthroplasties*, The Journal of Arthroplasty **12** (1997), no. 3, 297–304.
- [15] C. Bradford Barber, David P. Dobkin, and Hannu Huhdanpaa, *The quickhull algorithm for convex hulls*, ACM Transactions on Mathematical Software **22** (1996), no. 4, 469–483.
- [16] Julius S. Bendat and Allan G. Piersol, *Random data: Analysis and measurement procedures*, 4th ed ed., Wiley Series in Probability and Statistics, Wiley, Hoboken, N.J, 2010.
- [17] Miroslav Beneš and Barbara Zitová, *Performance evaluation of image segmentation algorithms on microscopic image data*, Journal of Microscopy **257** (2015), no. 1, 65–85.
- [18] Robert B. Bourne, Bert M. Chesworth, Aileen M. Davis, Nizar N. Mahomed, and Kory D. J. Charron, *Patient Satisfaction after Total Knee Arthroplasty: Who is Satisfied and Who is Not?*, Clinical Orthopaedics & Related Research **468** (2010), no. 1, 57–63.
- [19] G. Bradski, *The OpenCV library*, Dr. Dobb's Journal of Software Tools (2000).
- [20] Leo Breiman, *Bagging predictors*, Machine Learning **24** (1996), no. 2, 123–140.
- [21] Jordan S. Broberg, Joanna Chen, Andrew Jensen, Scott A. Banks, and Matthew G. Teeter, *Validation of a machine learning technique for segmentation and pose estimation in single plane fluoroscopy*, Journal of Orthopaedic Research (2023).
- [22] Lisa Gottesfeld Brown, *A survey of image registration techniques*, ACM Computing Surveys **24** (1992), no. 4, 325–376.
- [23] William Burton, Ignacio Rivero Crespo, Thor Andreassen, Moira Pryhoda, Andrew Jensen, Casey Myers, Kevin Shelburne, Scott Banks, and Paul Rullkoetter, *Fully automatic tracking of native glenohumeral kinematics from stereo-radiography*, Computers in Biology and Medicine **163** (2023), 107189.
- [24] William Burton, Andrew Jensen, Casey A. Myers, Landon Hamilton, Kevin B. Shelburne, Scott A. Banks, and Paul J. Rullkoetter, *Automatic tracking of healthy joint kinematics from stereo-radiography sequences.*, Computers in Biology and Medicine (2021).
- [25] Alexander Buslaev, Vladimir I. Iglovikov, Eugene Khvedchenya, Alex Parinov, Mikhail Druzhinin, and Alexandr A. Kalinin, *Albulmentations: Fast and Flexible Image Augmentations*, Information **11** (2020), no. 2, 125.
- [26] John Canny, *A Computational Approach to Edge Detection*, IEEE Transactions on Pattern Analysis and Machine Intelligence (1986).
- [27] F. Cenni, A. Leardini, M. Pieri, L. Berti, C. Belvedere, M. Romagnoli, and S. Giannini, *Functional performance of a total ankle replacement: Thorough assessment by combining gait and fluoroscopic analyses*, Clinical Biomechanics **28** (2013), no. 1, 79–87.

- [28] Francesco Cenni, Alberto Leardini, Claudio Belvedere, Francesca Buganè, Karin Cremonini, Maria T. Mischione, and Sandro Giannini, *Kinematics of the Three Components of a Total Ankle Replacement: In Vivo Fluoroscopic Analysis*, *Foot & Ankle International* **33** (2012), no. 4, 290–300.
- [29] Lyndon Chan, Mahdi Hosseini, Corwyn Rowsell, Konstantinos Plataniotis, and Savvas Damaskinos, *HistoSegNet: Semantic Segmentation of Histological Tissue Type in Whole Slide Images*, 2019 IEEE/CVF International Conference on Computer Vision (ICCV) (Seoul, Korea (South)), IEEE, October 2019, pp. 10661–10670.
- [30] T. M. Chan, *Optimal output-sensitive convex hull algorithms in two and three dimensions*, *Discrete & Computational Geometry* **16** (1996), no. 4, 361–368.
- [31] W.T. Cochran, J.W. Cooley, D.L. Favin, H.D. Helms, R.A. Kaenel, W.W. Lang, G.C. Maling, D.E. Nelson, C.M. Rader, and P.D. Welch, *What is the fast Fourier transform?*, *Proceedings of the IEEE* **55** (1967), no. 10, 1664–1674.
- [32] Corinna Cortes and Vladimir Vapnik, *Support-vector networks*, *Machine Learning* **20** (1995), no. 3, 273–297.
- [33] Carl D. Crane and Joseph Duffy, *Kinematic analysis of robot manipulators*, digitally printed version ed., Cambridge University Press, Cambridge, U.K., 2008.
- [34] R. Daems, Jan Victor, Patrick De Baets, S. Van Onsem, and Matthias Verstraete, *Validation of three-dimensional total knee replacement kinematics measurement using single-plane fluoroscopy*, *International Journal Sustainable Construction & Design* **7** (2016), no. 1, 14.
- [35] Richard J. de Asla, Lu Wan, Harry E. Rubash, and Guoan Li, *Six DOF in vivo kinematics of the ankle joint complex: Application of a combined dual-orthogonal fluoroscopic and magnetic resonance imaging technique*, *Journal of Orthopaedic Research* **24** (2006), no. 5, 1019–1027.
- [36] David W Dresigmeyer, *DIRECT SEARCH METHODS OVER LIPSCHITZ MANIFOLDS*, (2007).
- [37] Pedro F. Felzenszwalb and Daniel P. Huttenlocher, *Distance Transforms of Sampled Functions*, *Theory of Computing* **8** (2012), no. 1, 415–428.
- [38] Evelyn Fix and J.L. Hodges, Jr., *Discriminatory Analysis - Nonparametric Discrimination Consistency Properties*, February 1951.
- [39] P. D. L. Flood and Scott A. Banks, *Automated registration of 3-D knee implant models to fluoroscopic images using lipschitzian optimization*, *IEEE Transactions on Medical Imaging* **37** (2018), no. 1, 326–335.
- [40] William Tafel Freeman, *Steerable Filters and Local Analysis of Image Structure*, Ph.D. thesis, 1992.

- [41] Benjamin J. Fregly, W. Gregory Sawyer, Melinda K. Harman, and Scott A. Banks, *Computational wear prediction of a total knee replacement from in vivo kinematics*, Journal of Biomechanics **38** (2005), no. 2, 305–314.
- [42] Yoav Freund and Robert E Schapire, *A Decision-Theoretic Generalization of On-Line Learning and an Application to Boosting*, Journal of Computer and System Sciences **55** (1997), no. 1, 119–139.
- [43] Jerome H. Friedman, *Greedy function approximation: A gradient boosting machine.*, The Annals of Statistics **29** (2001), no. 5.
- [44] Bo Gao and Naiquan (Nigel) Zheng, *Investigation of soft tissue movement during level walking: Translations and rotations of skin markers*, Journal of Biomechanics **41** (2008), no. 15, 3189–3195.
- [45] E.H. Garling, B.L. Kaptein, B. Mertens, W. Barendregt, H.E.J. Veeger, R.G.H.H. Nelissen, and E.R. Valstar, *Soft-tissue artefact assessment during step-up using fluoroscopy and skin-mounted markers*, Journal of Biomechanics **40** (2007), S18–S24.
- [46] R.L. Graham, *An efficient algorith for determining the convex hull of a finite planar set*, Information Processing Letters **1** (1972), no. 4, 132–133.
- [47] Edward S. Grood and W. J. Suntay, *A Joint Coordinate System for the Clinical Description of Three-Dimensional Motions: Application to the Knee*, Journal of Biomechanical Engineering-transactions of The Asme (1983).
- [48] Marsha Jo Hannah, *Computer Matching of Areas in Stereo IMages*, Ph.D. thesis, Stanford University, 1977.
- [49] Ryuichiro Hataya, Jan Zdenek, Kazuki Yoshizoe, and Hideki Nakayama, *Faster AutoAugment: Learning Augmentation Strategies using Backpropagation*, arXiv:1911.06987 [cs] (2019).
- [50] Geoffrey Hinton, Nitish Srivastava, and Kevin Swersky, *Neural networks for machine learning lecture 6a overview of mini-batch gradient descent*, Cited on **14** (2012), no. 8, 2.
- [51] Sepp Hochreiter and Jürgen Schmidhuber, *Long Short-Term Memory*, Neural Computation **9** (1997), no. 8, 1735–1780.
- [52] Daniel P. Huttenlocher and William J. Rucklidge, *A multi-resolution technique for comparing images using the Hausdorff distance*, Proceedings of IEEE Conference on Computer Vision and Pattern Recognition (1993), 705–706.
- [53] D.P. Huttenlocher, G.A. Klanderman, and W.J. Rucklidge, *Comparing images using the Hausdorff distance*, IEEE Transactions on Pattern Analysis and Machine Intelligence **15** (Sept./1993), no. 9, 850–863.
- [54] International Organization for Standardization, *Accuracy (trueness and precision) of measurement methods and results*, July 2023.

- [55] Paul Jaccard, *The Distribution of the Flora in the Alpine Zone*, New Phytologist **11** (1912), no. 2, 37–50.
- [56] R A Jarvis, *On the Identification of the Convex Hull of a Finite Set of Points in the Plane*, (1973).
- [57] Jean-Yves Jenny, Scott Banks, and Florent Baldairon, *Registration of Knee Kinematics With a Navigation System: A Validation Study*, 2015.
- [58] Andrew J. Jensen, Paris D.L. Flood, Lindsey S. Palm-Vlasak, William S. Burton, Amélie Chevalier, Paul J. Rullkoetter, and Scott A. Banks, *Joint Track Machine Learning: An Autonomous Method of Measuring Total Knee Arthroplasty Kinematics From Single-Plane X-Ray Images*, The Journal of Arthroplasty **38** (2023), no. 10, 2068–2074.
- [59] Andrew James Jensen, Catia S. Silva, Kerry E. Costello, and Scott A. Banks, *Correcting Symmetric Implant Ambiguity in Measuring Total Knee Arthroplasty Kinematics from Single-Plane Fluoroscopy*, (In Review).
- [60] D. R. Jones, C. D. Pertunen, and B. E. Stuckman, *Lipschitzian optimization without the Lipschitz constant*, Journal of Optimization Theory and Applications **79** (1993), no. 1, 157–181.
- [61] Dan Jurafsky and James H. Martin, *Speech and language processing: An introduction to natural language processing, computational linguistics, and speech recognition*, 2nd ed ed., Prentice Hall Series in Artificial Intelligence, Pearson Prentice Hall, Upper Saddle River, N.J, 2009.
- [62] T. Kanade and M. Okutomi, *A stereo matching algorithm with an adaptive window: Theory and experiment*, IEEE Transactions on Pattern Analysis and Machine Intelligence **16** (Sept./1994), no. 9, 920–932.
- [63] Vasiliki Kefala, Adam J. Cyr, Michael D. Harris, Donald R. Hume, Bradley S. Davidson, Raymond H. Kim, and Kevin B. Shelburne, *Assessment of Knee Kinematics in Older Adults Using High-Speed Stereo Radiography*, Medicine & Science in Sports & Exercise **49** (2017), no. 11, 2260–2267.
- [64] Alex Kendall and Roberto Cipolla, *Geometric Loss Functions for Camera Pose Regression with Deep Learning*, 2017 IEEE Conference on Computer Vision and Pattern Recognition (CVPR) (Honolulu, HI), IEEE, July 2017, pp. 6555–6564.
- [65] David G. Kendall, *Shape Manifolds, Procrustean Metrics, and Complex Projective Spaces*, Bulletin of the London Mathematical Society **16** (1984), no. 2, 81–121.
- [66] Takehiro Kijima, Keisuke Matsuki, Nobuyasu Ochiai, Takeshi Yamaguchi, Yu Sasaki, Eiko Hashimoto, Yasuhito Sasaki, Hironori Yamazaki, Tomonori Kenmoku, Satoshi Yamaguchi, Yoshitada Masuda, Hideo Umekita, Scott A. Banks, and Kazuhisa Takahashi, *In vivo 3-dimensional analysis of scapular and glenohumeral kinematics: Comparison of symptomatic or asymptomatic shoulders with rotator cuff tears and healthy shoulders*, Journal of Shoulder and Elbow Surgery **24** (2015), no. 11, 1817–1826.

- [67] Diederik P. Kingma and Jimmy Ba, *Adam: A Method for Stochastic Optimization*, arXiv:1412.6980 [cs] (2017).
- [68] Jan J Koenderink, *The structure of images*, Biological Cybernetics **50** (1984), 363–370.
- [69] Jan J Koenderink and Andrea J Van Doorn, *Surface shape and curvature scales*, Image and Vision Computing **10** (1992), no. 8, 557–564.
- [70] Richard D. Komistek, Douglas A. Dennis, and Mohamed Mahfouz, *In Vivo Fluoroscopic Analysis of the Normal Human Knee*, Clinical Orthopaedics & Related Research **410** (2003), 69–81.
- [71] Alex Krizhevsky, Ilya Sutskever, and Geoffrey E. Hinton, *ImageNet Classification with Deep Convolutional Neural Networks*, Communications of the ACM **60** (2017), no. 6, 84–90.
- [72] Mei-Ying Kuo, Tsung-Yuan Tsai, Cheng-Chung Lin, Tung-Wu Lu, Horng-Chaung Hsu, and Wu-Chung Shen, *Influence of soft tissue artifacts on the calculated kinematics and kinetics of total knee replacements during sit-to-stand*, Gait & Posture **33** (2011), no. 3, 379–384.
- [73] Steven Kurtz, Kevin Ong, Edmund Lau, Fionna Mowat, and Michael Halpern, *Projections of Primary and Revision Hip and Knee Arthroplasty in the United States from 2005 to 2030*:, The Journal of Bone & Joint Surgery **89** (2007), no. 4, 780–785.
- [74] Mario A. Lafourte, Peter R. Cavanagh, H. J. Sommer, and A. Kalenak, *Three-dimensional kinematics of the human knee during walking*., Journal of Biomechanics (1992).
- [75] S. Lavallee and R. Szeliski, *Recovering the position and orientation of free-form objects from image contours using 3D distance maps*, IEEE Transactions on Pattern Analysis and Machine Intelligence **17** (1995), no. 4, 378–390.
- [76] Jong-Min Lee and Whoi-Yul Kim, *A New Shape Description Method Using Angular Radial Transform*, IEICE Transactions on Information and Systems **E95.D** (2012), no. 6, 1628–1635.
- [77] J. C. Léger, *Menger curvature and rectifiability*, April 1999.
- [78] Cheng-Chung Lin, Tung-Wu Lu, Hsuan-Lun Lu, Mei-Ying Kuo, and Horng-Chaung Hsu, *Effects of soft tissue artifacts on differentiating kinematic differences between natural and replaced knee joints during functional activity*, Gait & Posture **46** (2016), 154–160.
- [79] David G. Lowe, *Fitting parameterized three-dimensional models to images*, IEEE Transactions on Pattern Analysis and Machine Intelligence (1991).
- [80] Mohamed Mahfouz, Gregory Nicholson, Richard Komistek, David Hovis, and Matthew Kubo, *In Vivo Determination of the Dynamics of Normal, Rotator Cuff-Deficient, Total, and Reverse Replacement Shoulders*, The Journal of Bone & Joint Surgery **87** (2005), 107–113.

- [81] M.R. Mahfouz, W.A. Hoff, R.D. Komistek, and D.A. Dennis, *A robust method for registration of three-dimensional knee implant models to two-dimensional fluoroscopy images*, IEEE Transactions on Medical Imaging **22** (2003), no. 12, 1561–1574.
- [82] D. Marr, *Early processing of visual information*, Royal Society **275** (1976), no. 942, 483–519.
- [83] Keisuke Matsuki, Kei O. Matsuki, Shang Mu, Tomonori Kenmoku, Satoshi Yamaguchi, Nobuyasu Ochiai, Takahisa Sasho, Hiroyuki Sugaya, Tomoaki Toyone, Yuichi Wada, Kazuhisa Takahashi, and Scott A. Banks, *In vivo 3D analysis of clavicular kinematics during scapular plane abduction: Comparison of dominant and non-dominant shoulders*, Gait & Posture **39** (2014), no. 1, 625–627.
- [84] Keisuke Matsuki, Kei O. Matsuki, Shang Mu, Satoshi Yamaguchi, Nobuyasu Ochiai, Takahisa Sasho, Hiroyuki Sugaya, Tomoaki Toyone, Yuichi Wada, Kazuhisa Takahashi, and Scott A. Banks, *In vivo 3-dimensional analysis of scapular kinematics: Comparison of dominant and nondominant shoulders*, Journal of Shoulder and Elbow Surgery **20** (2011), no. 4, 659–665.
- [85] Keisuke Matsuki, Kei O. Matsuki, Satoshi Yamaguchi, Nobuyasu Ochiai, Takahisa Sasho, Hiroyuki Sugaya, Tomoaki Toyone, Yuichi Wada, Kazuhisa Takahashi, and Scott A. Banks, *Dynamic In Vivo Glenohumeral Kinematics During Scapular Plane Abduction in Healthy Shoulders*, Journal of Orthopaedic & Sports Physical Therapy **42** (2012), no. 2, 96–104.
- [86] Shang Mu, *JointTrack: An Open-Source, Easily Expandable Program for Skeletal Kinematic Measurement Using Model-Image Registration*, (2007), 27.
- [87] John Nickolls, Ian Buck, Michael Garland, and Kevin Skadron, *Scalable Parallel Programming with CUDA*, ACM Queue **6** (2008), no. 2, 40–53.
- [88] Mads Nielsen, Luc Florack, and Rachid Deriche, *Regularization, scale-space, and edge detection filters*, Computer Vision — ECCV '96 (Gerhard Goos, Juris Hartmanis, Jan van Leeuwen, Bernard Buxton, and Roberto Cipolla, eds.), vol. 1065, Springer Berlin Heidelberg, Berlin, Heidelberg, 1996, pp. 70–81.
- [89] Abigail E. Niesen, Anna L. Garverick, Stephen M. Howell, and Maury L. Hull, *Reorienting the tibial baseplate improves the registration accuracy of model-based radiostereometric analysis*, Journal of Biomechanics **113** (2020), 110078.
- [90] Stanislav Nikolov, Sam Blackwell, Alexei Zverovitch, Ruheena Mendes, Michelle Livne, Jeffrey De Fauw, Yojan Patel, Clemens Meyer, Harry Askham, Bernadino Romera-Paredes, Christopher Kelly, Alan Karthikesalingam, Carlton Chu, Dawn Carnell, Cheng Boon, Derek D'Souza, Syed Ali Moinuddin, Bethany Garie, Yasmin McQuinlan, Sarah Ireland, Kiarna Hampton, Krystle Fuller, Hugh Montgomery, Geraint Rees, Mustafa Suleyman, Trevor Back, Cíán Owen Hughes, Joseph R Ledsam, and Olaf Ronneberger, *Clinically Applicable Segmentation of Head and Neck Anatomy for Radiotherapy: Deep Learning Algorithm Development and Validation Study*, Journal of Medical Internet Research **23** (2021), no. 7, e26151.

- [91] Nobukazu Okamoto, Leigh Breslauer, Anthony K. Hedley, Hiroshi Mizuta, and Scott A. Banks, *In Vivo Knee Kinematics in Patients With Bilateral Total Knee Arthroplasty of 2 Designs*, The Journal of Arthroplasty **26** (2011), no. 6, 914–918.
- [92] Lindsey Palm-Vlasak, R Leitz, H Parvateneni, L Pulido, Mary Beth Horodyski, and Scott Banks, *Minimal Variation in Top Level and Decline Walking Speeds Between Pivoting TKA Subjects and Healthy Controls*, 2022.
- [93] Adam Paszke, Sam Gross, Francisco Massa, Adam Lerer, James Bradbury, Gregory Chanan, Trevor Killeen, Zeming Lin, Natalia Gimelshein, Luca Antiga, Alban Desmaison, Andreas Kopf, Edward Yang, Zachary DeVito, Martin Raison, Alykhan Tejani, Sasank Chilamkurthy, Benoit Steiner, Lu Fang, Junjie Bai, and Soumith Chintala, *PyTorch: An imperative style, high-performance deep learning library*, Advances in Neural Information Processing Systems 32, Curran Associates, Inc., 2019, pp. 8024–8035.
- [94] F. Pedregosa, G. Varoquaux, A. Gramfort, V. Michel, B. Thirion, O. Grisel, M. Blondel, P. Prettenhofer, R. Weiss, V. Dubourg, J. Vanderplas, A. Passos, D. Cournapeau, M. Brucher, M. Perrot, and E. Duchesnay, *Scikit-learn: Machine learning in Python*, Journal of Machine Learning Research **12** (2011), 2825–2830.
- [95] Eric Persoon and King-Sun Fu, *Shape Discrimination Using Fourier Descriptors*, **7** (1977), no. 3, 170–179.
- [96] Barbara Postolka, Renate List, Benedikt Thelen, Pascal Schütz, William R. Taylor, and Guoyan Zheng, *Evaluation of an intensity-based algorithm for 2D/3D registration of natural knee videofluoroscopy data*, Medical Engineering & Physics **77** (2020), 107–113.
- [97] Charles R. Qi, Li Yi, Hao Su, and Leonidas J. Guibas, *PointNet++: Deep Hierarchical Feature Learning on Point Sets in a Metric Space*, Advances in Neural Information Processing Systems **30** (2017).
- [98] Charles R. Qi, Hao Su, Kaichun Mo, and Leonidas J. Guibas, *PointNet: Deep Learning on Point Sets for 3D Classification and Segmentation*, arXiv:1612.00593 [cs] (2017).

- [99] Annika Reinke, Minu D. Tizabi, Michael Baumgartner, Matthias Eisenmann, Doreen Heckmann-Nötzel, A. Emre Kavur, Tim Rädsch, Carole H. Sudre, Laura Acion, Michela Antonelli, Tal Arbel, Spyridon Bakas, Arriel Benis, Matthew Blaschko, Florian Buettner, M. Jorge Cardoso, Veronika Cheplygina, Jianxu Chen, Evangelia Christodoulou, Beth A. Cimini, Gary S. Collins, Keyvan Farahani, Luciana Ferrer, Adrian Galdran, Bram van Ginneken, Ben Glocker, Patrick Godau, Robert Haase, Daniel A. Hashimoto, Michael M. Hoffman, Merel Huisman, Fabian Isensee, Pierre Jannin, Charles E. Kahn, Dagmar Kainmueller, Bernhard Kainz, Alexandros Karargyris, Alan Karthikesalingam, Hannes Kenngott, Jens Kleesiek, Florian Kofler, Thijs Kooi, Annette Kopp-Schneider, Michal Kozubek, Anna Kreshuk, Tahsin Kurc, Bennett A. Landman, Geert Litjens, Amin Madani, Klaus Maier-Hein, Anne L. Martel, Peter Mattson, Erik Meijering, Bjoern Menze, Karel G. M. Moons, Henning Müller, Brennan Nichyporuk, Felix Nickel, Jens Petersen, Susanne M. Rafelski, Nasir Rajpoot, Mauricio Reyes, Michael A. Riegler, Nicola Rieke, Julio Saez-Rodriguez, Clara I. Sánchez, Shravya Shetty, Maarten van Smeden, Ronald M. Summers, Abdel A. Taha, Aleksei Tiulpin, Sotirios A. Tsaftaris, Ben Van Calster, Gaël Varoquaux, Manuel Wiesenfarth, Ziv R. Yaniv, Paul F. Jäger, and Lena Maier-Hein, *Understanding metric-related pitfalls in image analysis validation*, September 2023.
- [100] Annika Reinke, Minu D. Tizabi, Carole H. Sudre, Matthias Eisenmann, Tim Rädsch, Michael Baumgartner, Laura Acion, Michela Antonelli, Tal Arbel, Spyridon Bakas, Peter Bankhead, Arriel Benis, Matthew Blaschko, Florian Büttner, M. Jorge Cardoso, Jianxu Chen, Veronika Cheplygina, Evangelia Christodoulou, Beth Cimini, Gary S. Collins, Sandy Engelhardt, Keyvan Farahani, Luciana Ferrer, Adrian Galdran, Bram van Ginneken, Ben Glocker, Patrick Godau, Robert Haase, Fred Hamprecht, Daniel A. Hashimoto, Doreen Heckmann-Nötzel, Peter Hirsch, Michael M. Hoffman, Merel Huisman, Fabian Isensee, Pierre Jannin, Charles E. Kahn, Dagmar Kainmueller, Bernhard Kainz, Alexandros Karargyris, Alan Karthikesalingam, A. Emre Kavur, Hannes Kenngott, Jens Kleesiek, Andreas Kleppe, Sven Kohler, Florian Kofler, Annette Kopp-Schneider, Thijs Kooi, Michal Kozubek, Anna Kreshuk, Tahsin Kurc, Bennett A. Landman, Geert Litjens, Amin Madani, Klaus Maier-Hein, Anne L. Martel, Peter Mattson, Erik Meijering, Bjoern Menze, David Moher, Karel G. M. Moons, Henning Müller, Brennan Nichyporuk, Felix Nickel, M. Alican Noyan, Jens Petersen, Gorkem Polat, Susanne M. Rafelski, Nasir Rajpoot, Mauricio Reyes, Nicola Rieke, Michael Riegler, Hassan Rivaz, Julio Saez-Rodriguez, Clara I. Sánchez, Julien Schroeter, Anindo Saha, M. Alper Selver, Lalith Sharan, Shravya Shetty, Maarten van Smeden, Bram Stieljes, Ronald M. Summers, Abdel A. Taha, Aleksei Tiulpin, Sotirios A. Tsaftaris, Ben Van Calster, Gaël Varoquaux, Manuel Wiesenfarth, Ziv R. Yaniv, Paul Jäger, and Lena Maier-Hein, *Common Limitations of Image Processing Metrics: A Picture Story*, August 2023.
- [101] Charles W. Richard and Hooshang Hemami, *Identification of Three-Dimensional Objects Using Fourier Descriptors of the Boundary Curve*, IEEE Transactions on Systems, Man, and Cybernetics **SMC-4** (1974), no. 4, 371–378.

- [102] Pedro Rodrigues, Michel Antunes, Carolina Raposo, Pedro Marques, Fernando Fonseca, and Joao P. Barreto, *Deep segmentation leverages geometric pose estimation in computer-aided total knee arthroplasty*, Healthcare Technology Letters **6** (2019), no. 6, 226–230.
- [103] Olaf Ronneberger, Philipp Fischer, and Thomas Brox, *U-Net: Convolutional Networks for Biomedical Image Segmentation*, Medical Image Computer and Computer-Assisted Intervention **9351** (2015), 234–241.
- [104] David E. Rumelhart, Geoffrey E. Hinton, and Ronald J. Williams, *Learning representations by back-propagating errors*, Nature **323** (1986), no. 6088, 533–536.
- [105] Olga Russakovsky, Jia Deng, Hao Su, Jonathan Krause, Sanjeev Satheesh, Sean Ma, Zhiheng Huang, Andrej Karpathy, Aditya Khosla, Michael Bernstein, Alexander C. Berg, and Li Fei-Fei, *ImageNet Large Scale Visual Recognition Challenge*, International Journal of Computer Vision **115** (2015), no. 3, 211–252.
- [106] Hannes Schulz and Sven Behnke, *Deep Learning: Layer-Wise Learning of Feature Hierarchies*, KI - Künstliche Intelligenz **26** (2012), no. 4, 357–363.
- [107] C. E. H. Scott, C. R. Howie, D. MacDonald, and L. C. Biant, *Predicting Dissatisfaction Following Total Knee Replacement: A Prospective Study of 1217 Patients*, The Journal of Bone and Joint Surgery. British volume **92-B** (2010), no. 9, 1253–1258.
- [108] G. Scott, M. A. Imam, A. Eifert, M. A. R. Freeman, V. Pinskerova, R. E. Field, J. Skinner, and S. A. Banks, *Can a total knee arthroplasty be both rotationally unconstrained and anteroposteriorly stabilised?: A pulsed fluoroscopic investigation*, Bone & Joint Research **5** (2016), no. 3, 80–86.
- [109] Göran Selvik, *Roentgen stereophotogrammetry: A method for the study of the kinematics of the skeletal system*, Acta Orthopaedica Scandinavica **60** (1989), no. sup232, 1–51.
- [110] Jean-Pierre Serre, *Lie algebras and Lie groups: 1964 lectures given at Harvard University*, 2nd. ed ed., Lecture Notes in Mathematics, no. 1500, Springer-Verlag, Berlin ; New York, 1992.
- [111] Leena Sharma and Francis Berenbaum, *Osteoarthritis: A companion to Rheumatology*, Mosby, Philadelphia, 2007.
- [112] Padhraic Smyth and David Wolpert, *Linearly Combining Density Estimators via Stacking*, **36** (1999), 59–83.
- [113] Rita Stagni, Silvia Fantozzi, Angelo Cappello, and Alberto Leardini, *Quantification of soft tissue artefact in motion analysis by combining 3D fluoroscopy and stereophotogrammetry: A study on two subjects*, Clinical Biomechanics **20** (2005), no. 3, 320–329.
- [114] Akira Sugi, Keisuke Matsuki, Ryunosuke Fukushi, Takeshi Shimoto, Toshiaki Hirose, Yuji Shibayama, Naoya Nishinaka, Kousuke Iba, Toshihiko Yamashita, and Scott A. Banks, *Comparing in vivo three-dimensional shoulder elevation kinematics between standing and supine postures*, JSES International **5** (2021), no. 6, 1001–1007.

- [115] Satoshi Suzuki and Keichi Abe, *Topological Structural Analysis of Digitized Binary Images by Border Following*, Computer Vision, Graphics, and Image Processing **30** (1985), 32–46.
- [116] Richard Szeliski, *Computer vision: Algorithms and applications*, second edition ed., Texts in Computer Science, Springer, Cham, 2022.
- [117] Abdel Aziz Taha and Allan Hanbury, *Metrics for evaluating 3D medical image segmentation: Analysis, selection, and tool*, BMC Medical Imaging **15** (2015), no. 1, 29.
- [118] Matthew G Teeter, Petar Seslija, Jaques S Milner, Hristo N Nikolov, Xunhua Yuan, Douglas D R Naudie, and David W Holdsworth, *Quantification of in vivo implant wear in total knee replacement from dynamic single plane radiography*, Physics in Medicine and Biology **58** (2013), no. 9, 2751–2767.
- [119] C. Tomasi and R. Manduchi, *Bilateral filtering for gray and color images*, Sixth International Conference on Computer Vision (IEEE Cat. No.98CH36271) (Bombay, India), Narosa Publishing House, 1998, pp. 839–846.
- [120] Ashish Vaswani, Noam Shazeer, Niki Parmar, Jakob Uszkoreit, Llion Jones, Aidan N. Gomez, Łukasz Kaiser, and Illia Polosukhin, *Attention Is All You Need*, December 2017.
- [121] Timothy P. Wallace and Owen R. Mitchell, *Analysis of three-dimensional movement using Fourier descriptors*, IEEE Transactions on Pattern Analysis and Machine Intelligence **PAMI-2** (1980), no. 6, 583–588.
- [122] Timothy P. Wallace and Paul A. Wintz, *An efficient three-dimensional aircraft recognition algorithm using normalized fourier descriptors*, Computer Graphics and Image Processing **13** (1980), no. 2, 99–126.
- [123] Jingdong Wang, Ke Sun, Tianheng Cheng, Borui Jiang, Chaorui Deng, Yang Zhao, Dong Liu, Yadong Mu, Mingkui Tan, Xinggang Wang, Wenyu Liu, and Bin Xiao, *Deep High-Resolution Representation Learning for Visual Recognition*, arXiv:1908.07919 [cs] (2020).
- [124] Toshifumi Watanabe, Masafumi Ishizuki, Takeshi Muneta, and Scott A. Banks, *Knee Kinematics in Anterior Cruciate Ligament-Substituting Arthroplasty With or Without the Posterior Cruciate Ligament*, The Journal of Arthroplasty **28** (2013), no. 4, 548–552.
- [125] Toshifumi Watanabe, Takeshi Muneta, Hideyuki Koga, Masafumi Horie, Tomomasa Nakamura, Koji Otake, Yusuke Nakagawa, Mai Kataura, and Ichiro Sekiya, *In-vivo kinematics of high-flex posterior-stabilized total knee prosthesis designed for Asian populations*, International Orthopaedics **40** (2016), no. 11, 2295–2302.
- [126] David H. Wolpert, *Stacked generalization*, Neural Networks **5** (1992), no. 2, 241–259.

- [127] Anqi Wu, E. Kelly Buchanan, Matthew R Whiteway, Michael Schartner, Guido Meijer, Jean-Paul Noel, Erica Rodriguez, Claire Everett, Amy Norovich, Evan Schaffer, Neeli Mishra, C. Daniel Salzman, Dora Angelaki, Andrés Bendesky, The International Brain Laboratory, John Cunningham, and Liam Paninski, *Deep Graph Pose: A semi-supervised deep graphical model for improved animal pose tracking*, Advances in Neural Information Processing Systems **33** (2020), 6040–6052.
- [128] Takaharu Yamazaki, Tetsu Watanabe, Yoshikazu Nakajima, Kazuomi Sugamoto, Kazuomi Sugamoto, Tetsuya Tomita, Hideki Yoshikawa, and Shinichi Tamura, *Improvement of depth position in 2-D/3-D registration of knee implants using single-plane fluoroscopy*, IEEE Transactions on Medical Imaging (2004).
- [129] Jong Chul Ye, *Geometry of Deep Learning: A Signal Processing Perspective*, Mathematics in Industry, vol. 37, Springer Nature Singapore, Singapore, 2022.
- [130] Varduhı Yeghiazaryan and Irina Voiculescu, *Family of boundary overlap metrics for the evaluation of medical image segmentation*, Journal of Medical Imaging **5** (2018), no. 01, 1.
- [131] Jacob Yerushalmy, *Statistical Problems in Assessing Methods of Medical Diagnosis, with Special Reference to X-Ray Techniques*, Public Health Reports (1896-1970) **62** (1947), no. 40, 1432.
- [132] B.-M. You, P. Siy, W. Anderst, and S. Tashman, *In vivo measurement of 3-D skeletal kinematics from sequences of biplane radiographs: Application to knee kinematics*, IEEE Transactions on Medical Imaging **20** (2001), no. 6, 514–525.
- [133] Yuhui Yuan, Jingyi Xie, Xilin Chen, and Jingdong Wang, *SegFix: Model-Agnostic Boundary Refinement for Segmentation*, Computer Vision – ECCV 2020 (Andrea Vedaldi, Horst Bischof, Thomas Brox, and Jan-Michael Frahm, eds.), vol. 12357, Springer International Publishing, Cham, 2020, pp. 489–506.
- [134] Dengsheng Zhang and Guojun Lu, *Review of shape representation and description techniques*, Pattern Recognition **37** (2004), no. 1, 1–19.
- [135] Zongwei Zhou, Md Mahfuzur Rahman Siddiquee, Nima Tajbakhsh, and Jianming Liang, *UNet++: A Nested U-Net Architecture for Medical Image Segmentation*, Deep Learning in Medical Image Analysis and Multimodal Learning for Clinical Decision Support (Danail Stoyanov, Zeike Taylor, Gustavo Carneiro, Tanveer Syeda-Mahmood, Anne Martel, Lena Maier-Hein, João Manuel R.S. Tavares, Andrew Bradley, João Paulo Papa, Vasileios Belagiannis, Jacinto C. Nascimento, Zhi Lu, Sailesh Conjeti, Mehdi Moradi, Hayit Greenspan, and Anant Madabhushi, eds.), vol. 11045, Springer International Publishing, Cham, 2018, pp. 3–11.
- [136] Wolfgang Ziller, *Lie Groups. Representation Theory and Symmetric Spaces*, University of Pennsylvania (2010).
- [137] S. Zuffi, A. Leardini, F. Catani, S. Fantozzi, and A. Cappello, *A model-based method for the reconstruction of total knee replacement kinematics*, IEEE Transactions on Medical Imaging **18** (Oct./1999), no. 10, 981–991.

BIOGRAPHICAL SKETCH

Andrew Jensen is a Florida native from Sarasota, Florida. He attended the University of Florida for his undergraduate degree in Mechanical Engineering, for which he received high honors. He took a brief hiatus from school to work at an orthopaedic solutions company, Exactech. The COVID-19 pandemic cut his time at Exactech short, so he joined the Gary J Miller Orthopaedic Biomechanics Laboratory as a part-time researcher during the summer leading up to his first official semester of graduate school.

Andrew enjoys reading (mostly philosophy and science fiction), working out, and hanging out with his dog.